Self-demixing of mRNA copies buffers mRNA:mRNA and mRNA:regulator stoichiometries

Andrés Cardona, Szilvia Ecsedi, Mokrane Khier, Zhou Yi, Alia Bahri, Amira Ouertani, Florian Valero, Margaux Labrosse, Sami Rouquet, Stéphane Robert, et al.

Title: Robust sorting and buffering within condensates control transcriptome stoichiostasis

Authors: Andrés H. Cardona[1]*, Szilvia Ecsedi[1]*, Mokrane Khier[1], Zhou Yi[1], Alia Bahri[1], Amira Ouertani[1], Florian Valero[1], Margaux Labrosse[1], Sami Rouquet[1], Stéphane Robert[2], Agnes Loubat[1], Danielle Adekunle[3], Arnaud Hubstenberger[1#]

Affiliations:
[1]Université Côte D'Azur, CNRS, Inserm, iBV, Nice, France.
[2]Université Aix Marseille, Inserm, INRAE, C2VN, Marseille, France.
[3]Université Côte D'Azur, CNRS, IRCAN, Nice, France.
[#]Corresponding author. Email: Arnaud.HUBSTENBERGER@univ-cotedazur.fr
*These authors contributed equally to this work

Graphical abstract

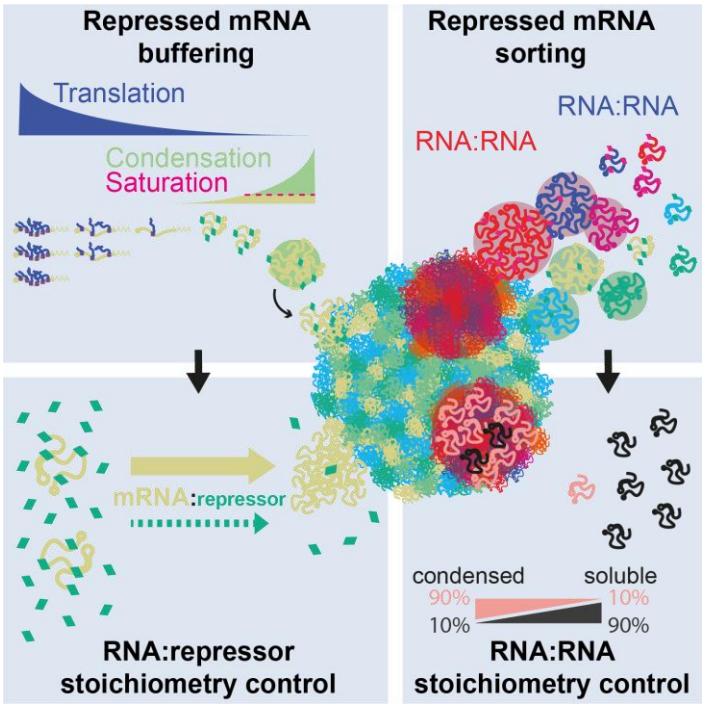

Highlights

mRNA phase separations buffer variation in translational activity

mRNA sorting and buffering into nanoclusters controls transcriptome stoichiometries

Repressed mRNA condensation prevents cytosolic depletion of translation repressors

Transcriptome-wide mRNA compaction is a default but selective state upon quiescence

Abstract

Cellular homeostasis requires the robust control of biomolecule concentrations, but how do millions of mRNAs coordinate their stoichiometries in the face of dynamic translational changes? Here, we identified a two-tiered mechanism controlling mRNA:mRNA and mRNA:protein stoichiometries where mRNAs super-assemble into condensates with buffering capacity and sorting selectivity through phase transition mechanisms. Using C. *elegans* oogenesis arrest as a model, we investigated the transcriptome cytosolic reorganization through the sequencing of RNA super-assemblies coupled with single mRNA imaging. Tightly repressed mRNAs self-assembled into same-sequence nanoclusters that further co-assembled into multiphase condensates. mRNA self-sorting was concentration-dependent, providing a self-buffering mechanism that is selective to sequence identity and controls mRNA:mRNA stoichiometries. The cooperative sharing of limiting translation repressors between clustered mRNAs prevented the disruption of mRNA:repressor stoichiometry in the cytosol. The robust control of mRNA:mRNA and mRNA:protein stoichiometries, which we term transcriptome stoichiostasis, emerges from mRNA self-buffering and cooperative super-assembly into multiphase multiscale condensates.

Keywords: phase separations, phase transitions, RNA condensates, homeostasis, RNP stoichiometry, buffering, sorting, translation, multiscale condensates, nanoclusters.

INTRODUCTION

Cells undergo dramatic activity changes yet must maintain stable internal conditions. Maintaining homeostasis in the face of massive fluctuations in biomolecule concentrations is a challenging task. For example, the stoichiometric information of mRNAs must be robustly controlled transcriptome-wide.[1,2] Transcription and mRNA decay are two strategies for mRNA copy number control. Translation regulation also uncouples protein production from mRNA expression[3] and provides spatiotemporal control of gene expression.[4] How cells buffer variations in translation to maintain a robust control of transcriptome stoichiometries remains to be addressed.

To control mRNA translation, regulatory proteins assemble with mRNAs into ribonucleoproteins (RNPs).[5] In a first layer of coordination, regulators are distributed across mRNA collectives that share the same binding elements, termed RNA regulons.[1,3] To further ensure robust translation control, mRNAs are co-repressed with redundant repressors or cofactors.[6–8] We and others introduced the conceptual framework of phase transitions where coregulated RNAs can further co-assemble into liquid droplets, semi-liquid hydrogels, or solidify into glass or crystal-like forms.[9–11] Co-repressed mRNAs condense transcriptome-wide[3,12–14], and despite the characterization of reconstituted repressive condensates[15–17], whether condensation is a cause or a consequence of translation repression *in vivo* is unclear.[4] While repression can occur in the absence of condensation, it has been observed that widespread mRNA repression during cellular quiescence and stress triggers condensation[18–20]. We therefore hypothesized that condensates may buffer the accumulation of repressed mRNAs.[1]

Phase transition theory predictions remain rarely quantitatively tested *in vivo*.[21–23] An open question is whether endogenous condensates have the storage capacity and selectivity to buffer

biomolecules within the crowded and complex cellular environment.[1] In solution, biomolecules remain soluble up to a saturation concentration, above which the fraction in excess co-assembles to concentrate into condensates, limiting the accumulation of biomolecules in the dispersed phase.[11] Whether various condensates buffer protein concentrations or reduce protein noise has been debated.[24,25] The ability of condensates to selectively buffer stoichiometric variations between a vast diversity of mRNAs is unknown. Translation repression has been proposed to be sufficient to target mRNAs to condensates through promiscuous interactions.[12,13,26] While this may explain how condensates are hijacked to non-specific aggregates in degenerative diseases,[27,28] this is incompatible with buffering selectivity. In fact, these low selectivity models contradict (i) the diversity of repressed mRNA condensates that coexist within cells,[1] (ii) the coexistence of multiple protein phases within condensates,[10,29–31] (iii) the absence of mixing between repressed mRNA species that form homotypic nanoclusters[32–35]. In addition to selectively buffering biomolecules, condensates have been postulated to have storage capacity. Although prevailing models suggest that stress granules and P-bodies have limited storage capacity, large variations in translation nevertheless indicate the existence of subcellular reservoirs. Nanoclusters may represent the invisible stores. Condensate buffering could provide a protective mechanism to maintain homeostasis. However, to date, studies characterizing the adaptive properties of condensates are few.[36–38]

Using C. *elegans* oogenesis as an in vivo model, we address how phase separations control mRNA stoichiometries. Archetypes of long-lived cells, oocytes maintain fitness through quiescence, and experience dramatic changes in cellular activity upon stimulation. In the absence of transcription within oocytes, maternal mRNA condensation may tend towards equilibrium as metabolic activity drops. Maternal mRNAs can accumulate in viscoelastic C. *elegans* P-bodies,[10,39] solid Xenopus Balbiani-bodies,[40] or hydrogel-like mammalian MARDOs.[41] We analyzed the supramolecular organization of oocyte transcriptomes and found that oogenesis arrest requires the large-scale, long-term, selective storage of the maternal transcriptome through high compaction into multiscale multiphase condensates that allow the dynamic and sequential retrieval of information as development resumes. We demonstrate that (i) repressed mRNAs saturate in an identity dependent manner providing a selective concentration buffering mechanism, (ii) this saturation-dependent clustering impacts mRNA:mRNA and mRNA:protein stoichiometries transcriptome-wide, (iii) condensation is exponential to the degree of translation repression. Our study provides a quantitative model of how RNA self-organization selectively and robustly buffers mRNA cytosolic stoichiometric variations in a sequence- and translation activity-dependent manner.

RESULTS

Transcriptome-wide mRNA condensation is a default but selective state upon quiescence

To explore the remodeling of the transcriptome during cellular adaptation to quiescence, we took advantage of C. *elegans* oogenesis rates, which can be reversibly controlled through the depletion of sperm (quiescent oogenesis) or the addition of sperm (active oogenesis). Oogenesis rates differ dramatically between active and quiescent oogenesis with one oocyte produced every ~20 minutes to one every ~10 hours.[42] In both oogenesis states oocytes remarkably maintain their

fitness, providing a unique model of cellular adaptation. Quiescence triggers the accumulation of translationally repressed mRNPs into P-body condensates that can grow up to 10 µm in size (Figures 1A, B).[10,20,39,43–45]

To address whether P-bodies are quiescence-adaptive reservoirs with storage capacity and selectivity for repressed mRNAs, we first focused on candidate mRNAs that were previously shown to be repressed (*spn-4*, *glp-1*) or translated (*puf-5*, *tbb-2*, *pccb-1*) in oocytes.[46] The repression cofactor protein GFP:CAR-1 was used to label P-bodies in arrested oocytes,[10,39,45] and single-molecule fluorescent *in situ* hybridization (smFISH) was used to quantify mRNA clustering.[47,48] To ensure that RNA condensation did not lead to over- or under-detection of mRNAs we controlled for the linear quantitative scaling between single transcripts and clustered mRNAs after calibrating single mRNA fluorescence intensity (see Figure S1, methods and associated quantitative controls). The two translationally repressed mRNAs, *spn-4* and *glp-1*, were found to be more than 100-fold concentrated in P-bodies compared to the surrounding cytosol (Figures 1B, 1B', S2A-E). In contrast, the two translated *pccb-1* and *tbb-2* mRNAs were concentrated less than 10-fold (Figures 1B, 1B', S2A, S2E). This differential partitioning of mRNAs in P-bodies corresponds to a dynamic range of 90% to 20% of sequestered mRNAs (Figures 1B, 1B', S2B, S2E), demonstrating that condensation depletes the cytosol of large but selective mRNA fractions. Although there was a poor correlation between mRNA abundance and mRNA condensation, both translationally repressed mRNAs strongly partitioned to P-bodies while both translated mRNAs partitioned less efficiently (Figure 1B'', S2A-B). For some mRNA species, tens of thousands of copies condensed per cell indicating that condensates could be reservoirs with large storage capacity (Figure 1B''', S2C-D).

To expand our quantification of condensation transcriptome-wide, we adapted our Fluorescence Activated Particle Sorting and RNA-sequencing (FAPSeq) method to oocytes (Figure 1C).[3] Oocyte P-bodies were labelled with GFP:CAR-1, formaldehyde fixed, and FAPS sorted by their size and fluorescence using whole animal extracts (Figure 1D), then subjected to RNA-sequencing. Using FAPSeq we computed mRNA enrichment in P-bodies versus whole oocytes (Figures S2F-S2I, Data S1). This strongly correlated (r^2>0.95) with the mRNA enrichments computed by smFISH imaging for candidate mRNAs, cross-validating the two approaches (Figure S2J). Calibrating RNA-Seq relative levels (Data S2) with imaging absolute numbers (Figures S2K, S2L) allowed us to extrapolate mRNA copy numbers within and outside P-bodies transcriptome-wide (Figure 1E, Data S3). For mRNAs of similar abundance, the degree of enrichment within P-bodies ranged across orders of magnitude, suggesting sorting selectivity (Figure 1E). The dynamic range of condensation was between 10 to 90%. The median across all mRNA species was 65% (Figures 1F, S2M-P). Together, this demonstrated that despite selectivity, large-scale condensation is the rule rather than the exception upon quiescence.

Translationally repressed mRNAs condense into oocyte P-body reservoirs

To define the features that distinguish condensed RNAs, we computed the degree of P-body enrichment of different RNA types compared to the whole oocyte transcriptome. mRNAs were strongly enriched compared to all ncRNAs we investigated (Figure 2A). Moreover, tRNAs and rRNAs, and components of the translation machineries, were among the most severely depleted

(Figures 2A, 2B), suggesting that P-body mRNAs are not translationally active. Ranking candidate mRNAs according to the abundance of their protein output in oocytes[46] confirmed that mRNA enrichment within P-bodies is inversely correlated with protein production (Figure 2C, Table S1). Accordingly, the mRNA targets of translation repressors PUF-5[49] and OMA-1/LIN-41[50] were also strongly enriched in oocyte P-bodies at the developmental stage at which these repressors function, whereas the targets of repressors that function at earlier stages were not (Figure 2D). Translationally repressed P-body mRNAs tended to encode regulatory functions, whereas mRNAs excluded from P-bodies tended to encode for proteins with constitutive, housekeeping, metabolic and structural functions (Figure 2E). By comparing mRNAs enriched in P-bodies to whole oocyte mRNAs we found that P-body mRNAs have longer 3'UTRs, while there was no significant length difference for CDSs or 5'UTRs (Figure S3A). This is in contrast to stress granule and P-granule mRNAs that have been shown to possess longer 3'UTRs, CDSs, and 5'UTRs (Figure S3A).[12,13] The absence of compositional bias (Figures S3B) and the restriction of length bias to 3'UTRs (Figures S3A) suggests more selective mechanisms for condensate sorting. The targets of some RBPs identified by CLIP are strongly enriched in P-bodies (Figure 2D), yet individually these RBPs do not explain the transcriptome-wide complexity of super-assemblies as these represent a small subset of the P-body transcriptome (Figure 1E).

Homotypic mRNA nanoclusters coarsen into multiscale, multiphase condensates

Our identification of the coexistence of thousands of mRNAs in condensates raised the question of the mechanism of their super-assembly. Classic phase separation theory predicts that as a system tends toward equilibrium a single large droplet will integrate smaller ones over time in a growth mechanism, termed coarsening, that minimizes the energy of surface tension at the interfaces (Figure 3A). To test whether coarsening applies to the viscoelastic P-bodies that were previously shown to relax under surface tension[10], we took advantage of the spatiotemporal organization of oocytes within gonads to record the sizes of GFP:CAR-1 condensates at various time-points (Figures 3B, 3C). In the oldest quiescent oocytes, 1-2 supersize outliers per cell outgrew the smaller condensates in a time-dependent manner to occupy most of the condensate cumulative volume (Figures 3C, 3C'). Although this coarsening fits the classic phase separation theory, the condensate growth was extremely slow and occurred over a week-long period. In combination with their viscoelastic properties[10], the slow growth of P-bodies is in contrast to the liquid P-granules that grow on a timescale of seconds.[9]

To determine when condensates arose, we considered two possibilities: (1) mRNA clusters were nucleated and grew during quiescence (2) smaller mRNA clusters existed prior to quiescence but were below detection limits. To distinguish between these two possibilities, we took advantage of the tunable rates of oogenesis.[42] In the absence of fertilization, oocytes remain arrested on a week-long time scale. In active oogenesis, oogenesis arrest occurred within hours, and macro-condensates were not detected (Figure 3C), as expected given their week-long growth upon quiescence. However, s*pn-4* smFISH uncovered nanoclusters that cumulatively accumulated half of the total repressed *spn-4* mRNAs, demonstrating that clustering has been previously largely underestimated due to resolution limitations (Figures 3D, 3D', S4). Although coarsening kinetics were limiting in active cells, nucleation was not, as small mRNA clusters were detected prior to quiescence. Upon quiescence, mRNAs slowly redistributed to supersize outliers. In addition, the

slope of the power-law distribution distinguished nanoclusters from macro-condensates, suggesting divergent mechanisms of assembly (Figure 3D, 3D'). Taken together, the ability to segregate large mRNA fractions is not restricted to macro-condensates and includes nanoclusters of active cells.

The cluster size distribution of *spn-4* mRNAs demonstrated the coexistence of four mRNA populations: single molecules, nanoclusters, macro-condensates, and supersize outliers (Figures 3D, 3D', S4D). To test whether compositional differences could explain the size distribution discontinuity between nanoclusters and macro-condensates we simultaneously labeled two translationally repressed mRNAs, *spn-4* and *glp-1* (Figure 3E). Imaging uncovered that smaller clusters were homotypic, they contained only *glp-1* or *spn-4* (Figure 3E-E'). Although homotypic clusters of *spn-4*, *glp-1,* or another repressed mRNA, *mbk-2,* co-assembled into heterotypic macro-condensates (Figure 3E-E', S5), their patterns were anticorrelated within macro-condensates (Figures 3E''-E''', S5I-K), supporting demixing between mRNAs of different identities. In addition to the RNA-protein interactions of single RNP assemblies, new interaction scales emerged from RNP clustering: homotypic RNA-RNA interactions within nanoclusters, and heterotypic interactions between nanoclusters that co-assembled but poorly mixed. Moreover, while RNA-RNA demixing separated mRNA species (Figure 3F), protein-protein demixing defined subcompartments on a larger scale within condensates (Figures 3G).[10,31] We conclude the multiscale multiphase organization of the transcriptome (Figure 3H).

Buffering of repressed mRNA concentration variations by condensates promotes robust cytosolic mRNA:protein stoichiometries

The observation that condensates grow when repressed mRNAs accumulate upon quiescence (Figure 3) suggested that condensates could provide a buffering mechanism that limits the accumulation of repressed mRNAs in the cytosol. To test whether condensates could buffer mRNAs:repressors stoichiometric variations, we analyzed concentration variations during oogenesis for the repressed mRNA, *spn-4*, and translation repressor CAR-1. Imaging revealed *spn-4* and CAR-1 cytosolic concentrations remained constant across oogenesis, while their relative stoichiometries within condensates dramatically changed (Figures 4A, 4B, S6). Additionally, despite a 4-fold variation between animals in total cellular *spn-4* copy numbers for similarly staged diakinesis oocytes, cytosolic copy numbers remained almost identical (Figure 4C). Sequestration to condensates buffered the *spn-4* mRNA variations. To further test the impact of this sequestration on cytosolic concentrations, we depleted the critical P-body component PUF-5 that is essential for RNA condensation into P-bodies (Figures 4D, S6B).[10] *puf-5(RNAi)* induced dissolution led to a more than 8-fold increase in *spn-4* mRNA cytosolic concentrations, consistent with our finding that 90% of *spn-4* mRNAs localized to condensates (Figures 4E, 4F, and Figures S6C-S6D). In contrast, less than 25% of CAR-1 repressors segregated to condensates (Figures 4E, S6A-S6A"), and no significant increase upon dissolution was detected (Figures 4F, S6B, S6B'). We conclude that condensates are more potent at sequestrating repressed mRNAs than repressors, and thus buffer repressed mRNAs without depleting the cytosol of repressors.

The buffering capacity of condensates may provide an adaptation mechanism to quiescence during which repressed mRNAs accumulate and repressors may become limiting. Moreover,

condensation associated repression systems may become essential upon quiescence. To test this, we first confirmed that condensation associated repression systems are not limiting in active oogenesis, where PUF-5 represses redundantly with PUF-6/7.[6,7] As previously reported, PUF-5 depletion had a very limited impact in active oogenesis: mRNA repression was maintained (Figure 4G), and oocytes remained fit enough to produce viable embryos (Figure 4H). However, depletion in quiescent oocytes not only induced a dissolution of mRNAs (Figure 4D, F),[10] but also a dramatic increase in translation for some mRNAs (Figure 4G), and a drop in fitness of quiescent oocytes, as they no longer produced viable embryos (Figure 4H). Of note, mRNAs were differentially sensitive to the disruption of the condensation-repression system that was limiting upon quiescence: *fog-1* translation dramatically increased whereas *spn-4* did not (Figure 4G). Altogether, we provide evidence that a condensation associated repression system is not only critical for buffering the accumulation of repressed mRNAs and maintaining robust translation control as repressors become limiting, but is also essential for oocytes to adapt to repressed mRNA accumulations upon quiescence.

Repressed mRNAs saturate autonomously but partition cooperatively

Many mRNAs co-exist within oocyte condensates (Figure 1E), raising the question of whether each mRNA species' condensation is individually regulated. In a concentration-dependent phase transition, biomolecules remain soluble at low concentrations, but condense past saturation (Figure 5A).[11] In a simple homotypic phase transition model, as molecules in excess of the saturation concentration self-assemble into condensates, the dispersed phase concentration plateaus, providing a buffering mechanism (Figure 5B).[24] In a heterotypic model, when molecules co-assemble with binding partners the saturation concentration may become partner-dependent, and consequently can hinder buffering (Figure 5B).[25] Hence, each repressed mRNA species could either autonomously self-assemble according to its own concentration, or any repressed mRNA could cooperatively co-assemble as a function of total repressed mRNA concentrations, independent of sequence identity. To distinguish between these two models, we first tested mRNA clustering response to variations in *spn-4* mRNA concentrations. We analyzed arrested oocytes with various levels of *spn-4* depending on *spn-4 (RNAi)* efficiency, and computed *spn-4* clustering by smFISH as a function of *spn-4* total cellular concentration (Figure 5C). Strikingly, *spn-4* could accumulate as a soluble, single transcript in the dispersed phase until it plateaued at a saturation concentration and nanoclusters appeared as a threshold effect (Figures 5C, 5D). The dose-response fit a homotypic rather than a heterotypic phase separation model (Figures 5D and 5B comparison). Furthermore, macro-condensate imaging showed *spn-4* preferentially clustered with itself (Figures 3E-3F, S5). These two results confirmed that *spn-4* mRNA saturates independently of other mRNAs in a model where homotypic interactions dominate over heterotypic.

While scaffolding components are essential for condensate assemblies, clients are recruited to pre-existing condensates[51]. At very low *spn-4* concentrations, *spn-4* homotypic nanoclusters dissolved, but heterotypic macro-condensates did not (Figure 5C, 5D). We also observed a biphasic partition coefficient of *spn-4* across concentrations confirming the existence of two regimes: (1) recruitment to pre-existing macro-condensates through heterotypic interactions as a client at lower concentrations, and (2) self-assembly into nanoclusters at higher concentrations

(Figure 5E). At low concentrations *spn-4* partitioned strongly to condensates (>100-fold), but partitioning quickly dropped as *spn-4* concentrations increased, suggesting that the recruitment as a client relied on specific but limited binding sites that became quickly occupied. Most strikingly, towards higher concentrations, self-assemblies provided a *spn-4* self-buffering mechanism: above saturation concentration repressed *spn-4* mRNAs in excess self-segregated instead of flooding the cytosol where *spn-4* concentrations remained clamped at a fixed concentration.

The coexistence of diverse homotypic mRNA clusters within macro-condensates (Figure 3E-F, Figure S5I-K) suggested that this self-buffering mechanism is not restricted to *spn-4*, but instead extends transcriptome-wide. We analyzed the distributions of mRNA condensation as a function of mRNA concentrations using FAPSeq data (Figure 5F). Two distinct classes of distribution profiles of mRNA condensation existed depending on mRNA concentrations. Above a concentration threshold, the distributions of mRNAs shifted toward higher condensation, and the dispersion of the distribution narrowed down (Figure 5F). This sharp shift that was reminiscent of a thresholding effect where condensation occurs past a saturation concentration. Despite the general trend of increased condensation above a copy number threshold, a number of poorly expressed mRNAs were strongly enriched, likely through a client mechanism as described for *spn-4.* Conversely some highly expressed mRNAs were poorly enriched in P-bodies, and may represent a population of translated mRNAs that remain soluble at high concentrations. These two independent approaches, (i) the single-molecule imaging of *spn-4* candidate mRNA, and (2) the purification sequencing of condensed mRNAs, independently confirmed that mRNA clustering into condensates buffered the accumulation of approximately half of oocyte mRNAs as their expression exceeded a concentration threshold that was mRNA identity-dependent.

Condensates buffer the tightest states of mRNA translation repression

Because mRNA translation repression occurred in the absence of macro-condensates in active oogenesis, while condensates buffered the accumulation of repressed mRNAs upon quiescence (Figure 5), we wanted to functionally characterize and quantitively model the relationship between repression and condensation. Our results, thus far, suggest that ribosome-free repressed mRNAs condense, while translated mRNAs remain soluble at high concentrations (Figure 1B'', 2A-C, 5F). In a simple linear model, as the translation output doubles, the number of ribosome-bound mRNAs, and thus soluble mRNAs, also doubles (Figure 6A). In a second model, translation output depends on ribosome density. Only when translation output tends toward zero, does the probability to be ribosome free (condensed) exponentially increases (Figure 6B). To distinguish between these two models, we focused on *spn-4* translation activation during oocyte maturation. Translation rates were estimated from recording changes in SPN-4:GFP levels across oogenesis time-points (Figures 6C-6D'), while mRNA clustering was quantified from *spn-4* smFISH imaging (Figures 6E-6F''). In both active and quiescent oogenesis, SPN-4:GFP protein only accumulated during late oogenesis (Figures 6C-6D'), recapitulating the pattern of *spn-4* translation activation.[50] During the slow translation activation of quiescent oogenesis, macro-condensates dissolved into smaller clusters (Figures 6E-6E''), and upon the robust translation activation of active oogenesis, nanoclusters dissolved into single molecules (Figures 6F-6F'').

Contrary to repressed mRNAs, translated mRNAs remained soluble at very high concentrations (Figures 6F''). Although mRNA clusters dissolved upon translation activation, there was no linear relationship between the fraction of soluble molecules and the translation output, supporting the non-linear model (Figure 6G). Only tightly repressed mRNAs were clustered. As translation reached less than 5% of the maximum efficiency, cluster sizes had already dropped by four orders of magnitude (Figures 6C', 6E'). At 15% of maximum translation efficiency, more than 50% of *spn-4* were solubilized (Figure 6G). Conversely, towards high translation output, a less than 2-fold increase in the number of soluble molecules was enough to provide a 10-fold increase in translation (Figure 6G). Translation output was dependent on translation efficiency per soluble mRNA rather than the number of soluble mRNAs. While the soluble mRNA fraction was translationally regulated across wide ranges of efficiency, there was an exponential relationship between mRNA condensation and the degree of repression (Figure 6G-H). Even subtle increases in translation frequency were associated with massive condensate dissolutions (Figure 6G-H), in accordance with the days-long repression requirement for condensate growth. The kinetics of mRNA translation dominated over the kinetics of condensation. We conclude that translation control mainly occurs in the dispersed phase of the cytoplasm where the translation efficiency of single transcripts is adapted to cellular activity. Condensates buffer the exponential accumulation of repressed mRNAs as translation drops, and conversely quickly dissolve upon translation activation.

The ability of repressed mRNAs to condense autonomously according to their identity through self-assembly into homotypic clusters indicated that mRNAs should similarly dissolve independent of each other according to their respective translation activation profile. To test this, we compared *spn-4* mRNA that is activated upon oocyte maturation to *glp-1*, an mRNA that remains translationally repressed until later embryogenesis (Figure 6I). While, *spn-4* was released from macro-condensates upon translation activation, repressed *glp-1* remained sequestered (Figures 6J-6K). We conclude that multiphase condensates are decentralized systems where distinct mRNA identities coexist within the same macro-condensate while being regulated autonomously.

DISCUSSION

In the context of gene expression control, whether condensates reduce protein expression noise, or provide a concentration-buffering mechanism has been debated.[24,25] By focusing on mRNA dynamics rather than those of proteins in our dissection of multi-scale multiphase assemblies, we uncovered how condensates selectively control transcriptome stoichiometries (Figure 7A). mRNAs first assemble with soluble regulators into single mRNPs whose translation is regulated in the dispersed phase. As translation drops, tightly repressed mRNPs do not exceed a fixed saturation concentration, without self-assembling in a self-buffering mechanism that selectively depends on mRNA identity. Diverse nanoclusters further coalesce but poorly mix within macro-condensate subcompartments, that are themselves defined through protein-protein phase separations.[10,31] Lowly abundant mRNAs below saturation are alternatively recruited as clients to preexisting macro-condensates, diversifying partition mechanisms. Thousands of mRNAs can therefore co-exist within condensates and their concentrations can be independently coordinated to cellular activity (Figure 7A). Their autonomous self-assembly prevents one accumulating

repressed mRNA from disrupting others. The better partitioning of mRNAs as compared to regulatory proteins further ensures that mRNA sequestration does not deplete the cytosol of regulators. mRNAs cooperatively share limiting regulators, preventing the disruption of RNA:protein stoichiometry in the dispersed phase. Altogether, condensates allow for a selective and robust buffering of biomolecule stoichiometry variations.

Beyond their ability to protect cells from stoichiometry variations, the unique properties of oocyte P-bodies define their reservoir functionality for the long-term and large-scale storage of maternal mRNA information. We have previously shown that the semi-liquid properties of the viscoelastic P-body droplets in arrested oocytes, mechanically "freeze" repressed RNPs that must be preserved for long-term storage until oogenesis resume.[10] Such "solidification" of maternal stores is conserved through evolution.[40,41] Here, we demonstrate that with a median storage capacity of 65% of mRNA copies, oocyte P-bodies provide a transcriptome-wide reservoir for mRNAs controlling oogenesis and early embryogenesis during which transcription is silenced. Disrupting these reservoirs ectopically "floods" the oocytes with mRNA molecules whose cytosolic concentrations can increase up to 9 times. Combined with the solidification of RNPs,[10,40,41] coarsening into super-size droplets limits the surface/volume ratio, further reducing interface exchange to restrain the diffusion of the repressed mRNA information.

The ability of condensates to concentrate large cytosolic RNA fractions in small volumes suggests that compaction improves storage capacities. Weighting enrichment by mRNA abundance, we estimate that 50±10 % of the ≈18 million mRNAs condense in 5% of the oocyte volume (Figures S7A, B). This concentrates mRNAs to 10^7 nucleotides per μm^3, which is in the same range as the textbook example of nuclear dsDNA compaction (Figure 7B, Figures S7C, D). Multiplying the volume of a single compacted repressed mRNA[52] by our computed number of P-body mRNAs gives a cumulative volume slightly larger than P-bodies (Figures 7C, Figure S7D, E), suggesting that P-body mRNAs reach the overlap concentration where mRNAs become entangled by occupying overlapping space. Whether RNA entanglement provides a mechanical mechanism to limit the diffusion of mRNAs remains to be tested. Regardless, segregation through phase separations is a thermodynamically driven process and may have the advantage of being an energy-free storage mechanism for the quiescent or stressed cells.

Condensates have no fixed internal stoichiometry. This ensures that their buffering functionality is unaltered even when cellular activity variations are encountered. Although these long-term and large-scale reservoirs contain mRNAs in their tightest state of repression, selective condensation and dissolution quickly sense concentration variations to integrate cellular demands, providing a store that can be quickly mobilized through sequential waves of translation activation and dissolution. In some cell types condensates may not reach sufficient volume to serve as reservoirs, in these instances nanoclusters may function as concentration sensors to ensure that robustly measured saturation concentrations of repressed mRNAs remain available to respond to translation demand. Furthermore, we have shown that even in the absence of macro-condensates, the nanocluster pool can be larger than the soluble pool for a given mRNA species. In addition to RNA nanoclusters,[32–35] protein nanoclusters were also uncovered.[53,54] This raises the question of the unexplored material properties of this nanoscale of organization and opens intriguing new avenues of investigation. Evolution must have shaped the phase diagram of each mRNA to limit mRNA intermixing and selectively adapt supramolecular organizations to individual

molecular functions in a molecular grammar that remains to be deciphered. Beyond stoichiometric control, spatial and biochemical clustering may functionalize every aspect of RNA life,[55,56] underscoring that there is still much to be discovered about the self-organizingprinci ples of transcriptome supra-molecular polymers.

Limitations of the study

The phase transition framework has proven fruitful to uncover key properties of the organization of the transcriptome, however many predictions of the model have not yet been tested. Previously, we characterized mRNP transitions between soluble, semi-liquid and solid states[10], and the condensation of mRNA regulons[3]. Here, we uncovered an mRNA self-buffering mechanism that is dependent on mRNA concentration, repression, and identity. Further testing of the phase transition model predictions should include comprehensive phase diagrams across transcript diversity. Our results also predict that two types of interactions target mRNAs to condensates. We distinguished mRNA recruitment as a client at low concentrations and as a scaffolding component driving its self-assembly at higher concentrations. However, we did not dissect the molecular grammar driving transcriptome multiphase transitions.

We concluded that condensates have buffering properties, however we only touched on the protective role of condensate buffering. Condensate dissolution dramatically impacted mRNA:mRNA and mRNA:protein stoichiometries, but what are the direct consequences on biochemical interaction/reactions? Strategies to block buffering without disrupting condensate assembly remain a serious technical challenge but could further discriminate functionalities. Although condensation-repression systems promote fitness in quiescence, the limits up to which condensates can buffer the accumulation of a single transcript without disrupting the others is unanswered. This is critical to tackle pathological aggregations in degenerative diseases[27,28].

Providing an integrated view of mRNA clustering across spatiotemporal scales remains a key challenge. Building on previous work,[10] cluster size distribution across time-points distinguished the rapid self-assembly of homotypic clusters from their slow co-assembly into heterotypic macro-condensates. Although size, composition and kinetics of assembly discriminated these two populations, the underlying interactions and material properties that distinguish them were not addressed. To map cluster size distributions from single transcript to hundreds of thousands mRNA super-assemblies, we relied on single-molecule fluorescence sensitivity without spatially resolving individual mRNAs. In addition, to increase resolution condensate characterization would further benefit from multiphase live-imaging across time scales, from the sub-second diffusion-reaction, to the week-long coarsening. When computing the degree of P-body enrichment of various RNAs we state that mRNAs were strongly enriched compared to ncRNAs, however our RNA-Seq library preparation was size-biased so small RNAs could not be captured.

ACKNOWLEDGEMENTS

We thank Florence Besse, Patrick Brest, and Stéphane Noselli for valuable discussions and helpful comments on the manuscript. We thank Thomas C. Evans, and the Caenorhabditis Genetics Center (CGC; University of Minnesota) for providing transgenic strains and reagents

used in this study. We thank the iBV PRISM Imaging facility, Bioinformatics facility and Cytometry facility for use of equipment and expertise.

Funding:
CNRS, INSERM and University Côte d'Azur (UCA) for core funding to AH
ATIP-AVENIR starting grant program to AH
ANR, AAP ANR 2020 (ANR-20-CE12-0010), RNADAPT to AH
INSERM, ITMO Cancer to AH
UCA and FRM (FDT202106013219) to AHC
Aides Individuelles Jeunes Chercheurs 2017, UCA, Ville de Nice to SE

AUTHOR CONTRIBUTIONS

AHC, SE and AH conceived the study.
AHC collected and analyzed smFISH and fluorescent protein reporter data, developed smFISH image quantification pipelines, nanoclusters fitting, RNA-Seq - smFISH regressions, *In silico* simulations, and feeding RNAi experiments.
SE prepared animal extracts, performed FAPS purification, RNA extraction, cDNA libraries libraries, and analyzed RNA-Seq data.
MK conducted RNAi microinjection experiments, smiFISH experiments and pre-analysis.
ZY analyzed RNA-Seq data under supervision of DA and SE.
FV generated *spn-4(RNAi)* feeding clone.
ML collected and analyzed production rates from SPN-4:GFP protein reporters, under supervision of AHC.
AL, AB, AO and SR participated to the preparation of samples for the FAPS purifications.
AL and SR conducted the FAPS purifications.
AH collected and analyzed 3'UTR fusion reporters data and embryonic lethality.
AHC, SE, and AH made figures; AHC and AH wrote the original draft; DA, AHC, SE and AH reviewed and edited the manuscript.

COMPETING INTERESTS

Authors declare that they have no competing interests.

MAIN FIGURE TITLES AND LEGENDS

Figure 1. Quantitative modeling of the selective mRNA condensation within oocyte P-bodies.
(**A**) C. *elegans* oogenesis schematic. The PUF-5 translation repressor and CAR-1 cofactor condense repressed mRNAs in P-bodies of quiescent oocytes.[10,45]
(B-B''') Differential condensation of candidate mRNAs in GFP:CAR-1 P-bodies. (**B**) Single molecule Fluorescence *in situ* hybridization (smFISH) confocal imaging from pink insets in (A). (B') mRNA selective partitioning. The blue line is the theoretical relationship between the condensed fraction (CF) and the partition coefficient (PC) (see Methods). (B'') Relationship

between mRNA abundance and condensed mRNA fraction. (B'') Relationship between condensed mRNA fraction and the absolute number of condensed mRNAs. n, number of oocytes analyzed for each transcript; errors bars, ± 95% CI of the mean; *r*, Pearson correlation coefficient. (**C-F**) Purification and sequencing of oocyte P-bodies. (**C**) Schematics of condensate Fluorescence Activated Particle Sorting and RNA-Seq (FAPSeq). (**D**) FAPSeq separation of condensates according to diffraction and fluorescence. (**E**) mRNA copy numbers within/outside condensates from the smFISH calibrated FAPSeq (see Figure S2). (**F**) Distribution of mRNA condensation across transcripts. Median, 65%, range, 10-90%, Q, quartile.

Figure 2. Translationally repressed mRNAs condense into oocyte P-bodies.

(**A-D**) Differential enrichment of RNA classes within P-bodies. RNA-Seq of purified oocyte P-bodies and dissected oocytes were compared. (**A**) P-body depletion of translation machinery RNAs (rRNA, tRNA), and snRNAs and ncRNAs, as compared to mRNAs. (**B**) P-body depletion of small and large ribosomal subunit rRNAs. Mean values ± 95% CI (**C**) P-body enrichment of mRNAs encoding proteins that are not expressed or poorly expressed. mRNAs were binned according to the abundance of their protein product. (**D**) P-body enrichment of PUF-5 and OMA-1/LIN-41 translation repressor mRNA targets as compared to targets of repressors that work earlier or later in development. Schematics of repressor expression patterns at the top. n, number of transcripts. (**E**) P-body depletion of mRNAs encoding housekeeping, structural and metabolic functions, and enrichment of mRNAs encoding regulatory and developmental functions, GO analysis. n, number of transcripts in each category.

Figure 3. Homotypic mRNA nanoclusters co-assemble into multiphase multiscale condensates.

(**A**) Condensate coarsening schematic. (**B**) Spatiotemporal organization of oogenesis. Imaging insets in pink.

(**C-C'**) Confocal imaging of P-body coarsening across oogenesis. (**C**) Comparison of GFP:CAR-1 P-body coarsening in active versus quiescent oogenesis. Estimated time before ovulation in brackets. (**C'**) Size distribution and cumulative volume of P-bodies across quiescent oogenesis time points. n, number of animals.

(**D-D'**) mRNA cluster size distribution in staged diakinesis oocytes. (**D**) smFISH confocal images of single mRNAs (purple arrow), nanoclusters (orange arrow), and macro-condensates (blue arrow). (**D'**) Power law distribution of mRNA clusters and supersize outliers. n, number of animals. Mean values ± 95% CI.

(**E-E''**) Macro-condensate super-assemblies of homotypic nanoclusters. (**E**) Simultaneous labeling of *spn-4* and *glp-1* mRNAs in oocytes revealed single molecules (light green and red arrows), homotypic nanoclusters (either *spn-4* or *glp-1* only, green or red arrows), and heterotypic macro-condensates. (**E'**) *glp-1*:*spn-4* fluorescent intensity ratios within clusters as a function of cluster sizes. Note the discontinuity between the smaller clusters that are homotypic, while macro-condensates are heterotypic. (**E''**) Example of anticorrelation between *spn-4* and *glp-1* mRNA labeling across a macro-condensate confocal section (dotted line in (E)). FU, fluorescence units. (**E'''**) Pearson correlation coefficients computed as in (E'') for the colocalization of 2 mRNAs across macro-condensate confocal sections (see also Figure S5J). Two-color labeling (Cy3 and Cy5) of the same mRNA provided a positive colocalization control. n, number of sections analyzed (number of animals). Mean values ± 95% CI.

(**F-H**) Multiscale and multiphase organization of condensates. (**F**) Confocal imaging of RNA-RNA demixing within condenstes. (**G**) Confocal imaging of protein-protein demixing. (**H**) Super-assembly schematic.

Figure 4. Condensation controls cytosolic mRNA:repressor stoichiometries.

(**A**) Confocal images of stoichiometric changes between the *spn-4* repressed mRNA and CAR-1 repression cofactor across oogenesis. (**B**) Condensate buffering of *spn-4*:CAR-1 stoichiometry. Note disperse phase constant concentrations. n, number of animals (**C**) Robustness and noise of *spn-4* mRNA copy number in the dispersed and condensed phases, respectively. Staged diakinesis oocytes of WT animals were compared. n, number of oocytes (**D**) Confocal images of *spn-4* and *glp-1* mRNAs induced dissolution (*puf-5(RNAi))* in diakinesis oocytes. (**E**) Differential condensation of repressors (CAR-1) and repressed mRNAs (*spn-4*, *glp-1*) in diakinesis oocytes. n, number of oocytes. (**F**) Disruption of mRNA:repressor stoichiometry upon condensate dissolution (*puf-5(RNAi)*). n, number of oocytes. (**G**) Disruption of translation repression upon PUF-5 depletion is quiescence dependent. GFP translation reporters were under the control of *spn-4* and *fog-1* 3'UTR sequences. n, number of animals. (**H**) Embryonic lethality upon PUF-5 depletion is quiescence dependent. n, number of experiments.

Figure 5. Concentration-dependent mRNA clustering buffers repressed mRNA accumulations.

(**A-B**) Models of concentration-dependent phase separations. (**A**) Biomolecules remain soluble at low concentrations but condense past a saturation concentration. (**B**) Self-assembly through homotypic interactions leads to fixed saturation concentrations, while co-assembly through heterotypic interactions usually results in non-fixed saturation concentrations.

(**C-E**) *spn-4* mRNA clustering response to *spn4* concentration variations within quiescent oocytes. (**C**) RNAi manipulated *spn-4* concentrations and smFISH single mRNA quantification (light blue arrow), nanoclusters (dark blue arrow), and GFP:CAR-1 labeled macro-condensates (green arrow). (**D**) Plateauing of single soluble *spn-4* mRNAs at saturation concentration in the dispersed phase induces *spn-4* nanoclustering. Macro-condensate copy numbers scaled with total abundance. (**E**) Bimodal response of *spn-4* partition coefficient to total concentration variations. n, number of oocytes.

(**F**) Transcriptome-wide distribution of mRNA enrichment in oocyte P-bodies depending on transcript copy numbers. Enrichment in P-bodies was computed by comparing the P-body and whole oocyte transcriptomes (P-body/whole oocyte $log_2 FC$), see Figure 1, Figures S2 and S3, Data S1-3). mRNAs were binned according to their total cellular mRNA copy numbers.

Figure 6. Low translation dissolves mRNAs whose clustering is exponential to the degree of repression.

(**A-B**) Models of mRNA translation and condensation control. The translation output depends on either the number of translated mRNAs (**A**) and/or the translation efficiency per mRNA (**B**). Ribosome free mRNAs (non-translated) condense.

(**C-H**) *spn-4* mRNA dissolution upon translation activation. (**C-D**) Confocal imaging of SPN-4:GFP protein accumulation across active and quiescent oogenesis (estimated time before ovulation in brackets). (**C'-D'**) SPN-4 accumulation rates computed from SPN-4:GFP intensity variations across oogenesis. (**E-F**) smFISH confocal imaging of *spn-4* mRNA cluster dissolution. (**E'-F'**) *spn-*

4 mRNA cluster size distribution. (**E''-F''**) Cellular concentration of soluble and condensed *spn-4* mRNAs **(G-H)** *spn-4* clustering is exponential to the degree of translation repression. The fraction of clustered mRNA (G), and the average cluster size distributions (H) are plotted as function of the protein production rate. n, number of oocytes. Mean values ± 95% CI.
(**I-J**) Sequential dissolutions of mRNA condensed phases across oogenesis. (**I**) Schematics of SPN-4 and GLP-1 translation temporal waves. (**J**) smFISH imaging of *spn-4* and *glp-1* mRNAs. (**K**) Quantification of cluster dissolution.

Figure 7. Oocyte P-body multiscale multiphase super-assemblies. (A) Schematic model of the multiscale multiphase control of mRNA stoichiometry depending on mRNA translational activity and sequence identity. See discussion for details. (**B**) Compaction of P-body mRNAs and nuclear dsDNA. mRNA compaction was computed for diakinesis P-bodies. DNA compaction was computed for the nuclei of germ stem cells, that were chosen because of their small nuclear volume (**C**) Model of mRNA compaction within P-bodies. Gyration radius (R_g) of compacted repressed mRNAs estimated elsewhere.[52] Experimental measures suggest mRNA concentration within P-bodies (*c*) are near overlap concentration (*c**), suggesting mRNA entanglement. V_p, volume predicted from multiplying the number of mRNAs within P-bodies by the predicted volume of single repressed mRNA. V_c, cumulative volume of P-bodies experimentally measured.

SUPPLEMENTAL MAIN FIGURE TITLES AND LEGENDS

Figure S1. Single molecule fluorescence in situ hybridization (smFISH) quantifications of mRNA clustering within staged oocytes, related to Figures 1, 3, 4, 5, and 6 (see methods for detailed descriptions and associated quantification controls).
(A) Confocal imaging section of mRNA condensation in arrested oocytes. The translation repression cofactor GFP:CAR-1 labelled P-bodies, and colocalizing *spn-4* mRNA clusters were detected by smFISH.
(**B-C**) Oocyte segmentation. (**B**) Lower and upper oocyte limits were identified along the z-stack acquisition using the derivative maxima and minima of the 90th percentile fluorescence intensity. (**C**) Oocytes were manually segmented along the x-y axis from the maximum intensity projection images. Oocytes were manually staged according to their position along the gonad proximo-distal axis. Oocytes in position -1 are the most differentiated.
(**D-G**) Macro-condensate segmentation using a fluorescence intensity thresholding method. (**D**) Fluorescent intensity normalization. (**E**) Background fluorescence removal. (**F**) Fluorescence intensity thresholding and macro-condensate segmentation and dilatation. (**G**) Labelling and masking of mRNA macro-condensates.
(**H**) Detection of sub-diffractive mRNA foci using FISH-quant [57] after masking macro-condensates that were detected in (D-G). White line delineates the masked macro-condensates, white squares mark the detected positions of sub-diffractive mRNA foci (local maxima or brightness pixel within foci). The Image is a maximum projection of 2 z-planes, hence some detected positions are not shown.
(**I-O**) Quality controls and filters for optimal detection of mRNA foci as adapted from[57]. (**I**) Calibration of the over-detection and under-detection intensity thresholds. The number of detected cytosolic mRNA foci were plotted as a function of the fluorescence intensity detection threshold in a smFISH image of staged oocytes. The curve can be decomposed in 3 segments.

In the first segment (red inset 1), the number of detected foci sharply decreases as the intensity detection threshold increases. In this segment, foci are over detected. In the second segment (red insets 2 and 3), the number of detected foci plateaus. This segment provides an objective criterion to define the optimal detection window: changing the intensity detection threshold in that window has no impact on the number of detected foci. The last segment (red inset 4), where the number of detected foci decreases with the intensity threshold, corresponds to the under-detection window. (**J-L**) Examples of different intensity detection thresholds resulting in over-detection (**J**), optimal detection (**K**), and under-detection (**L**). Green arrows indicate instances of over-detection while blue arrows point to examples of low quality spots. (**M**) Quality control filter based on point spread function (PSF) standard deviations[57]. (**N**) Additional filters for mRNA foci detection. Detected spots are fitted to a theoretical PSF. Sigmas, amplitude, and a minimal distance allowed between fitted spots filter out foci that do not fit a sub-diffractive PSF, detections in the background, and double detections, respectively[57]. (**O**) Quantifications of the number of fitted cytosolic mRNA foci in a representative oocyte: detected (upper), after quality control (middle), and after additional filters (lower).

(**P-S**) Quantifications of *spn-4* mRNA copy numbers (i) as single molecule transcripts in the dispersed phase, (ii) in sub-diffractive nanocluster foci, and (iii) in macro-condensates. (**P**) Calibration of single mRNA fluorescence intensities. Top panel, confocal images of *spn-4* mRNAs within oocytes. To ensure that mRNAs exist in a single molecule form, *spn-4* mRNA concentrations were diluted in oocytes by increasing concentrations of *RNA*i. Bottom panel, fluorescence intensity distribution of *spn-4* mRNA foci. A right-skewed Gaussian in purple was fit to the experimental fluorescence intensity distribution in grey. The relative fluorescence intensities were calibrated so that the maximum of the distribution corresponded to the normalized fluorescence of 1X in the diluted conditions, which corresponds to the fluorescence of a single mRNA molecule. Note that upon dilution almost no foci were detected with a fluorescence intensity equal or superior to 2X. Such a narrow skewed Gaussian distribution with a fluorescence intensity distributed between 0 and 2 X, and centered around 1X, demonstrated our ability to detect mRNAs with single molecule sensitivity. Inset, confocal image of an average single mRNA imaged at high dilution. (**Q**) Control confirming that the fluorescence intensity of single mRNA molecules does not change within versus outside P-body condensates. Following *spn-4(RNAi) to dilute spn-4* mRNAs and ensure single molecules distributions (P), fluorescence intensity distributions were computed either for *spn-4* single molecule foci within CAR-1 condensates (condensed phase), or for *spn-4* single molecule foci within the cytosol (dispersed phase). Of note, other controls confirming that the fluorescence intensity of mRNA molecules does not change between the soluble and clustered states included the physiological or artificial dissolution of macro-condensates and nanoclusters, where the total quantified number of mRNA copies remained unchanged independent of mRNA clustering status (Figures 6F'', 6E'-E'', Figure S6D). See also methods (**R**) Quantification of *spn-4* mRNA copy numbers within the macro-condensates segmented in (F). The average fluorescent intensity of a single transcript computed in (I) was either integrated or cumulated up to reach the fluorescence intensity of the macro-condensates. Both methods gave similar results (see Figure S2O). (**S**) Quantifications of *spn-4* mRNA copy numbers in the dispersed phase (single) and in sub-diffractive nanocluster foci. The fluorescence intensity distribution of sub-diffractive mRNA foci in a staged diakinesis oocytes is shown in grey, a right-skewed Gaussian model fit is shown in blue. The distribution was further decomposed in

a single molecule fit in purple as defined in (I) and a nanocluster fit in orange, so as to compute the number of single mRNAs and the number of mRNA in nanoclusters, respectively.

Figure S2. Scaling the transcriptome-wide FAPS purification and RNA-sequencing method of condensates with single molecule imaging approaches, related to Figure 1.

(A-C) Quantifications, in staged diakinesis arrested oocytes, of the differential condensation of candidate mRNAs in GFP:CAR-1 P-bodies from single molecule Fluorescence *in situ* hybridization (smFISH) confocal imaging (See Fig. S1 and methods for imaging pipeline). (**A**) mRNA selective partition. (**B**) Condensed fractions. (**C**) Condensed copy numbers. n, number of quantified oocytes. errors bars, ± 95% CI of the mean.

(**D**) Computed subcellular compartment volumes in staged diakinesis arrested oocytes (see methods). n, number of quantified oocytes. errors bars, ± 95% CI of the mean.

(**E**) Relationship between mRNA partition coefficients and mRNA condensed fractions in staged diakinesis arrested oocytes. The blue line is the theoretical relationship between the condensed fraction (CF) and the partition coefficient (PC): $PC = CF/(1-CF) * V_d/V_c$ where V_d is the volume of the dilute fraction and V_c is the volume of the condensed fraction as computed in (D). *r*, Pearson correlation coefficient.

(**F-I**) Transcriptomics analysis of the FAPS purified diakinesis oocytes P-bodies. (**F**) The principal component analysis (PCA) separates the transcriptomes of FAPS purified diakinesis oocyte P-bodies, from the pre-sorted fractions (whole animal extracts) and the dissected diakinesis oocytes. n=3 independent biological replicates (**G**) Differential enrichment of RNAs in the FAPS purified oocyte P-bodies as compared to the pre-sorted whole animal extracts. The dot plot represents all RNAs from the RNA-Seq analysis. Note that somatic enriched transcripts labeled in pink are strongly depleted from oocyte P-bodies, validating the purification quality. (**H**) The distribution of RNA enrichment in oocyte P-bodies was computed from (G). (**I**) Differential enrichment of RNAs in the FAPS purified diakinesis oocyte P-bodies as compared to the whole diakinesis oocyte transcriptome. RNA relative expression levels in oocytes were computed in FPKM.

(**J-L**) Correlations between the imaging (smFISH) and FAPS purification-RNA-sequencing (FAPSeq) methods for the quantification of mRNA subcellular localizations. (**J**) Correlation for the mRNA enrichment in P-bodies. (**K**) Correlation for the mRNA abundance in oocyte P-bodies. (**L**) Correlation for the mRNA abundance in oocytes. n, number of animals analyzed per mRNA for the smFISH. n, number of independent biological replicates for the FAPSeq. errors bars, ± 95% CI of the mean. r^2, R-squared of linear regression model (blue line). Shaded areas, 95% CI of linear regressions.

(**M-P**) Distributions of mRNA enrichment in P-bodies. (**M**) mRNA enrichment was computed by comparing the oocyte P-body transcriptome to the whole oocyte transcriptome. To avoid bias from the technical dispersion because of low sequencing read counts for poor abundance transcripts, only transcripts in the top 50% of expression levels were plotted (**N**) Comparison of the cumulative distribution of mRNA relative enrichment in P-bodies depending on mRNA expression levels in oocytes. mRNAs were binned according to their expression levels in oocytes (FPKM), demonstrating that mRNA enrichment in P-bodies increases with mRNA abundance. The large dispersion of the lowest mRNA abundance bins is technical, and reflects dispersion noise due to the low sequencing read counts. (**O**) smFISH calibrated distribution of mRNA enrichment in P-bodies. mRNA enrichment was computed using the S2J linear regression.

smFISH integrative and cumulative methods to compute mRNA condensation gave similar results. (**P**) Distribution of the percentage of condensed mRNAs as computed from the integrated method in (O), including low abundance transcripts.

Figure S3. Features of condensed mRNAs, related to Figure 2.

(**A**) mRNA length comparisons between P-bodies and P-granules. (**B**) Absence of nucleotide compositional bias for P-body mRNAs. mRNAs were split in 5 bins according to their enrichment in P-bodies, and the % of A, U, C, G nucleotides was computed for 5'UTRs, CDS, and 3'UTRs.

Figure S4. *In silico* simulations and corrections of experimental measures for the quantification of *spn-4* mRNA clustering, related to Figures 1, 3, 4, 5, and 6.

(**A**) Synthetic images of single mRNA foci randomly placed at increasing concentrations within the oocyte volume. Lower panels are one-plane magnifications of the inset. Note that because of the lack of imaging resolution to separate the mRNAs that are randomly placed at high density, some mRNAs artificially appear to cluster in brighter foci towards higher concentrations despite the absence of clustering within the simulation input parameters, demonstrating that mRNA clusters can be overestimated, as further quantified in (B). (**B**) Comparison of *spn-4* mRNA distribution across cluster sizes in simulated images (*in silico*) versus experimental results. Experimental distributions of cluster sizes were computed at low (*spn-4(RNAi)*) and high (WT animals) mRNA concentrations, either in active oocytes or arrested diakinesis oocytes that were staged in position -4 along the gonad proximo-distal axis. *In silico* distributions as simulated in (A) were computed for concentrations matching the experimental measures. See Figure S1 for the quantification pipeline of smFISH experimental and simulated images, and Figure 5C for the experimental imaging *of spn-4* in RNAi conditions. Note that in the simulation, the nanoclusters detected at high concentrations were artefacts because single mRNAs were not well separated because of imaging resolution limits as shown in (A). n, number of animals analyzed for quantifications. n, number of replicates for the simulation. (**C**) Comparison of *spn-4* mRNA cluster size distributions at various mRNA concentrations between simulated images (left panel) and experimental results (right panel). *spn-4* mRNA concentrations were experimentally varied using an RNAi approach, for imaging see Figure 5C. Note the concentration threshold effect on mRNA clustering in the experimental data that is not detected in the simulation. (**D**) Experimental quantifications of *spn-4* mRNA distribution across cluster sizes with a correction from the *in silico* simulation. Corrections subtracted the artificial clusters that were detected in the simulation at similar concentrations, and that were instead accounted as single soluble transcripts. n, number of animals. Mean values ± 95% CI. (**E**) smFISH quantifications of single dispersed mRNAs and mRNA nanoclusters within simulated images versus experimental images. (**F**) Corrected experimental quantifications of single dispersed mRNAs and mRNA nanoclusters. Corrections subtracted the artificial clusters detected in the simulation at similar concentrations that were instead accounted as single soluble transcripts.

Figure S5. Controls for the smFISH imaging of mRNA demixing, related to Figure 3.

(A-H) Bleed through controls for the two-color smFISH imaging of mRNAs. (**A-C**) Bleed through controls for the demixing of *spn-4* and *glp-1* mRNAs within macro-condensates. (**A**) *spn-4* and *glp-1* mRNAs were fluorescently labelled with Cy3 and Cy5 fluorophores. (**B**) Bleed through control for Cy3 in the absence of Cy5 labeling. (**C**) Bleed through control for Cy5 in the absence

of Cy3 labeling. (**D-F**) Bleed through controls for *spn-4* and *glp-1* mRNAs in the cytosol. (**D**) *spn-4* and *glp-1* mRNAs were fluorescently labelled with Cy3 and Cy5 fluorophores. (**E**) Bleed through control for Cy3 in the absence of Cy5 labeling. (**F**) Bleed through control for Cy5 in the absence of Cy3 labeling. Fluorescence intensity scales are presented above images. Laser intensities were matched. (**G**) Quantifications of Cy3 bleed-through within the Cy5 collection channel. (**H**) Quantifications of the Cy5 bleed-through within the Cy3 collection channel.
(I-K) smFISH imaging and controls for mRNA-mRNA demixing within quiescent diakinesis oocytes. **(I)** smFISH images of mRNA-mRNA demixing within macro-condensates. *spn-4*, *glp-1* and *mbk-2* mRNAs are shown. Right panels, fluorescent intensity distributions across xy axis as shown as white dashed line on merged panels. (**J**) Controls for mRNA-mRNA demixing within macro-condensates. Top panel imaging of *spn-4* and *glp-1* mRNA demixing. Middle and bottom panels are positive controls for mRNA colocalization, the same mRNA, either *spn-4* or *glp-1,* was labelled with two colors. (**K**) Quantification controls for the demixing between homotypic clusters. n, number of analyzed clusters (number of animals). FU: fluorescence units.

Figure S6. Condensation quantifications for the repression cofactor GFP:CAR-1, and the *spn-4* and *glp-1* repressed mRNAs, related to Figures 4 and 5.
(**A-B'**) Quantifications of the translation repression cofactor GFP:CAR-1 condensation in arrested diakinesis oocytes from confocal z-stack acquisitions. (**A**) Confocal images of GFP:CAR-1 depletion (*car-1(RNAi)*) in arrested diakinesis oocytes. (**A'**) Control for the GFP:CAR-1 fluorescence specificity and quantitative sensitivity. The detected fluorescence in the dispersed phase (outside of condensates) dropped to ≈0 upon CAR-1 depletion (*car-1(RNAi)*). (**A''**) Quantifications of the GFP:CAR-1 cumulative fluorescence intensity in the dispersed versus condensed phase. (**B**) Confocal images of GFP:CAR-1 condensates dissolution upon PUF-5 depletion (*puf-5(RNAi)*). (**B'**) Control for the condensed versus soluble GFP:CAR-1 quantifications. The total GFP:CAR-1 measured concentration remained unchanged as GFP:CAR-1 was released to the cytoplasm upon the *puf-5(RNAi)* induced dissolution of condensates, confirming the absence of bias in the quantification of condensed versus soluble molecules.
(**C-D**) Quantifications of the repressed mRNAs (*spn-4*, *glp-1*) condensation in oocytes from confocal z-stack acquisitions of smFISH images (see Figure S1 for quantification pipeline details). (**C**) Confocal images of *spn-4* mRNA depletion (*spn-4(RNAi)*). Magnifications are in insets. (**C'**) Control for the *spn-4* mRNA detection fluorescence specificity and quantitative sensitivity. The detected cytosolic *spn-4* mRNA concentrations dropped to ≈0 upon *spn-4* mRNA depletion (*spn-4(RNAi)*). (**C''**) Quantifications of *spn-4* mRNA molecules, in mRNA copy number, within the dispersed and condensed phases. (**D**) Image quantifications of *spn-4* and *glp-1* mRNAs induced dissolution (*puf-5(RNAi))* in arrested oocytes (see Figure 4D for corresponding smFISH confocal images). Left panel, control for the condensed versus soluble mRNA quantifications. The total cellular mRNA density remained unchanged upon the *puf-5(RNAi)* induced dissolution of mRNA condensates, confirming the absence of bias in the quantification of condensed versus soluble molecules. Right panel, quantifications of cytosolic mRNA concentration increase upon mRNA release from condensate dissolution.

Figure S7. Transcriptome-wide quantification of mRNA enrichment and compaction within oocyte P-bodies, related to Figure 7.

(**A-B**) mRNA condensation estimates from the smFISH calibrated FAPSeq (see method details). (**A**) Condensation of half of mRNAs within 5% of the cellular volume. The number of condensed mRNA (Data S3) was computed from the smFISH calibrated FAPSeq (see method details). Subcellular volumes were computed in S2D (**B**) Local mRNA concentrations within and outside condensates. (**C**) mRNA length distributions across transcripts that were used to compute mRNA compactions in (C) and (D). (**D**) Schematic representation of the computing of mRNA compaction within condensates. DNA compaction was computed for germ stem cell nuclei, which were chosen because of their high compaction. RNA compaction was computed for a diakinesis oocyte P-body (**E**) Estimation of the cumulative volume that would be occupied by repressed P-body mRNAs, taking into account the gyration radius of repressed mRNAs as defined by[52] and the number of P-body mRNAs of the current study.

STAR Methods

Robust sorting and buffering within condensates control transcriptome stoichiometries

Andrés H. Cardona[1]*, Szilvia Ecsedi[1]*, Mokrane Khier[1], Zhou Yi[1], Alia Bahri[1], Amira Ouertani[1], Florian Valero[1], Margaux Labrosse[1], Sami Rouquet[1], Stéphane Robert[2], Agnes Loubat[1], Danielle Adekunle, Arnaud Hubstenberger[1#]

[1]Université Côte D'Azur, CNRS, Inserm, iBV, Nice, France.
[2] Université Aix Marseille, Inserm, INRAE, C2VN, Marseille, France.
[3] Université Côte D'Azur, CNRS, Inserm, IRCAN, Nice, France.

*These authors contributed equally to this work.

[#]Correspondence to: Arnaud.HUBSTENBERGER@univ-cotedazur.fr

Contents:

872 **KEY RESOURCES TABLE**
873

REAGENT or RESOURCE	SOURCE	IDENTIFIER
Bacterial and virus strains		
E. coli OP50	Caenorhabditis Genetics Center	WormBase ID: WBStrain00041969; https://cgc.umn.edu/strain/OP50
E. coli HT115(DE3)	Caenorhabditis Genetics Center	WormBase ID: WBStrain00041080; https://cgc.umn.edu/strain/HT115(DE3)
Chemicals, peptides, and recombinant proteins		
RNaseOUT Recombinant Ribonuclease Inhibitor	Invitrogen (Thermo Fisher Scientific)	Cat#10777019
PBS, pH 7.4 (flow cytometry grade)	ThermoFisher Scientific	Cat#A1286301
Zirconium Oxide Beads 1.0 mm RNase Free	Next Advance	Cat#ZROB10-RNA
SUPERase In RNase Inhibitor (20U/uL)	Invitrogen (Thermo Fisher Scientific)	Cat#AM2696
HEPES	Sigma-Aldrich (Merck)	Cat#H3375; CAS: 7365-45-9
Triton X-100	Sigma-Aldrich (Merck)	Cat#X100; CAS: 9036-19-5
Poly-L-Lysine solution (0.1%)	Sigma-Aldrich (Merck)	Cat#P8920; CAS: 25988-63-0
Gelatine solution (2%)	Sigma-Aldrich (Merck)	Cat#G1393; CAS: 9000-70-8
Chromium (III) Potassium Sulfate	Merck	Cat#1.01036; CAS: 7788-99-0
Sodium phosphate dibasic dodecahydrate	Sigma-Aldrich (Merck)	Cat#71649; CAS: 10039-32-4
Sodium Phosphate, Monobasic	Merck	Cat#567545; CAS: 10049-21-5
Formaldehyde solution	Sigma-Aldrich (Merck)	Cat#F8775; CAS: 50-00-0
Qiagen Proteinase K (>600 mAU/ml)	Qiagen	Cat#19131; CAS: 39450-01-6
SSC buffer (20x)	Jena Bioscience	Cat#BU-118L
Formamide (≥99.5%)	Sigma-Aldrich (Merck)	Cat#F9037; CAS: 75-12-7
Stellaris RNA FISH Hybridization Buffer	LGC Biosearch Technologies	Cat#SMF-HB1-10
ProLong Glass Antifade Mountant	Invitrogen (Thermo Fisher Scientific)	Cat#P36980
Peptone	Thermo Fisher Scientific	Cat#211677
Yeast extract BioChemica	ITW Reagents	Cat#A1552
Sodium chloride	Sigma-Aldrich (Merck)	Cat#S7653; CAS: 7647-14-5
Agar, Bacteriological grade	Thermo Fisher Scientific	Cat#443572500; CAS: 9002-18-0
Magnesium sulfate	Sigma-Aldrich (Merck)	Cat#M7506; CAS: 7487-88-9

Calcium chloride hexahydrate	Sigma-Aldrich (Merck)	Cat#442909; CAS: 7774-34-7
Potassium phosphate monobasic	Sigma-Aldrich (Merck)	Cat#P979; CAS: 7778-77-0
IPTG	Sigma-Aldrich (Merck)	Cat#I6758; CAS: 367-93-1
Cholesterol	Sigma-Aldrich (Merck)	Cat#C8667; CAS: 57-88-5
Carbenicillin	Condalab	Cat#6803
Critical commercial assays		
miRNeasy FFPE kit	Qiagen	Cat#217504
Agilent RNA 6000 Pico Kit	Agilent	Cat#5067-1513
SMARTer Stranded Total RNA-Seq Kit v2 - Pico	Takara	Cat#634411
Agilent High Sensitivity DNA Chips	Agilent	Cat#5067-4626
Qubit RNA HS Assay Kit (Invitrogen)	Invitrogen (Thermo Fisher Scientific)	Cat#Q32852
Qubit dsDNA HS Assay Kit (Invitrogen)	Invitrogen (Thermo Fisher Scientific)	Cat#Q32851
Illumina TruSeq HT assay	Illumina	Cat#FC-121-2003
Deposited data		
RNA-Seq raw data	This paper	GEO: GSE213222
HTSeqCounts raw reads	This paper	GEO: GSE213222
RNA relative enrichment within oocyte P-bodies	This paper	Data S1
RNA-Seq abundances	This paper	Data S2; GEO: GSE213222
Estimated condensed and dissolved mRNA copy numbers in oocytes	This paper	Data S3
GO analysis of P-body enriched and depleted mRNAs	This paper	Data S4
smFISH raw micoscopy data	This paper; Mendeley data	https://doi.org/10.17632/ys7pzfxk9g.1; https://doi.org/10.17632/n7sf6f4c22.1; https://doi.org/10.17632/gcbvzm5kzg.1
Fluorescent reporters raw microscopy data	This paper; Mendeley data	https://doi.org/10.17632/5jt3m3twsh.1
Protein expression of maternal mRNAs in oocytes	Merritt et al.[46]	Table S2
mRNA targets of FBF-1 and GLD-1	Hu et al.[58]	http://POSTAR.ncrnalab.org
mRNA targets of OMA-1 and LIN-41	Tsukamoto et al.[50]	https://academic.oup.com/genetics/article/206/4/2007/6072647#supplementary-data
mRNA targets of PUF-5	Stumpf et al.[49]	https://rnajournal.cshlp.org/content/14/8/1550/suppl/DC1
Experimental models: Organisms/strains		
C. elegans: *fog-2(q71)* V	Caenorhabditis Genetics Center	WormBase ID: WBStrain00004538; https://cgc.umn.edu/strain/CB4108

C. elegans wild isolate	Caenorhabditis Genetics Center	WormBase ID: WBStrain00000001; https://cgc.umn.edu/strain/N2
C. elegans: $P_{pie\text{-}1}$*::gfp::car-1::UTR*$^{pie\text{-}1}$	Squirrell et al.[59]	N/A
C. elegans: *fog-2(q71)*; $P_{pie\text{-}1}$*::gfp::car-1::UTR*$^{pie\text{-}1}$	This paper	N/A
C. elegans (TE73): *fog-2(q71)*; *car-1(oc8[car-1:gfp:FLAG])*	gift of T. Evans	N/A
C. elegans (TE51): $P_{pie\text{-}1}$*::gfp::car-1::UTR*$^{pie\text{-}1}$*;*$P_{nmy\text{-}2}$*::pgl-1::mrfp*	Hubstenberger et al.[10]	N/A
C. elegans (TE71): *fog-2(q71)*; $P_{pie\text{-}1}$*::gfp::car-1::UTR*$^{pie\text{-}1}$*;*$P_{nmy\text{-}2}$*::pgl-1::mrfp*	Hubstenberger et al.[10]	N/A
C. elegans (DG4158): *spn-4(tn1699[spn-4::gfp::3xflag])*	Tsukamoto et al.[50]; Caenorhabditis Genetics Center	WormBase ID: WBStrain00005730; https://cgc.umn.edu/strain/DG4158
C. elegans: *fog-2(q71); spn-4(tn1699[spn-4::gfp::3xflag])*	This paper	N/A
C. elegans (DG4215): *puf-5(tn1726[gfp::3xflag::puf-5])*	Tsukamoto et al.[50]; Caenorhabditis Genetics Center	WormBase ID: WBStrain00005742; https://cgc.umn.edu/strain/DG4215
C. elegans: *fog-2(q71); puf-5(tn1726[gfp::3xflag::puf-5])*	This paper	N/A
C. elegans: $P_{pie\text{-}1}$*::GFP::H2B::3'UTR*$^{fog\text{-}1}$ *+ unc-119(+)*	Caenorhabditis Genetics Center	WormBase ID: WBStrain00022333; https://cgc.umn.edu/strain/JH2423
C. elegans: $P_{pie\text{-}1}$*::GFP::H2B::3'UTR*$^{spn\text{-}4}$ *+ unc-119(+)*	Caenorhabditis Genetics Center	WormBase ID: WBStrain00022302; https://cgc.umn.edu/strain/JH2311
C. elegans: *fog-2(q71);* $P_{pie\text{-}1}$*::GFP::H2B::3'UTR*$^{fog\text{-}1}$ *+ unc-119(+)*	This paper	N/A
C. elegans: *fog-2(q71);* $P_{pie\text{-}1}$*::GFP::H2B::3'UTR*$^{spn\text{-}4}$ *+ unc-119(+)*	This paper	N/A
Oligonucleotides		
spn-4 smiFISH probes	This paper (synthesized by IDT)	Table S3
glp-1 smiFISH probes	This paper (synthesized by IDT)	Table S4
puf-5 smiFISH probes	This paper (synthesized by IDT)	Table S5
tbb-2 smiFISH probes	This paper (synthesized by IDT)	Table S6
pccb-1 smiFISH probes	This paper (synthesized by IDT)	Table S7
complementary FLAPx probes	This paper (synthesized by IDT)	Table S8
Recombinant DNA		
L4440 vector	Kamath et. al.; Timmons et al.[60–62]	Addgene Plasmid #1654 (pPD129.36)
puf-5(RNAi) in L4440 vector	Hubstenberger et al.[63]	N/A
car-1(RNAi) in L4440 vector	Hubstenberger et al.[39,63]	N/A
Software and algorithms		

R 4.1.2	R	https://www.r-project.org/
RStudio 2021.09.1+372	RStudio; Posit	https://www.rstudio.com; https://posit.co/downloads/
Fiji 2.9.0/1.53t	Schindelin et al.[64]	https://imagej.net/software/fiji/
MATLAB R2018b	MathWorks	https://www.mathworks.com/
FISH-quant	Mueller et al.; Tsanov et al.[47,48]	https://bitbucket.org/muellerflorian/fish_quant/src/master/
Oligostan	Mueller et al.; Tsanov et al.[47,48]	https://bitbucket.org/muellerflorian/fish_quant/src/master/Oligostan/
bcl2fastq	Illumina	https://support.illumina.com/sequencing/sequencing_software/bcl2fastq-conversion-software.html
FastQC	Andrews et al.[65]	https://qubeshub.org/resources/fastqc
Galaxy server	Goecks et al.[66]	https://usegalaxy.org/
HISAT2 v2.1.0	Kim et al.[67]	http://daehwankimlab.github.io/hisat2/; https://github.com/DaehwanKimLab/hisat2
StringTie	Pertea et al.[68]	https://ccb.jhu.edu/software/stringtie/
HTseq count	Anders et al.[69].	https://htseq.readthedocs.io/en/release_0.11.1/count.html
SamTools	Li et al.[70]	http://www.htslib.org/
IGV v2.6.1	Robinson et al.; Thorvaldsdóttir et al.[71,72]	https://software.broadinstitute.org/software/igv/home
Bioconductor 3.14	Huber et al.[73]	https://bioconductor.org/
DESeq2	Love et al.[74]	https://bioconductor.org/packages/release/bioc/html/DESeq2.html
GenomicRanges	Lawrence et al.[75,76]	https://bioconductor.org/packages/release/bioc/html/GenomicRanges.html
rtracklayer	Lawrence et al.[75,76]	https://bioconductor.org/packages/release/bioc/html/rtracklayer.html
Panther (release 20191216)	Panther	http://www.pantherdb.org/

Original code: fluorescent reporters quantification, smFISH image quantification, smFISH image simulation	This paper; Mendeley data; GitHub	https://doi.org/10.17632/8jvrnztdvc.1; https://github.com/CardonaEA/code-image-analysis-c-elegans
Other		
MoFlo Astrios EQ	Beckman Coulter	Cat#B25982
Qubit 4.0	Thermo Fisher Scientific	Cat#Q33238
Agilent 2100 BioAnalyser	Agilent	Cat#G2939BA
Zeiss LSM 880	Zeiss	N/A
Zeiss ZEN (black edition) software	Zeiss	N/A

874

RESOURCE AVAILABILITY

Lead contact

Further information and requests for resources and reagents should be directed to and will be fulfilled by the lead contact, Arnaud Hubstenberger (Arnaud.HUBSTENBERGER@univ-cotedazur.fr).

Materials availability

All unique materials and reagents generated in this study are available from the lead contact with a completed material transfer agreement.

Data and code availability

- RNA-seq raw data have been deposited at GEO and are publicly available as of the date of publication. Accession number is listed in the key resources table. Relative enrichment, abundance, copy number, and GO terms of oocyte mRNAs are provided with this paper as Data S1 to S4. Raw microscopy data from smFISH and fluorescent reporters have been deposited at Mendeley Data and are publicly available as of the date of publication. DOIs are listed in the key resources table. This paper analyzes existing, publicly available data. These sources and identifiers for the datasets are listed in the key resources table. All data reported in this paper will be shared by the lead contact upon request.
- All original code has been deposited at Mendeley Data and GitHub and is publicly available as of the date of publication. DOIs and identifiers are listed in the key resources table.
- Any additional information required to reanalyze the data reported in this paper is available from the lead contact upon request.

EXPERIMENTAL MODEL AND STUDY PARTICIPANT DETAILS

C. elegans strains, maintenance and RNAi

C. elegans strains were maintained by standard methods on feeding plates seeded with OP-50 E.*coli* [77]. All transgenic strains were crossed either into hermaphrodites *N2* (Bristol wild-type strain) or feminized CB4108 (*fog-2(q71)*) backgrounds that are depleted of sperm. Strains are listed in Table S2. To deplete the expression of genes of interest, RNAi in C. *elegans* was performed as previously described, either by feeding [61,63] or injecting (dsRNA) [78]. Briefly, for the feeding method, synchronized L4 larvae were grown at 20°C for 48 h on HT115(DE3) E.*coli* strains expressing the dsRNA of interest from an L4440 plasmid, whose inserted sequence was directly cloned from the corresponding C. *elegans* cDNA [61,63]. A random dsRNA that is absent from the *C. elegans* genome was expressed from the L4440 plasmid as a *mock(RNAi)* control. For the alternative direct injection of double-stranded RNA (dsRNA) in the gonad [78], worm gonads were analyzed 48 h post injection.

METHOD DETAILS

Live-imaging of GFP:protein fusions

Live *C. elegans* nematodes were anaesthetized with 50 mM NaN_3 in Phosphate Buffer Saline (PBS), and transferred between slides and coverslips to 4% agarose pads, and imaged on a Zeiss LSM 880 microscope with a Plan-Apochromat 40x/1.4 Oil DIC M27 objective and AiryScan SR module. Imaging was conducted in the first 15 min of anesthesia. To avoid signal interference from the intestine, images of GFP-tagged proteins were acquired from the gonad closer to the objective. 3D image data was obtained using Zeiss ZEN software and a 488 nm laser (BP 420-480 + BP 495-550). Z-stacks were acquired with a step-size of 0.5 µm (2.0 optical zoom, 0.66 µs pixel dwell, master gain of 750, digital offset of 1, 79 µm pinhole) and processed using the in-built Zeiss Airyscan Processing algorithm. Images were acquired across half of the oocyte depth, from cortex to nuclei (~ 6 µm), to prevent differences in signal intensity due to tissue depth.

Single molecule FISH (smFISH)

smFISH probes preparation

Our smFISH method to visualize mRNA subcellular localization with single-molecule sensitivity in formaldehyde fixed *C. elegans* gonads was adapted from.[48] For that purpose, we designed 37 to 48 smFISH probes per tested transcript using the Oligostan R script.[48] Primary probes carried FLAPx extensions (Tables S3-S7) that anneal to complementary FLAPx secondary probes labeled with two Cy3 fluorophores (Table S8) to fluorescently label target mRNAs. The theoretical expected amplified fluorescence would correspond to a minimum 37x2 fluorophore per single hybridized transcript. For smFISH probes preparation, primary probes (~60nM/probe) were mixed with labeled FLAPx secondary probes (5µM) in TSE buffer (10 mM Tris; 1 mM EDTA; 100 mM NaCl; pH 7.95), and annealed as previously described[79].

Sample preparation and hybridization

Briefly, synchronized *C. elegans* adult gonads were dissected on coated coverslips (0.05% Poly-L-lysine; 0.2% gelatin; 0.02% $CrKO_8S_2$), fixed for 5 min in 4% formaldehyde in Phosphate Buffer (77.4mM Na_2HPO_4; 4mM NaH_2PO_4) at RT, and freeze-cracked as previously described [39]. After freeze-cracking, gonads were secondary fixed in 4% formaldehyde for 20 min at RT, washed in Phosphate Buffer, permeabilized in 70% ethanol overnight at 4°C, and washed again in Phosphate Buffer. Next, to unmask RNAs from bound proteins, and facilitate probe hybridization, samples were treated with proteinase K (QIAGEN, 4 µg/ml in 2xSSC) for 5 min at RT, followed by a secondary fixation in 4% formaldehyde for 15 min to restore crosslinks disrupted by the proteinase K, then washed twice in Phosphate Buffer and once in 15% formamide in 1xSSC. For hybridization, samples were preincubated in 15% formamide in 1xSSC for 15 min at RT, then hybridized for 16 h at 37°C with 2.5 µl of smFISH probes as prepared above and further diluted in 100 µl of Stellaris RNA FISH Hybridization Buffer (LCG Biosearch Technologies) containing 10% formamide. For mounting, samples were incubated twice in 25% formamide in 1xSSC for 30 min at 37°C, washed twice in Phosphate Buffer, mounted on slides using ProLong Antifade (Invitrogen), and cured for 60 h before imaging.

smFISH imaging

smFISH images of *C. elegans* oocytes were acquired on a Zeiss LSM 880 microscope with a Plan-Apochromat 63x/1.4 Oil DIC M27 objective. Images were processed with the AiryScan super-resolution (SR) module, using Zeiss ZEN software. A 561 nm laser (BP 570-620 + LP 645 + SBS SP 615) was used for mRNA detection, and a 488 nm laser (BP 420-480 + BP 495-550)

for GFP:CAR-1 signal to assess mRNA localization into P-bodies that are GFP:CAR-1 labelled. For AiryScan acquisitions, images were taken with a *z*-spacing of 0.185 µm, 2.0 optical zoom, 0.66 µs pixel dwell, average of 4, master gain of 750, digital offset of 1, and 143 µm pinhole. For Fast AiryScan aquisitions, z-stacks were obtained with a step-size of 0.250 µm, 1.8 optical zoom, 0.52 µs pixel dwell, average of 4, master gain of 750, digital offset of 1, and 384 µm pinhole. Multiphase 3D smFISH images were processed using the in-built Zeiss Airyscan Processing algorithm.

smFISH image analysis of mRNA clustering

Image quantifications of condensed and dissolved mRNAs were performed with MATLAB R2018b. Our image analysis approach is detailed below and in Figure S1.

Segmentation of oocyte boundaries and staging

To conduct mRNA clustering analysis in smFISH images of staged diakinesis oocytes, the first segmentation delineated oocyte boundaries within the dissected gonads (Figure S1A). A pre-processing step defined the upper and the lower limits of oocytes within the z-stack acquisition, the z-upper (Z_{up}) and z-lower (Z_{lo}) oocyte boundaries. For that purpose, the 90th percentile of the fluorescence intensities was computed for each stack along the z-axis, and the partial derivative (numerical gradient) of the 90th percentiles was calculated using the MATLAB function *gradient*. The z-stack positions corresponding to the derivative's maximum and minimum defined the oocyte lower and upper limits by detecting the transition between background and oocyte signal (Figure S1B). Next, to set oocyte limits along x- and y-axis, the oocyte contours were identified manually in maximum intensity projections of the z-stacks (Figure S1C). Following oocyte segmentations, each oocyte was staged according to its position along the proximo-distal axis of the gonad. The most proximal oocyte, ranked in position -1, is the most mature oocyte paused for fertilization. Other oocytes were numbered according to their proximo-distal positions, where the -4 oocyte is more differentiated than the -5 along the gonad spatiotemporal axis (Figure S1C).

Segmentation of mRNA condensates

The second segmentation step was used to identify the mRNA condensates that were larger than 32 pixels in size (~0.02 µm^3) in each segmented oocyte (Figures S1D-S1F). This thresholding segmentation method was applied in the GFP:CAR-1 and the mRNA channels, which are both independent and overlapping markers of condensates (Figure S1A). Briefly, pixels with intensities lower than the image's 90th quantile were filtered out as background. Then, 2-by-2-by- pixel regions were normalized (N) between 0 (≈cytoplasm) and 1 (≈condensates), according to each plane maximum intensity (Figure S1D):

$$N_{i,j} = \begin{cases} \dfrac{\ln \bar{I}_i}{\ln \max\left(I_{z_{lo}}\right)}, & j < Z_{lo} \\ \dfrac{\ln \bar{I}_i}{\ln \max\left(I_j\right)}, & Z_{lo} \le j \le Z_{up} \\ \dfrac{\ln \bar{I}_i}{\ln \max\left(I_{z_{up}}\right)}, & j > Z_{up} \end{cases}$$

where N is the normalized value of a 2-by-2-by-1 region, i denotes x, y coordinates, j is the z-stack, $\bar{I}$ is the average intensity, and I represents intensities at stack j, z-upper (Z_{up}) or z-lower (Z_{lo}) oocyte boundaries.

After normalizing the fluorescence intensity (Figure S1D), the local fluorescence background was removed (Figure S1E). To this end, continuums of weak normalized fluorescent intensities (N < 0.65) were identified using the 3D-connected component function. Large 3D-connected regions (> 5000 pixels) with low N (N < 0.65) were defined as local background and were therefore filtered out (Figure S1E). Next, to segment mRNA condensates, z-stack regions that passed a specific intensity threshold (N > 0.6) were labeled using the 3D-connected component function. 3D-connected objects larger than 0.02 µm^3 were considered as macro-condensates. To ensure that condensate edges were included, each macro-condensate binary mask was dilated using MATLAB function *imdilate* (Figure S1F).

Identification of mRNA sub-diffractive foci

After delineating oocytes and segmenting the largest mRNA condensates (see above), the third step identified sub-diffractive fluorescent foci, that represent both single mRNAs and mRNA nanoclusters, using the open-source MATLAB package FISH-quant.[47,48] Briefly, the raw smFISH signal was enhanced by a two-step convolution of the image with Gaussian Kernels using the FISH-quant function *img_filter_Gauss_v5* as detailed.[47,48] To limit detection to the sub-diffractive foci, mRNA macro-condensates were masked (Figure S1G). Next, to quantify foci depending on oocyte differentiation stages, oocyte limits along x- and y-axis as defined above were used to generate compatible image outlines files readable by the FISH-quant software. Finally, cytosolic mRNA foci were detected (3D local maximum) and filtered in FISH-quant (Figure S1H). To avoid single mRNA over- or under- detections, the applied filters included the determination of the Fluorescence intensity detection threshold (Figure S1I-L), the quality control filter (Figure S1M), the fit to the theoretical point-spread function (PSF) (Figure S1N), filters whose respective impacts were quantified (Figure S1O) as previously described.[47,48]

Single molecule calibration

To quantify smFISH images with single molecule sensitivity it was critical to define the fluorescence intensity distribution of single mRNA molecules. For that purpose, the intensity distribution of sub-diffractive mRNA foci was quantified at very low RNA concentrations to ensure that all mRNAs exist as single molecules (Figure S1P). mRNA foci were detected with the open-source MATLAB package FISH-quant.[47,48] The point-spread function (PSF) and amplitude of single molecules were defined in images with mRNA concentrations lower than 0.5 mRNAs/µm^3. Such low concentrations were obtained either by depleting most RNAs by RNAi (Figure S1P), or by restricting the analysis at the onset of transcriptional activation in the distal tip regions of the gonad when transcripts have not yet reach high concentrations (up to 30 to 50 µm from the distal gonad tip cell). Both methods yielded almost identical distributions of intensities for single mRNAs. A right-skewed Gaussian was fit to obtain a function that describes the distribution of single mRNA molecule amplitudes:

$$\hat{A}(x) = h * \phi(x)\Phi(\alpha x)$$

where $\hat{A}$ is the kernel density estimation (KDE) for the amplitude of individual mRNA molecules, h represents the height of the distribution, and $\phi(x)\Phi(\alpha x)$ is the skewed Gaussian function with the shape parameter α:

$$\phi(x)\Phi(\alpha x) = e^{-\frac{1}{2}\left(\frac{x-centroid}{sd}\right)^2} * \left[\operatorname{erf}\left(\frac{\alpha\left(\frac{x-centroid}{sd}\right)}{\sqrt{2}}\right) + 1\right]$$

The fitting was performed with the MATLAB function *lsqcurvefit*, thus yielding estimates of h, α, $centroid$ and sd (standard deviation). After defining the relative 1X fluorescence intensity at which the skewed Gaussian distribution of single molecule peaked, we confirmed that we detected almost no foci with fluorescence at 2X intensities in our highly diluted conditions (Figure S1P). Thus, single mRNAs can be distinguished from clusters containing two mRNAs whose intensity is expected at 2X, validating that we can quantify mRNA clustering with single molecule sensitivity. In addition we further confirmed that at high dilution, the fluorescence intensity distributions of single molecules overlapped whether they were recorded inside GFP:CAR-1 P-bodies (condensed phase), or outside in the cytosol (dispersed phase) (Figure S1Q). This, in combination with further controls detailed below (Section of Single molecule fluorescence intensity controls) confirms that single molecule fluorescent intensities do not significantly change between the condensed and soluble phases.

mRNAs copies within sub-diffractive foci

While in diluted conditions, all mRNA foci have an almost identical fluorescence intensity distribution which corresponds to the intensity of single mRNAs, at higher mRNA concentrations many brighter foci corresponding to mRNA clusters containing multiple mRNAs were detected (Figure S1P). The modeled KDE of single molecule amplitudes (Figure S1P) was then used to estimate the number of single mRNA foci detected in oocyte cytosols (Figure S1S). To this end, the distribution of fluorescent amplitudes of cytosolic mRNA foci was fit with a right-skewed Gaussian model. This fit was further decomposed in two Gaussian distributions. The peak of the first Gaussian was imposed to be centered at the single molecule fluorescence amplitude whose parameters were calibrated at lower concentration in Figure S1P as described above. The second Gaussian centered at higher fluorescence amplitudes, and described foci containing more than one mRNA molecule (Figure S1S). This second population of foci were considered as nanoclusters. The right-skewed Gaussian function used to describe fluorescence intensity distribution was the following:

$$\hat{A}_f(x) = h_s * \phi(x)\Phi(\alpha x) + h_n * \phi_n(x)\Phi_n(\alpha_n x)$$

where $\hat{A}_f$ denotes the KDE for the amplitude of cytosolic mRNA foci. The fitting yields estimates of the height (h_s) for the single molecule fraction with fixed parameters given by $\phi(x)\Phi(\alpha x)$, as well as estimates of h_n, α_n, $centroid_n$ and sd_n, for the nanocluster fraction. To estimate the number of molecules, the functions that describe the KDEs of single molecule ($h_s * \phi(x)\Phi(\alpha x)$) and nanoclusters ($h_n * \phi_n(x)\Phi_n(\alpha_n x)$) populations were integrated, multiplied by the number of cytosolic foci, and divided by the estimated peak amplitude given by $\hat{A}$. This integration allowed

us to estimate the proportion of single mRNAs and nanoclusters, and the number of molecules in each fraction.

mRNAs copy number quantification within macro-condensates

To quantify the number of mRNA molecules that were clustered within macro-condensates, we took advantage of the average PSF of single mRNAs computed at low concentration (see above and Figure S1R) and used two complementary and cross-validating methods, an integrative method and a cumulative method (Figure S1R). For the integrated intensity approach, we used the dedicated FISH-quant biocomputing pipeline[57] that we modified to adapt integration windows to each condensate volume. For the cumulative method, we computed the number of mRNA molecules per condensates as follows:

$$N_{(cumulative\ intenisty)} = \frac{\sum_{j=1}^{V_{mc}} (I_{mc_j} - BGD_{sm}) \geq 0}{\sum_{i=1}^{V_{sm}} (I_{sm_i} - BGD_{sm}) \geq 0},$$

where V represents the number of voxels, mc a given macro-condensate, sm the average PSF of single mRNAs, I is the grayscale intensity, and BGD denotes background.

Quantifications of mRNA phase parameters

Dispersed mRNA copy number or dissolved mRNAs ($N_{dis(smFISH)}$):

Sum of the mRNAs that are detected as single transcripts in the cytosolic phase as described in our smFISH quantification pipeline detailed above.

Condensed mRNA copy number or clustered mRNAs ($N_{cond(smFISH)}$)*:*

Sum of the mRNAs that are detected either as belonging to macro-condensates or nanoclusters in our smFISH quantification pipeline detailed above.

Total mRNA copy number ($N_{tot(smFISH)}$):

Sum of dispersed and condensed mRNA copy numbers.

Condensed mRNA fraction ($\%\ cond_{smFISH}$):

Ratio between the condensed mRNA copy number and the total mRNA copy number; $\%\ cond_{smFISH} = \frac{N_{cond(smFISH)}}{N_{tot(smFISH)}} * 100.$

P-body enrichment (FC_{smFISH})*:*

Ratio between the condensed mRNA copy number and the dispersed mRNA copy number; $FC_{smFISH} = \frac{N_{cond(smFISH)}}{N_{dis(smFISH)}}$.

Phase volumes:

The segmentation of oocyte boundaries and oocyte staging (see above) was used to obtain 3D reconstructions of staged oocytes and nuclei, and measure respective volumes. The

segmentation of mRNA condensates using a thresholding approach (see above) yielded macro-condensate volumes.

Total cytoplasmic concentration ($C_{tot(smFISH)}$):
Total copy number divided by the cytoplasm volume where the cytoplasm volume ($vol_{cytoplasm}$) was defined as the oocyte volume without the nucleus; $C_{tot(smFISH)} = \frac{N_{tot(smFISH)}}{vol_{cytoplasm}}$.

Dispersed phase cytosolic concentration ($C_{dis(smFISH)}$):
Concentration of mRNAs that are present as single transcript (non-clustered) in the dispersed phase. The dispersed mRNA copy number was divided by the cytosol volume ($vol_{cytosol}$) , defined as the oocyte volume to which the volume of macro-condensates and the nucleus was subtracted; $C_{dis(smFISH)} = \frac{N_{dis(smFISH)}}{vol_{cytosol}}$.

Condensed phase concentration ($C_{cond(smFISH)}$):
Condensed mRNA concentrations were measured in macro-condensates larger than 19 µm^3 as, $\frac{mRNAs\ in\ macro-condensate}{vol_{macro-condensate}}$, because volume measurements are more accurate in larger objects. $C_{cond(smFISH)}$ is the average condensed mRNA concentrations.

Partition coefficient (PC_{smFISH}):
The partition coefficient was computed as the ratio between the condensed phase concentration and the dispersed phase cytosolic concentration; $PC_{smFISH} = \frac{C_{cond(smFISH)}}{C_{dis(smFISH)}}$.

Condensate cumulative volume ($\sum vol_{cond}$)*:*
The condensate cumulative volume could not be directly measured because the smallest condensates are below microscopy resolution. Instead we computed the condensate cumulative volumes as follow*:* $\sum vol_{cond} = \frac{N_{cond(smFISH)}}{C_{cond\ (smFISH)}}$.

spn-4 mRNA distribution across cluster sizes:
The cluster sizes were defined as the number of condensed mRNA copies per cluster (mRNA molecules per foci, see quantification of the number of mRNAs copies within sub-diffractive mRNA foci and macro-condensates sections). Second to compute *spn-4* mRNA distributions across cluster sizes, the number of clusters was multiplied by the number of *spn-4* molecules per cluster.

Theoretical relationship between the Partition coefficient (PC) *and the Condensed mRNA fraction* ($\%\ cond$, CF):
By combining:

(a) $CF = \frac{N_{cond}}{N_{tot}} = \frac{N_{cond}}{N_{dis}+N_{cond}}$

(b) $C_{cond} = \frac{N_{cond}}{V_{cond}}$

(c) $C_{dis} = \frac{N_{dis}}{V_{dis}}$

(d) $PC = \frac{C_{cond}}{C_{dis}} = \frac{N_{cond}}{N_{dis}} * \frac{V_{dis}}{V_{cond}}$

(e) $\frac{N_{dis}}{N_{cond}} = \frac{1}{PC} * \frac{V_{dis}}{V_{cond}}$

We obtained the following theoretical relationship:

$$PC = \frac{CF}{1 - CF} * \frac{V_{dis}}{V_{cond}}$$

$$PC = \frac{\%\ cond}{100 - \%\ cond} * \frac{V_{dis}}{V_{cond}}$$

where V_{dis} is the cytosol volume (see *phase volumes*) and V_{cond} is the *condensate cumulative volume* (Figures S2D).

In silico simulations for smFISH

We used simulated images to evaluate the accuracy of our smFISH measures of mRNA clustering (Figure S4). In the absence of physical interactions, two independently free diffusing molecules may artificially appear as belonging to the same cluster by lack of spatial resolution in microscopy images as the molecules randomly come close to each other. Such an occurrence will increase at high concentrations, leading to cluster overestimates. To take into account this resolution limit at high concentrations, and correct for potential clustering overestimates, we took an *in silico* simulation approach (Figure S4). To do this, we generated synthetic smFISH images where individual mRNAs were placed randomly within a 3D space, as expected from free diffusion without clustering (Figure S4A). To simulate our experimental imaging resolution limits, experimental PSFs of single mRNAs extracted from RNAi experiments were used. The random placement of PSFs in 3D was done in a segmented oocyte without nucleus using the MATLAB function *randsample.* A variable of our simulation was the input RNA concentration, that was artificially increased by adding randomly placed PSFs (Figure S4A). For the random placement, sampling replacement was allowed, and simulations were repeated 3 times for a given RNA concentration. The simulated images were next analyzed using our smFISH quantification pipeline (Figure S1, and see above). In this way, we could compare the measured smFISH mRNA quantification results from the simulated images that did not include clustering in the input parameters (1) to the actual input values of the simulation, (2) to our experimental measures (Figures S4B-S4F). The experimental nanocluster quantifications were corrected by subtracting the cluster artifactual over detection in the simulation, and single soluble mRNA quantifications were corrected by adding mRNA artifactually detected as nanoclusters (Figures S4B-S4F).

Single molecule fluorescence intensity controls

First, we confirmed that single molecule fluorescence intensities distributions were independent of RNA condensation (Figure S1Q, and above section "*Single molecule calibration*"). To test whether our quantifications of clustered mRNAs in the condensed phase were accurate and scaled linearly with the quantification of single mRNAs in the dispersed phase, we induced a

dissolution of mRNA clusters, and tested whether our total mRNA quantification remained unchanged independent of mRNA condensation status. For that purpose, condensate dissolution was either artificially induced by RNAi (Figures 4D, S6D), or physiologically induced during oocyte maturation (Figures 6E-6F''). Both approaches quantified the same total mRNA copy number whether mRNAs were condensed in macro-condensates, in nanoclusters or dissolved, confirming our quantifications did not over or underestimate mRNA in the condensed form as compared to the dispersed form. In addition, the smFISH computed mRNA copy number, as well as mRNA enrichment in condensates, linearly correlated with the results independently obtained from the condensate purification sequencing method (Figures S2J-S2L), cross-validating our imaging quantification by a biochemical purification sequencing approach.

P-body purification and oocyte dissection

Oocyte P-bodies were purified from *C. elegans* by adapting our published Fluorescent activating Particle Sorting (FAPS) method that we previously developed starting from human epithelial cells in culture,[3] the most significant improvement being our ability to start from whole animal fixed tissues rather than non-fixed cell lines.

Sample preparation

C. elegans oocyte P-bodies were labelled using a fluorescent GFP:CAR-1 reporter under the germline promoter *pie-1.*[10] As a secondary marker, PGL-1:RFP was used, which labels subcompartments of the oocyte P-bodies.[10,39] To sort oocyte P-bodies, ~ 1000 *C. elegans* animals were used per replicate. For each sorting experiment, staged L4 females (TE71) and L4 hermaphrodites (TE51) were isolated and grown for 72 h at 20°C in the absence of males. In adult worms, GFP:CAR-1 labelled P-bodies formed in the arrested oocytes of unmated females (TE71). By contrast, within active oocytes of self-mated hermaphrodites (TE51) that bypass oogenesis arrest, GFP:CAR-1 did not condensed into P-bodies macro-condensates, providing negative controls for the P-body purification.

Worm lysis and extract preparation for FAPS

Adult worms were collected and washed 3 times in Phosphate Buffer (77.4mM Na_2HPO_4; 4mM NaH_2PO_4) equilibrated at 20°C, fixed in ~2.2% formaldehyde in a Phosphate Buffer for 12 min at 20°C, and washed twice in 100mM Tris pH 7.5 to quench the formaldehyde. All subsequent steps were conducted at 4°C to limit RNA degradation. Fixed worms were washed twice in Lysis buffer (150 mM NaCl; 50 mM Hepes pH 7.5; 1mM EDTA; 1% Triton; 0,2% SDS), resuspended in 300uL of fresh lysis buffer complemented with 80U of RNaseOut (Invitrogen). Worm lysates were generated by mechanical bead beating using 1.0 mm zirconium-oxide beads in a Bullet Blender Gold homogenizer (Next Advance). The bead beating was conducted at medium speed for 15 s, which was repeated 8 times for total cellular lysis, with intermediate cooling steps of 30 s on ice between each bead beating to limit RNA degradation that can be induced by samples over-heating. The resulting fraction was named the whole animal pre-sorted extract. Three biological replicates from independent experiments were performed.

P-body sorting by FAPS

From the whole animal pre-sorted extracts, oocyte P-bodies were sorted on a cell sorter (MoFlo Astrios EQ, Beckman Coulter) equipped with a nozzle size of 70 mm, and working at 66 000 Hz

with a 60 psi pressure, using the 488 nm excitation laser and the 526/26 band pass filter to detect the GFP labelled P-bodies, and the 561 nm excitation laser and the 579/8 band pass filter to detect the RFP. Particles were detected according to their intensities (either GFP or RFP) and sizes (Forward Scattered Light). The sorting window was defined to keep GFP:CAR-1 labeled oocyte P-bodies, by comparing TE71 extracts that contained P-bodies to TE51 extracts that did not contain enlarged P-bodies (Figure 1D). The purity mode (1-2 envelopes) and a differential pressure of 0.5 were applied for sorting. Note that the starting dilution of the pre-sorted extract was critical for the purity of sorted P-bodies. A 1/2000 dilution of the pre-sorted extract was therefore adjusted to detect maximum 10000 Events Per Second (EPS). After 12 h of sorting, $1x10^6$ P-bodies were collected. The pre-sorted and sorted fractions were stored at 80 °C. The presence of sorted P-bodies was confirmed by microcopy, and their stability was verified by re-sorting collected P-bodies [3].

Oocyte dissections

For transcriptomic analyses, an additional control of dissected oocytes was included. Briefly, ~100 adult *C. elegans* females (TE71), that were matched to the synchronized *C. elegans* used for P-body purification, were washed in Phosphate Buffer and dissected on coverslips. Dissected oocytes were transferred into 1ml Phosphate Buffer, centrifuged at 1000G for 10 min, and resuspended in ~150 µl Phosphate Buffer. Lysis and FAPS steps were skipped. Three biological replicates from independent experiments were performed.

Transcriptome analysis of oocyte P-bodies

Sorted oocyte P-bodies, whole animals extracts (pre-sorted extracts containing somatic and germline RNAs), and dissected oocytes fractions (oocyte RNAs) were processed in parallel for RNA-sequencing (RNA-Seq).

RNA sequencing

In order to obtain high-quality RNAs from fixed samples (sorted oocyte P-bodies and animal extracts) and oocyte dissections, total RNA was extracted using a miRNeasy FFPE kit (Qiagen) with adaptations: i) the deparaffinization step was skipped, and ii) since sorted oocyte P-bodies were subcellular fractions, the separation of cell debris by centrifugation was omitted for these samples. The subsequent steps followed the recommendations of the supplier, and notably included DNase-I treatment and reverse crosslink of fixed fractions. After extraction, RNA integrity was confirmed using Agilent RNA Pico Chips (Agilent 2100 BioAnalyser), and RNA concentration was quantified with RNA HS Assay Kit (Invitrogen) using a Qubit 4.0. For cDNA libraries preparation, 10 ng of total RNA were used. Briefly, paired-end RNA-Seq libraries with barcodes were generated using SMARTer Stranded Total RNA-Seq Kit v2 - Pico (Takara). The quality and average size of the libraries were confirmed with Agilent High Sensitivity DNA Chips (Agilent 2100 BioAnalyser), and the concentrations were measured with dsDNA HS Assay Kit (Invitrogen) using a Qubit 4.0. For RNA-Seq, libraries were pooled in equimolar concentrations of 4 nM and paired-end sequencing (Illumina TruSeq HT assay) was performed at UCAGenomix - Functional Genomics platform (Université Cote d'Azur, Nice, France).

RNA-Seq analysis

RNA-Seq libraries were built from 3 biological replicates of the sorted P-bodies, whole animal pre-sorted extracts, and dissected oocytes. After a 75 base pair long paired-end sequencing of pooled samples, demultiplexing (*bcl2fastq application*) was performed. Sequencing reads were checked for quality by FastQC (FastQC: A Quality Control Tool for High Throughput Sequence Data, *https://qubeshub.org/resources/fastqc*) and 4 bases of the 5'-end, and 1 base of the 3'-end were trimmed. Read mapping was then performed on a local Galaxy server.[66] Briefly, reads were aligned to the *C. elegans* genome (WBcel235.96) using *HISAT2 v2.1.0.*[67] For the alignment, the following stranded reverse-forward design parameters were used: function governing the maximum number of ambiguous characters was allowed, maximum mismatch penalty = 6, minimum mismatch penalty = 2, maximum soft clipping penalty = 2, minimum soft clipping penalty = 1, ambiguous read penalty = 1, read gap open penalty = 5, read gap extend penalty = 3, reference gap open penalty = 5, reference gap extend penalty = 3, penalty for canonical splice sites = 0, penalty for non-canonical splice sites = 12, minimum intron length = 20, maximum intron length = 140000. To estimate relative RNA abundance for each transcript species, FPKM (Fragments Per Kilobase Million) and TPM (Transcripts Per Kilobase Million) were computed with *StringTie* using default parameters.[68]

RNA enrichment in oocyte P-bodies

To compute the relative RNA enrichment between FAPS purified P-bodies, whole animal pre-sorting extracts, and whole oocytes, read raw counts were determined for each annotated gene by *HTseq-count* using default stranded parameters.[69] Next, the *DESeq2* Bioconductor package was used to detect fold-change ($FC_{RNA-Seq}$) differences between groups taking into account internal normalization with correction for library size and RNA composition bias.[74] The geometric mean was calculated for each gene across samples. Then, the counts per gene were divided by the geometric mean. The ratios generated by this procedure were the size factors for each sample. Shrinkage estimation was applied for dispersions using the samples from the different conditions as replicates. To determine gene expression differences between conditions, negative binomial generalized linear models were fit to each gene and the Wald test was applied for significance testing. Count outliers and genes with mean of normalized counts below threshold were removed by Cook's distance. For statistical significance, *p*-value < 0.05 was considered the threshold of FDR filtering for Type II error. All the statistical analyses were conducted in R version 4.1.2.

Feature analysis of oocyte P-body mRNAs

Differential enrichment of RNA biotypes in oocyte P-bodies, including rRNAs.

GenomicRanges and rtracklayer Bioconductor packages were used to retrieve biotype information from the Gene Transfer Format file corresponding to WBcel235.96.[75,76] Transcripts were classified into the following biotypes: mRNA, pseudogenes, antisense, lincRNA, snRNA, ncRNA, rRNA, snoRNA, tRNA, and the $FC_{RNA-Seq}$were computed for each biotype by comparing the oocyte P-body transcriptome to the whole oocyte transcriptome (Data S1).

Differential enrichment of mRNAs in oocyte P-bodies depending on the abundance of their protein product.

mRNAs were binned in 3 classes (no, poor and high protein product) according to the abundance of the encoded proteins in diakinesis oocytes as estimated using GFP fluorescent reporters.[46]

Differential P-body enrichment for the RNA targets of various RNA binding proteins.
The mRNA targets of various RNA binding proteins were predicted as follow. The top 100 mRNA targets of FBF-1 and GLD-1 were ranked according to their binding site records from CLIP data sets as computed in.[58] The targets of OMA-1 and LIN-41 were identified in [50] and selected with a corrected p-value bellow 0.05. mRNA targets of PUF-5 were predicted from.[49]

Gene Ontology (GO) analysis.
To determine the GO terms of our P-body enriched and depleted mRNAs, a Panther enrichment test (release 20191216) was conducted at http://www.pantherdb.org/, using the GO Ontology database DOI: 10.5281/zenodo.3727280 Released 2020-03-23. Representative categories are shown in Figure 2E, and complete analysis can be found in Data S4.

Nucleotide length for mRNAs enriched in oocyte P-bodies and embryonic P-granules.
For P-body and P-granule enriched mRNAs (corrected p-value p<0.05), we computed for the longest isoform of each coding transcript the 5'UTR, 3'UTR, and CDS nucleotide length using the *C. elegans* genome annotation (WBcel235.96). P-granule enriched mRNAs were identified in [13].

Nucleotide compositional bias of mRNAs enriched in oocyte P-bodies.
mRNAs were ranked from low to high enrichment in P-bodies ($FC_{RNA-Seq}$) and distributed in 5 equal sizes bins. For each bin, the nucleotide composition (% of A,U,C,G) was computed in the 5'UTR, 3'UTR, and CDS.

Transcriptome-wide scaling of condensation
For each transcript of the transcriptome, the condensed mRNA copy number in the cytosolic P-bodies ($N_{cond(p)}$), the dissolved mRNA copy number in the dispersed cytosolic phase ($N_{dis(e)}$), and their P-body enrichment as compared to the dispersed cytosolic phase (FC_p) were extrapolated by calibrating the RNA condensate purification and sequencing results with smFISH imaging quantifications of RNA condensation (Figure S2A-L). The RNA-Seq provided information about mRNA abundance (FPKM units) and enrichment ($FC_{RNA-Seq}$) on a transcriptome-wide scale, but values were relative (Figures S2F-S2I). In a complementary approach, the smFISH quantified mRNA absolute copy number in the condensed ($N_{cond(smFISH)}$) and dispersed phases ($N_{dis(smFISH)}$) and their exact enrichment in P-bodies (FC_{smFISH}), but for a limited number of candidate mRNAs (Figure S1, S2A-E). To combine the advantages of these two approaches, we scaled the transcriptome-wide RNA-Seq with the absolute mRNA measurements of the smFISH imaging using linear regressions (Figures S2J-S2L).

Linear regressions demonstrated the strong correlation and therefore cross-validation between the two approaches when comparing:

(i) mRNA enrichment in P-bodies measured by smFISH ($\log_2 FC_{smFISH}$) vs. mRNA enrichment in P-bodies measured by RNA-Seq ($\log_2 FC_{RNA-Seq}$) (Figure S2J).
(ii.a) smFISH condensed mRNA copy number ($N_{cond(smFISH)}$) vs. RNA-Seq abundance in condensates (FPKM units) (Figure S2K).

(ii.b) smFISH total mRNA copy number in oocytes ($N_{tot(smFISH)}$) vs. RNA-Seq abundance in oocytes (FPKM units) (Figure S2L).
Note that $N_{tot(smFISH)} = N_{dis(smFISH)} + N_{cond(smFISH)}$, and the linear regressions of absolute counts (ii.a and ii.b) were constrained to intercept the origin (Figures S2K, S2L).

We took advantage of these linear regressions whose confidence interval were narrow to predict (p) the $\log_2 FC_p$ (regression i) and the condensed mRNA counts ($N_{cond(p)}$) (regression ii.a) for ~11140 mRNA species (Data S3), as follows.

The linear regression (i) of the mRNA enrichment in P-bodies yielded smFISH calibrated predictions (p) for the FC_p:

$\log_2 FC_p \approx \log_2 \frac{condensed}{dissolved}$, and therefore $FC_p \approx 2^{\log_2 FC_p} \approx \frac{condensed}{dissolved}$

$FC_p \approx \frac{condensed}{dissolved}$ yielded estimates (e) for the percentage of condensed molecules (% $cond_e$) and the percentage of dissolved molecules (% dis_e) as follows:

$$\% \, cond_e = \frac{FC_p}{FC_p+1} * 100, \; \% \, dis_e = \frac{1}{FC_p+1} * 100$$

The linear regression (ii.a) of P-body mRNA abundances predicted condensed mRNA counts ($N_{cond(p)}$), which combined with FC_p returned estimates for the dissolved counts as $N_{dis(e)} = \frac{N_{cond(p)}}{FC_p}$, and total counts as $N_{tot(e)} = N_{cond(p)} * \left(\frac{FC_p+1}{FC_p}\right)$.

Linear regressions, model predictions, and statistical analyses were conducted using R version 4.1.2.

Transcriptome-wide percentage of condensation

To obtain an estimate of the condensation percentage for all mRNAs combined together while minimizing the fitting dependence, we computed a weighted average of the relative $\log_2 FC_{RNA-Seq}$ enrichments ($\overline{\log_2 FC}_w$) calculated using the RNA-Seq of dissected oocytes, and in which the weight of each transcript depends on its relative copy number (FPKM) within the oocyte as follows:

$$\overline{\log_2 FC}_w = \frac{\sum_{n=1}^{N} \log_2 FC_n * oocyte\ FPKM_n}{\sum_{n=1}^{N} oocyte\ FPKM_n}$$

Where n represents a transcript and N is the total number of transcripts in dissected oocytes.
Next, we used the model (i) to obtain the $\log_2 FC_p$ enrichment calibrated by smFISH, and calculated the estimated percentage of condensation (% $cond_e$) and the confidence interval for all oocyte mRNA transcripts (Figure S7A).

Transcriptome-wide compaction in condensates

To estimate the mRNA compaction in P-body condensates, we computed the transcriptome-wide condensed mRNA local concentration within P-bodies as follow:

$$transcriptome\text{-}wide\ C_{cond} = \frac{\sum N_{cond(p)}}{\sum vol_{cond}}$$

Confidence interval was computed as follows:

$$\min(transcriptome\text{-}wide\ C_{cond}) = \frac{\sum N_{cond(p)}\ \ lower\ limit\ (95\%\ CI)}{\sum vol_{cond}\ \ uper\ limit\ (95\%\ CI)}$$

$$\max(transcriptome\text{-}wide\ C_{cond}) = \frac{\sum N_{cond(p)}\ \ uper\ limit\ (95\%\ CI)}{\sum vol_{cond}\ \ lower\ limit\ (95\%\ CI)}$$

The P-body mRNA condensed copy number ($N_{cond(p)}$) and its minimum and maximum 95 % confidence interval (95% CI) were computed for each transcript transcriptome-wide using the linear regression (ii.a) (Data S3), from which the cumulative condensed copy number was computed for all oocyte mRNAs ($\sum N_{cond(p)}$) and its upper and lower limits. The corresponding cumulative volume of P-bodies ($\sum vol_{cond}$) was computed as described in the smFISH method section.

We further calculated the mRNA compaction in condensates in nucleotide per µm^3 ($mRNA\ nt\ concentration$) (Figures 7B-C, S7A-E), as follows, where nt is the annotated length in nucleotides of each corresponding full-length transcript (Data S3):

$$mRNA\ nt\ concentration = \frac{\sum N_{cond(p)} * nt}{\sum vol_{cond}}$$

Quantification of coarsening across oogenesis

The proximo-distal axis in *C. elegans* gonads, along which oocytes are aligned in a single row, is a convenient spatiotemporal axis, to study condensate growth across time. For each oocyte the time before ovulation can be estimated knowing the oocyte position in the row and the ovulation rate (the frequency at which one oocyte move from one position to the next) (Figure 3A-C). To quantify P-body coarsening, we recorded the sizes of fluorescently labelled GFP:CAR-1 P-bodies depending on oocyte position along the gonad axis. To image the entire gonads, up to 4 z-stack acquisitions were analyzed per animal, using the parameters described in the live-imaging methods section. Next, condensates were segmented within staged oocytes using the script detailed in the smFISH quantification methods (Figure S1). We computed the condensate volume distribution and the cumulative volume distribution for each time-point before ovulation (oocyte position) (Figure 3C').

mRNA compositional bias across cluster sizes

The repressed mRNAs *spn-4* and *glp-1* were simultaneously detected by two-color smFISH using Cy3 and Cy5 labeled probes. Images were acquired as described in the smFISH imaging section with an additional channel for Cy5 (633 nm laser, BP 570-620 + LP 645). Laser power used for

both channels was 5% (Fast Airyscan). Single-labeled controls showed no bleed-through between Cy3 and Cy5 channels (Figure S5A-H).

To assess mRNA compositional differences across cluster sizes, *the ratio between glp-1* and *spn4* mRNA cumulative fluorescence intensities was computed for each mRNA cluster and plotted as a function of the cluster size. Clusters were segmented using the thresholding approach described in Segmentation of mRNA condensates. The stringency of the thresholding was slightly reduced to include small clusters.

mRNA demixing within macro-condensates

The degree of *spn-4* and *glp-1* demixing within macro-condensates was evaluated by computing the Pearson correlation coefficient (*r*) along x-y transversal sections of macro-condensates (Figure 3E'''). As positive control of mixing, *spn-4* or *glp-1* simultaneously with Cy3 and Cy5 fluorescent probes (see Figures 3E''', S5J). In addition, the ratio between Cy3 and Cy5 cumulative fluorescence intensities was plotted as a function of cluster size, which confirmed the homotypic feature of small clusters as compared to large macro-condensates (Figures S5J, K).

Analysis of relative protein concentrations

Protein concentrations across differentiation

The relative GFP:CAR-1 and PUF-5:GFP protein concentrations were calculated along oocyte differentiation using z-stack confocal images of live *C. elegans* gonads (see Live imaging section). Oocytes were manually delimited and staged according to their differentiation along the gonad proximo-distal axis, and GFP condensates were segmented (see Quantification of P-body coarsening across oogenesis). The relative concentration in oocytes (rC_{oocyte}), dissolved (rC_{dis}), condensed (rC_{cond}), and in each macro-condensate (rC_{MC}) was computed per volume unit as follows:

$$rC_{phase} = \frac{\sum FU}{phase\ volume}$$

Where FU is the fluorescence intensity units and $phase\ volume$ is the volume given in either voxels or μm^3. RNAi controls depleting the fluorescent protein of interest were used to confirm the specificity and sensitivity of our measures (Figures S6A-S6B').

To measure GFP:CAR-1 local concentrations (Figure 4B) in condensates across oocyte differentiation, values were obtained from the eight larger condensates segmented in each oocyte; in the same fashion as the condensed phase concentration (see $C_{cond(smFISH)}$) of mRNAs was computed.

fog-1 and spn-4 translation reporters

The *P*$_{pie-1}$*::GFP::H2B::3'UTR*$^{fog-1/spn-4}$ fusions reporters were reported to recapitulate endogenous expression patterns.[46] The accumulation of the GFP:H2B reporter in nuclei was quantified in one focal plane by computing the maximum intensity of a selected nucleus minus the background of the surrounding cytosol, as previously reported.[6,39]

SPN-4:GFP protein production rates

SPN-4:GFP protein production rates, computed in Fluorescence units per µm^3 per min, were derived from SPN-4:GFP concentrations (in Fluorescence units per µm^3) across oogenesis time points (in min). Briefly, synchronized unmated L4 larvae females were either isolated or kept in culture with males, to compare protein production rates in quiescent (unfertilized) and active oogenesis (fertilized). Time points between N and N+1 oocytes in the gonad correspond to the time between 2 ovulation events, and are 0,33 h and 10 h, in active and quiescent oogenesis, respectively. *C. elegans* gonads from adults that were 48 h post L4 larvae stage were imaged and the relative SPN-4:GFP concentration (rC_{SPN4}) was calculated at each oogenesis time point along the gonad using Fiji. For image background subtraction, a representative region (~250 x 250 pixels) was defined in the distal gonad that does not express SPN-4:GFP. The rC_{SPN4} per segmented and staged oocyte was computed from cumulative z-projections (sum of slices) of 3D z-stacks as follows:

$$rC_{sPN4} = \frac{\bar{I}_{outline} * px_{outline} - BGD * vx_{oocyte}}{V_{vx} * vx_{oocyte}} = \frac{\sum I_{oocyte-BGD}}{V_{oocyte}}$$

$\bar{I}_{outline}$ represents the mean fluorescence intensity of the z-projected oocyte ($outline$), $px_{outline}$ is the number of pixels in the $outline$, vx_{oocyte} is the number of voxels in the oocyte given by $N_{stacks} * px_{outline}$ where N_{stacks} is the number of slices. V_{vx} represents the voxel volume in µm^3. The estimated mean background was calculated as $BGD = \frac{\bar{I}_{BGD} * px_{BGD}}{vx_{BGD}} = \frac{\bar{I}_{BGD}}{N_{stacks}}$, where $\bar{I}_{BGD}$ is the mean fluorescence intensity of the z-projected BGD representative region ($outline_{BGD}$), px_{BGD} is the number of pixels in the $outline_{BGD}$, and vx_{BGD} is the number of voxels given by $N_{stacks} * px_{BGD}$.

From the difference in relative SPN-4:GFP concentration ($\Delta\, rC_{SPN4}$) between the N and N+1 oocyte separated by the ovulation time, we computed the relative SPN-4 protein production rates ($rPR_{SPN4} = \frac{\Delta\, rC_{SPN4}}{ovulation\ time}$).

QUANTIFICATION AND STATISTICAL ANALYSIS

Quantification

The details of the quantification are included in the sections of method details.

Statistical analysis

Statistical analyses were performed in R v. 4.1.2. When comparing two datasets, normality distribution was assessed using a Shapiro-Wilk test. Two-sided Mann–Whitney U-test was used for non-normally distributed data, and two-sided t-test for normally distributed (parametric) data. For parametric hypothesis testing, equality of variances was determined (F test; *var.test* function). When comparing more than two datasets, regression models were fitted and model assumptions checked including the normality of residuals (Shapiro-Wilk test). One-way ANOVA was used if a model met assumptions, otherwise, Kruskal-Wallis tests were implemented. Parametric or non-

parametric pairwise comparisons were conducted with a false discovery rate (FDR) adjustment method. *p*-value less than 0.05 was considered statistically significant.

Plotted data are presented as mean values with 95% confidence intervals, violin plots with the probability density distribution of the data, or boxplots with median (center line), first and third quartiles (box bounds), whiskers (1.5 times the interquartile range), and outliers. Sample sizes (*n*) are indicated in figure captions or the relevant sections of method details.

The details of RNA-Seq statistical analyses are included in the corresponding sections of method details.

SUPPLEMENTARY TABLES

Protein abundance	Gene id (wormbase)	mRNA	Enrichment in P-bodies
High	WBGene00001482	*fog-2*	-1.580621583
High	WBGene00003220	*mes-2*	-0.3786363
High	WBGene00003920	*par-5*	-1.16238
High	WBGene00006537	*tbb-2*	-1.272879
High	WBGene00003994	*pgl-3*	-0.7272095
High	WBGene00003043	*lip-1*	1.009881
High	WBGene00004374	*rme-2*	-0.799679
High	WBGene00003230	*mex-5*	1.076572
High	WBGene00004241	*puf-5*	0.1067736
High	WBGene00003912	*pal-1*	1.182124
High	WBGene00000871	*cye-1*	-0.436435661
High	WBGene00003221	*mes-3*	0.3024479
High	WBGene00000467	*cep-1*	0.431863468
High	WBGene00004976	*spe-41*	-0.02561671
High	WBGene00004027	*pie-1*	-0.3722637
Poor	WBGene00003992	*pgl-1*	0.1226306
Poor	WBGene00003785	*nos-3*	0.956317
Poor	WBGene00000935	*daz-1*	1.093645633
Poor	WBGene00001862	*him-3*	1.293189
Poor	WBGene00003229	*mex-3*	0.5136953
Poor	WBGene00001481	*fog-1*	1.471059837
No	WBGene00001609	*glp-1*	1.270785647
No	WBGene00001401	*fbf-1*	1.05501891
No	WBGene00001402	*fbf-2*	0.941915491
No	WBGene00001595	*gld-1*	0.98989342
No	WBGene00004984	*spn-4*	1.849331
No	WBGene00004078	*pos-1*	1.533989

Table S1. mRNA enrichment within oocyte P-bodies according to the abundance of their protein product in oocytes, related to Figure 2.

Strain	Genotype	Mutagen	Reference
-	*P_{pie-1}::gfp::car-1::UTR^{pie-1}*	Bombardment	[59]
-	*fog-2(q71)*; *P_{pie-1}::gfp::car-1::UTR^{pie-1}*	Bombardment	This study
TE73	*fog-2(q71)*; *car-1(oc8[car-1:gfp:FLAG])*	CRISPR-Cas9	gift of T. Evans
TE51	*P_{pie-1}::gfp::car-1::UTR^{pie-1};P_{nmy-2}::pgl-1::mrfp*	Bombardment	[10]
TE71	*fog-2(q71)*; *P_{pie-1}::gfp::car-1::UTR^{pie-1};P_{nmy-2}::pgl-1::mrfp*	Bombardment	[10]
DG4158	*spn-4(tn1699[spn-4::gfp::3xflag])*	CRISPR-Cas9	[50]
-	*fog-2(q71)*; *spn-4(tn1699[spn-4::gfp::3xflag])*	CRISPR-Cas9	This study
DG4215	*puf-5(tn1726[gfp::3xflag::puf-5])*	CRISPR-Cas9	[50]
-	*fog-2(q71)*; *puf-5(tn1726[gfp::3xflag::puf-5])*	CRISPR-Cas9	This study

P: promoter. *UTR*: 3' untranslated region.

Table S2. *C. elegans* strains.

mRNA	Probe	5' - probe - FLAPx - 3'
spn-4	1	ATGGCGAAGCACTTCATTTGACTTCGAGCCCTCCTAAGTTTCGAGCTGGACTCAGTG
spn-4	2	CATTGCTACGGTATGGTGCCATCATGAATCCTCCTAAGTTTCGAGCTGGACTCAGTG
spn-4	3	TTGAACAACTGATGCATTGGCTCAGCTCCCTCCTAAGTTTCGAGCTGGACTCAGTG
spn-4	4	GGGCTGTTATGTGGGGACCAATGAATCTCCCTCCTAAGTTTCGAGCTGGACTCAGTG
spn-4	5	TGCTCTCTTTCCTTTGTTAGCACTATTATTTCCCTCCTAAGTTTCGAGCTGGACTCAGTG
spn-4	6	TGCTGCATGGTGAGTTTTGTCTGTGCATGCCTCCTAAGTTTCGAGCTGGACTCAGTG
spn-4	7	CATCAGAATACTTGTTTCCGTCGTAGGCTCGCCTCCTAAGTTTCGAGCTGGACTCAGTG
spn-4	8	CTCGCTGTGCTTGGTGCATCGAGGTGCCTCCTAAGTTTCGAGCTGGACTCAGTG
spn-4	9	GTTGATAAGCTTTCTGCGGGTTGGTGTCGCCCTCCTAAGTTTCGAGCTGGACTCAGTG
spn-4	10	TTCTCACTTCTATAATTCTTCCTTGAACATGTCCTCCTAAGTTTCGAGCTGGACTCAGTG
spn-4	11	TTCGTGAAGCGCAGCACGAGCTTTCTCCCTCCTAAGTTTCGAGCTGGACTCAGTG
spn-4	12	ACCCTTTGGATCCACGATCATTTGTGACGCCTCCTAAGTTTCGAGCTGGACTCAGTG
spn-4	13	AGAAGCCGGCTCACGAGTTTTCGGTTTGACCCTCCTAAGTTTCGAGCTGGACTCAGTG
spn-4	14	AATTGGATCTTTGTTGGAAGGATTCGCACTGTCCTCCTAAGTTTCGAGCTGGACTCAGTG
spn-4	15	TGTTAGCAAGCGAGGTAGGTTAAACGGACTGGCCTCCTAAGTTTCGAGCTGGACTCAGTG
spn-4	16	ACGAATCATTTGACAAGGACAACGAGTGTCGCCCTCCTAAGTTTCGAGCTGGACTCAGTG
spn-4	17	AAATGGGCGTATCAGTTGAACTGATTACTGGCCCTCCTAAGTTTCGAGCTGGACTCAGTG
spn-4	18	TTGGTGGAGAAACAGACTTTCCGTGGAACGATCCTCCTAAGTTTCGAGCTGGACTCAGTG
spn-4	19	GGAACCTTCGTAGAGAGCAGCGAGAAGATAATCCTCCTAAGTTTCGAGCTGGACTCAGTG
spn-4	20	CTGATGATCTCAATCCAGAAGATGTCACAGATCCTCCTAAGTTTCGAGCTGGACTCAGTG
spn-4	21	GAAGTGTCGAGAAGAGCAGTAATCTGGTCACGCCTCCTAAGTTTCGAGCTGGACTCAGTG
spn-4	22	ATGATGTGGGAATATAGAGTTCAACTCCACATCCTCCTAAGTTTCGAGCTGGACTCAGTG
spn-4	23	AACGGTAATCCATCATGTGCTCTGTGAGCCCTCCTAAGTTTCGAGCTGGACTCAGTG
spn-4	24	TTCCACACTCAGGACTCTTCCATATGCCCTCCTAAGTTTCGAGCTGGACTCAGTG
spn-4	25	GACAGCTCGTGATTCGAAGAATCAGAACACTTCCTCCTAAGTTTCGAGCTGGACTCAGTG
spn-4	26	TTTGCAGAAGTATTCACCAGCTGAAGAAAGCTCCTCCTAAGTTTCGAGCTGGACTCAGTG
spn-4	27	AGCTTCGGGAAAACATGTTGTGTTCTCCTTTTCCTCCTAAGTTTCGAGCTGGACTCAGTG
spn-4	28	CATAAATTATGAGGGGCTCGAAGATCGACACACCTCCTAAGTTTCGAGCTGGACTCAGTG
spn-4	29	GCTTTGGTGGTGGCAAAACTTCATTTTGTGGACCTCCTAAGTTTCGAGCTGGACTCAGTG
spn-4	30	AGGATTCGATGGAATCGAGTGTGACAAACCCCCTCCTAAGTTTCGAGCTGGACTCAGTG
spn-4	31	AGAACATTGCCGCCAAATCTTGTTCACGAAACCTCCTAAGTTTCGAGCTGGACTCAGTG
spn-4	32	AGGGAATATTGCTGACATATATCCTGTTATCTCCTCCTAAGTTTCGAGCTGGACTCAGTG
spn-4	33	ACAGGAATGCAAAAATAACTGGCGAACACAGCCCTCCTAAGTTTCGAGCTGGACTCAGTG
spn-4	34	AAGATGCTCAGAAAATACAATACGTGGGCACACCTCCTAAGTTTCGAGCTGGACTCAGTG
spn-4	35	GAGATGGCAAAATAGGGAAGATGCTGAAACGCCCTCCTAAGTTTCGAGCTGGACTCAGTG
spn-4	36	TCCTACAAAATAACACCGGGGGGGTCGATCCTCCTAAGTTTCGAGCTGGACTCAGTG
spn-4	37	TTGGTCTGCACAAGACTACGCGTGTTGAAAATCCTCCTAAGTTTCGAGCTGGACTCAGTG

Table S3. Sequence of probes against *spn-4*. Primary probes carried the FLAPx extension shown in blue.

mRNA	Probe	5' - probe - FLAPx - 3'
glp-1	1	TGACCGGTGGTGCCATTTCATGGTTAAACACCTCCTAAGTTTCGAGCTGGACTCAGTG
glp-1	2	CCCAGACTTAGCACCATGACCTGACTCCTCCTAAGTTTCGAGCTGGACTCAGTG
glp-1	3	AAGTTCATGATGGTAGCTGGCTTCAGCAACCCTCCTAAGTTTCGAGCTGGACTCAGTG
glp-1	4	GAGCAGCAGTCATGTCCATTGAATCGACTCCTCCTAAGTTTCGAGCTGGACTCAGTG
glp-1	5	CTCCTTTTGAAAGAAGAAGCTCTGCCATCTCCTCCTAAGTTTCGAGCTGGACTCAGTG
glp-1	6	ATCAATGCAGTCATACCATTCCGGTCCCCTCCTAAGTTTCGAGCTGGACTCAGTG
glp-1	7	CATTCACATCGGCTCCAGCCTTCAAGCCTCCTAAGTTTCGAGCTGGACTCAGTG
glp-1	8	TTTTCCTCTGACATTGGCAGCAAGCCACCTCCTAAGTTTCGAGCTGGACTCAGTG
glp-1	9	GCAGAACTCGTCGTCTATACTTTGAATCCACCTCCTAAGTTTCGAGCTGGACTCAGTG
glp-1	10	AATGATTTGACTGATTCCGACGACCTTTCTCCCTCCTAAGTTTCGAGCTGGACTCAGTG
glp-1	11	ACAGCTACCATTGCTTCCGTAATTGGGAGCCTCCTAAGTTTCGAGCTGGACTCAGTG
glp-1	12	ATACGTACGGTTGCTCGAAGATTTGCACTGACCTCCTAAGTTTCGAGCTGGACTCAGTG
glp-1	13	CTCCATTTGCGAATTGATCAGCACATCTTGCCTCCTAAGTTTCGAGCTGGACTCAGTG
glp-1	14	GAAGCAAGATCCATACACTTTCGTTGCTCGCCTCCTAAGTTTCGAGCTGGACTCAGTG
glp-1	15	CCATATTGGCATTCGCAATATCCAGTATTCCCTCCTAAGTTTCGAGCTGGACTCAGTG
glp-1	16	GGAGCATAACTGTCTATCCTTTATTTCGCAGCCTCCTAAGTTTCGAGCTGGACTCAGTG
glp-1	17	ATCTCCAGAGAATCCGTTGGGGCAGTTACCCTCCTAAGTTTCGAGCTGGACTCAGTG
glp-1	18	GCAGTGTGGTCTCTGTAGTGGAAGATCACAACCTCCTAAGTTTCGAGCTGGACTCAGTG
glp-1	19	ACATGTCGATAGCCTCCTCGCAATACTCCTCCTAAGTTTCGAGCTGGACTCAGTG
glp-1	20	AGTTGTTAACACACGTTTCTTCGATGAGGCATCCTCCTAAGTTTCGAGCTGGACTCAGTG
glp-1	21	CCCGAGTCGCATACACATCTGAAGTTCTTCCTCCTAAGTTTCGAGCTGGACTCAGTG
glp-1	22	GTTCACAATATCGACCGGATTTTCCAATTGGGCCTCCTAAGTTTCGAGCTGGACTCAGTG
glp-1	23	TAGCAGAGTCCGTTGTTGCAAGGATCCGAACCTCCTAAGTTTCGAGCTGGACTCAGTG
glp-1	24	TCTTGACAGATACACGTCGGATTTTCACCATCCTCCTAAGTTTCGAGCTGGACTCAGTG
glp-1	25	TACTCCGGACTTGTTTCCATTCGATTCGGTCCTCCTAAGTTTCGAGCTGGACTCAGTG
glp-1	26	GACGGTGGTGGTGTCAGATGATTTGTTTCGCCCTCCTAAGTTTCGAGCTGGACTCAGTG
glp-1	27	GACGATGCTGCACTTGTTGGCGTTTTTCGCCTCCTAAGTTTCGAGCTGGACTCAGTG
glp-1	28	ACCGTCTTTTCACATCCTTCCTTAGCGCCTCCTAAGTTTCGAGCTGGACTCAGTG
glp-1	29	AAGCATTATCGGTGTTCTTCCGTCTTCGTCCCTCCTAAGTTTCGAGCTGGACTCAGTG
glp-1	30	GTTTGTCCTTATTAGAGCTTCGTCGGACCAGCCTCCTAAGTTTCGAGCTGGACTCAGTG
glp-1	31	TATTACCATTTCCTCGTTATCGTGCATCGCCCTCCTAAGTTTCGAGCTGGACTCAGTG
glp-1	32	ATGAAGAGCTGTTCGTCCTTTATACTTGTTGGCCTCCTAAGTTTCGAGCTGGACTCAGTG
glp-1	33	ACTTGATGTTTTCCGAGTTCACGTGCTACTACCTCCTAAGTTTCGAGCTGGACTCAGTG
glp-1	34	TCGAATTGCCTCTGTTGTAATGACATCTTCCCCTCCTAAGTTTCGAGCTGGACTCAGTG
glp-1	35	TGATTGACTGACTCATTTGTGATTGGAGCTGTCCTCCTAAGTTTCGAGCTGGACTCAGTG
glp-1	36	TCGCATCTGGTCCTGCAGCTTGAACACCTCCTAAGTTTCGAGCTGGACTCAGTG
glp-1	37	GAGAGGGATTTCGTCGGCTGGTAGATCAGCCCTCCTAAGTTTCGAGCTGGACTCAGTG
glp-1	38	ACTATAATCGCTACAGTGTCTCTTGGTATTGGCCTCCTAAGTTTCGAGCTGGACTCAGTG
glp-1	39	TCGTTGATTCCATCGGAGGCATCCAGACCCTCCTAAGTTTCGAGCTGGACTCAGTG
glp-1	40	AACTCTTTCCATTTCATGTTCACCATCCCCCTCCTAAGTTTCGAGCTGGACTCAGTG
glp-1	41	TGCATTAGTGTTTCTCCTCCGGTAGCTTGCCTCCTAAGTTTCGAGCTGGACTCAGTG
glp-1	42	GGTATTGACATTTGGAGAATGGTCTTTGCCCCCTCCTAAGTTTCGAGCTGGACTCAGTG
glp-1	43	GATCACGAATGACAGTCTCTTTTGATTTCTCGCCTCCTAAGTTTCGAGCTGGACTCAGTG
glp-1	44	CTCCGTTAGCACATGTAGTTGGAGTGCACCCTCCTAAGTTTCGAGCTGGACTCAGTG
glp-1	45	CATCGTTGTAACACGTTCCATTGCTCCGACCTCCTAAGTTTCGAGCTGGACTCAGTG
glp-1	46	TCTCACATCGTTGTCCAGTGAATCCTTGTTCCTCCTAAGTTTCGAGCTGGACTCAGTG
glp-1	47	CTTCATCTCTGTTCGGAATACATCTTCCATCCTCCTAAGTTTCGAGCTGGACTCAGTG
glp-1	48	CTCCATAGCCTTCTTCACAGCCTTTTTGCCTCCTAAGTTTCGAGCTGGACTCAGTG

Table S4. Sequence of probes against *glp-1*. Primary probes carried the FLAPx extension shown in blue.

mRNA	Probe	5' - probe - FLAPx - 3'
puf-5	1	TTATCACTAGATGGCGTTTCTAGTAGAGGCACCCTCCTAAGTTTCGAGCTGGACTCAGTG
puf-5	2	ACGGTTGACACGATTCTTGATCCGATCGAACCCTCCTAAGTTTCGAGCTGGACTCAGTG
puf-5	3	TGTTGGACGACATAGTTCCCGTATTGATGGAACCTCCTAAGTTTCGAGCTGGACTCAGTG
puf-5	4	ACAAGATGTCCAGAGCATCACGGTTCGTCCCTCCTAAGTTTCGAGCTGGACTCAGTG
puf-5	5	CTGATCCTTCACATATCCATCGAAGATTTCGCCTCCTAAGTTTCGAGCTGGACTCAGTG
puf-5	6	ACTTGTCTTGCGACATCGATAGAATGTTACGGCCTCCTAAGTTTCGAGCTGGACTCAGTG
puf-5	7	ACGAGACGGCAACCATACTTGTCTTGGCCCTCCTAAGTTTCGAGCTGGACTCAGTG
puf-5	8	CAGTTTGACAACTTTCTGCAGAACGTGGATGGCCTCCTAAGTTTCGAGCTGGACTCAGTG
puf-5	9	GATCTTCTGGGAAATGGCGCTCCAGGAACCTCCTAAGTTTCGAGCTGGACTCAGTG
puf-5	10	GATCGAACATTGCTCTGGACGTTTCCAACGCCTCCTAAGTTTCGAGCTGGACTCAGTG
puf-5	11	TGACGTATTGTTGGCGGTGAAATCGGCAAACGCCTCCTAAGTTTCGAGCTGGACTCAGTG
puf-5	12	AGTCAGCAGGAGTCAAGTTCAATGGGCCTCCTCCTAAGTTTCGAGCTGGACTCAGTG
puf-5	13	TTCAGTTTGTTCATGAAATGGGCACTGATGTCCCTCCTAAGTTTCGAGCTGGACTCAGTG
puf-5	14	TGAGTGGAGTTGGCATAGCCCAGTATGGCCTCCTAAGTTTCGAGCTGGACTCAGTG
puf-5	15	TTGGCTCATTCGTCATCGTCATTGGCACCCTCCTAAGTTTCGAGCTGGACTCAGTG
puf-5	16	TGAGCTTCTGGAGCGACTCGATTATTTTCTTCCTCCTAAGTTTCGAGCTGGACTCAGTG
puf-5	17	TTTGGCATAGAGGCGCATTTCCGATGCCCTCCTAAGTTTCGAGCTGGACTCAGTG
puf-5	18	GCGTGCCACTGATGTCATGAGTCCATCCTCCTAAGTTTCGAGCTGGACTCAGTG
puf-5	19	GGATTATCAGACAGCTTGTCGATGGTTTGCTCCTCCTAAGTTTCGAGCTGGACTCAGTG
puf-5	20	TGATCTTTTCGACGAGCTTCATCGCGATCCCTCCTAAGTTTCGAGCTGGACTCAGTG
puf-5	21	TTTCGATCAATCCGTTGTCACACATCTTGCCCTCCTAAGTTTCGAGCTGGACTCAGTG
puf-5	22	GGCGAGTATTGGAAGCGCTGGTTCCCACCTCCTAAGTTTCGAGCTGGACTCAGTG
puf-5	23	TTTGGTGATCGCTGATCGACGATGAATCCGCCTCCTAAGTTTCGAGCTGGACTCAGTG
puf-5	24	GCTTTCGAGTTGATTCTTCCAGTACTGTCACCCTCCTAAGTTTCGAGCTGGACTCAGTG
puf-5	25	GAGGTCATCCCGAATGTTTCCGCTGTTGCCTCCTAAGTTTCGAGCTGGACTCAGTG
puf-5	26	TTCGATGATTGTATCACGGTACATTTCCATGACCTCCTAAGTTTCGAGCTGGACTCAGTG
puf-5	27	GACATCGAATTTCTGGATCGACATCTGCACCCTCCTAAGTTTCGAGCTGGACTCAGTG
puf-5	28	CGGTGTAGACGGTGTCAAGGCAGCCAGACCTCCTAAGTTTCGAGCTGGACTCAGTG
puf-5	29	CCATCTTACGTTCCTCTTTTCCGAGAAGTGCCTCCTAAGTTTCGAGCTGGACTCAGTG
puf-5	30	AGGCGTTCCTGTTCGTCAAGGGTTGCATCCTCCTAAGTTTCGAGCTGGACTCAGTG
puf-5	31	CCAGAGGACTTGATGACGTATTGAACGACGTACCTCCTAAGTTTCGAGCTGGACTCAGTG
puf-5	32	TAGCGAACTCGTTCGATGAAAGTCGGAAGCAGCCTCCTAAGTTTCGAGCTGGACTCAGTG
puf-5	33	AGGAGCTGAAGACGTGTGTTGAAGCAATGGAGCCTCCTAAGTTTCGAGCTGGACTCAGTG
puf-5	34	AACAGTCATCAGGTTGTCATCGCGACACACCTCCTAAGTTTCGAGCTGGACTCAGTG
puf-5	35	ATTTGACGAAGAAACTCCACGCACTAATTGGTCCTCCTAAGTTTCGAGCTGGACTCAGTG
puf-5	36	TCAACAAACTTCTGGATGATGAAATTTCCGGCCCTCCTAAGTTTCGAGCTGGACTCAGTG
puf-5	37	CACTGCGGCAAAGACTGGTGAAGACAGCCCTCCTAAGTTTCGAGCTGGACTCAGTG
puf-5	38	TTGTCAAAGAGCACAAAGTGCATCTCGTTATCCCTCCTAAGTTTCGAGCTGGACTCAGTG
puf-5	39	TGACTCCAGTTCTATCCATAGCGAAATCGACCTCCTAAGTTTCGAGCTGGACTCAGTG
puf-5	40	AGCGATCCGTTGCTAACAACATCTTGGAGACCTCCTAAGTTTCGAGCTGGACTCAGTG
puf-5	41	ACACGGATCACTCGACTTGGCAAATGGATCCTCCTAAGTTTCGAGCTGGACTCAGTG
puf-5	42	TCCCATGAAGTTGAACAGAGGAATGTTGGACGCCTCCTAAGTTTCGAGCTGGACTCAGTG
puf-5	43	GAGAATGCACCTCCATCGAAGGATCCGCCTCCTAAGTTTCGAGCTGGACTCAGTG
puf-5	44	CAGAGGAAAAACGCTCAAGGCGGCCGGAACCTCCTAAGTTTCGAGCTGGACTCAGTG
puf-5	45	AGCAAGAGAGGTGGAGCAAAGAGAAAAGCTCCCCTCCTAAGTTTCGAGCTGGACTCAGTG
puf-5	46	TGATCGGTGCAAAGTGGCAGAAAATCAAGACTCCTCCTAAGTTTCGAGCTGGACTCAGTG
puf-5	47	TCGTTTCCAACGGAAAAATCGGCAAGCCCCCTCCTAAGTTTCGAGCTGGACTCAGTG
puf-5	48	GACAGCCCAGGCAGGCAAAAGACGGGCCTCCTAAGTTTCGAGCTGGACTCAGTG

Table S5. Sequence of probes against *puf-5*. Primary probes carried the FLAPx extension shown in blue.

mRNA	Probe	5' - probe - FLAPx - 3'
tbb-2	1	AGTGTACCAATGGAGGAAAGCCTTGCGGCCCTCCTAAGTTTCGAGCTGGACTCAGTG
tbb-2	2	GTTCGGGATCCATTCGACGAAGTAGGACGAGCCTCCTAAGTTTCGAGCTGGACTCAGTG
tbb-2	3	TGGGAATCGGAGACAGGTGGTAACTCCGGCCTCCTAAGTTTCGAGCTGGACTCAGTG
tbb-2	4	ACCGAGAATGAGCTCATGATTCTGTCTGGCCTCCTAAGTTTCGAGCTGGACTCAGTG
tbb-2	5	CACATTGTCGACAAGCTCAGCTCCTTCCCTCCTAAGTTTCGAGCTGGACTCAGTG
tbb-2	6	GACAGAATCCATGGTTCCTGGTTCGAGATCCCTCCTAAGTTTCGAGCTGGACTCAGTG
tbb-2	7	CCAACACGGCGCGTGGCACATACTTTCCTCCTAAGTTTCGAGCTGGACTCAGTG
tbb-2	8	GTCGGAGATGACCTCCCAGAATTTGGATCCCTCCTAAGTTTCGAGCTGGACTCAGTG
tbb-2	9	TTATTGCTCCGATTCGTAAGTCTCTCCAGCCTCCTAAGTTTCGAGCTGGACTCAGTG
tbb-2	10	GGCAGTTGCTTCTTGGTATTGTTGGTATTCTGCCTCCTAAGTTTCGAGCTGGACTCAGTG
tbb-2	11	ATGAGATCGTTCATGTTGCTCTCGGCTTCCTCCTAAGTTTCGAGCTGGACTCAGTG
tbb-2	12	GTGAACTCCATCTCGTCCATTCCTTCTCCTCCTAAGTTTCGAGCTGGACTCAGTG
tbb-2	13	AAGGTGGCAGCCATCTTGAGTCCTCTCCTCCTAAGTTTCGAGCTGGACTCAGTG
tbb-2	14	GTGGGATGTCACAAACGGCGGTCTTGACGCCTCCTAAGTTTCGAGCTGGACTCAGTG
tbb-2	15	CTTGTTCTGAACGTTGAGCATTTGCTCGTCACCTCCTAAGTTTCGAGCTGGACTCAGTG
tbb-2	16	CTCTCTCATCGACATGCGTCCACGGACCTCCTAAGTTTCGAGCTGGACTCAGTG
tbb-2	17	GTCTTGGGTCACAGGCAGCCATCATGCCTCCTAAGTTTCGAGCTGGACTCAGTG
tbb-2	18	CTTGGCATCGAACATTTGTTGGGTGAGCTCCCTCCTAAGTTTCGAGCTGGACTCAGTG
tbb-2	19	CCCTTGGCGGAAAGTGGTGCGAATCCTCCTCCTAAGTTTCGAGCTGGACTCAGTG
tbb-2	20	AAGCTTGCGGAGATCGGCATTGAGCTGTCCTCCTAAGTTTCGAGCTGGACTCAGTG
tbb-2	21	GGTTGGGTTGGTGAGTTTGAGGGTACGGTAGCCCTCCTAAGTTTCGAGCTGGACTCAGTG
tbb-2	22	ATGTCGTAGAGGGCCTCGTTGTCAATGCCCTCCTAAGTTTCGAGCTGGACTCAGTG
tbb-2	23	TAGGTCTCATCGGTGTTCTCAACAAGCTGCCTCCTAAGTTTCGAGCTGGACTCAGTG
tbb-2	24	GGACGGAGAGGGTGGCATTGTATGGTTCTACCTCCTAAGTTTCGAGCTGGACTCAGTG
tbb-2	25	ACTGTGTCGGACACCTTTGGCGATGGTACCTCCTAAGTTTCGAGCTGGACTCAGTG
tbb-2	26	TCTTCGCGGATTTTGGAGATGAGAAGTGTTCCCCTCCTAAGTTTCGAGCTGGACTCAGTG
tbb-2	27	TTCCAGATCCGGTTCCTCCTCCGAGACCTCCTAAGTTTCGAGCTGGACTCAGTG
tbb-2	28	CTTCGGCTTCCTTGCGGATCACGTCACCTCCTAAGTTTCGAGCTGGACTCAGTG
tbb-2	29	TGTAGTGACCCTTGGCCCAGTTGTTTCCCCTCCTAAGTTTCGAGCTGGACTCAGTG
tbb-2	30	CTCCGCTTTGTCCGAACACAAAGTTGTCAGCCTCCTAAGTTTCGAGCTGGACTCAGTG
tbb-2	31	GTTGTTGGCTTCGTTGTAGTAGACGTCAATGCCCTCCTAAGTTTCGAGCTGGACTCAGTG
tbb-2	32	TCAAGCTGGAGATCCGTCTCTCCCTTCCTCCTAAGTTTCGAGCTGGACTCAGTG
tbb-2	33	ATTTGGTTTCCGCATTGTCCGGCTTGCCCTCCTAAGTTTCGAGCTGGACTCAGTG
tbb-2	34	ATAGCGGCCACGGTCAGGTAACGTCCCCTCCTAAGTTTCGAGCTGGACTCAGTG
tbb-2	35	CGACGGTAAGGGCACGGTAAGCCTGGGCCTCCTAAGTTTCGAGCTGGACTCAGTG
tbb-2	36	CGGAACAGCTGGCCGAATGGTCCAGAGCCTCCTAAGTTTCGAGCTGGACTCAGTG
tbb-2	37	CCTCAGCGTATCCGTCGACGTCGTCTCCTCCTAAGTTTCGAGCTGGACTCAGTG
tbb-2	38	AGGTTCCGTCTGGCTGGATTCCGTGCCCTCCTAAGTTTCGAGCTGGACTCAGTG
tbb-2	39	AACATAGCAGTGAACTGCTCTGAGATACGCCCTCCTAAGTTTCGAGCTGGACTCAGTG
tbb-2	40	AGTGAAGACGTGGGAATGGAACCATGTTGACGCCTCCTAAGTTTCGAGCTGGACTCAGTG
tbb-2	41	ATGGTGAGGGATACAAGATGGTTCAAATCACCCCTCCTAAGTTTCGAGCTGGACTCAGTG
tbb-2	42	GTGAGTGAGTTGGAATCCTTGAAGACAATCGCCCTCCTAAGTTTCGAGCTGGACTCAGTG
tbb-2	43	GAAAAGCTCTTGGATAGCGGTCGAGTTTCCAACCTCCTAAGTTTCGAGCTGGACTCAGTG

Table S6. Sequence of probes against *tbb-2*. Primary probes carried the FLAPx extension shown in blue.

mRNA	Probe	5' - probe - FLAPx - 3'
pccb-1	1	CCAGGCGTAGTTGATGTCTCCACGAAGATCCTCCTAAGTTTCGAGCTGGACTCAGTG
pccb-1	2	TTTGATGACATGACATCGTAAGCTCCTCCCCTCCTAAGTTTCGAGCTGGACTCAGTG
pccb-1	3	GAGTAATGATGGTAATCTTTGGAACGGTGGCCCCTCCTAAGTTTCGAGCTGGACTCAGTG
pccb-1	4	GCATCCAGCAGCAAACTTTGGATTGTTTCCCCTCCTAAGTTTCGAGCTGGACTCAGTG
pccb-1	5	GAATCCAATGACCAAGTTCTTGGCGTAGTCTCCTCCTAAGTTTCGAGCTGGACTCAGTG
pccb-1	6	AGCGTGAACAACGTCCTTCATGTTGTAGGCCCTCCTAAGTTTCGAGCTGGACTCAGTG
pccb-1	7	GCAGCACGGATTGGAGCAGCATCAGTGCCTCCTAAGTTTCGAGCTGGACTCAGTG
pccb-1	8	TGAGCGACTCCAGAGGTGACAGTGTGAGTCCTCCTAAGTTTCGAGCTGGACTCAGTG
pccb-1	9	GCTTTGACAACATCTGGGCCAGTGATGAACCTCCTAAGTTTCGAGCTGGACTCAGTG
pccb-1	10	CGAGTAGACGGCTCCTCCAGCACATGCCTCCTAAGTTTCGAGCTGGACTCAGTG
pccb-1	11	AAGCCATCACGTTCTCTTGGAAGATATCGGCCTCCTAAGTTTCGAGCTGGACTCAGTG
pccb-1	12	CCGATGACTGGGGCTCCGACAAGCATCCTCCTAAGTTTCGAGCTGGACTCAGTG
pccb-1	13	CAGGATATTTCTCTTTCTGCATACCGAAGTCCCTCCTAAGTTTCGAGCTGGACTCAGTG
pccb-1	14	TGCAGGTGTGCTCGGCAAACATGTCATACCTCCTAAGTTTCGAGCTGGACTCAGTG
pccb-1	15	GCAACCTTGATGGTATGAGCGATCGAACTGCCTCCTAAGTTTCGAGCTGGACTCAGTG
pccb-1	16	TTAGAGTGGAATGTTTCCGTGCTTCTTCCATCCTCCTAAGTTTCGAGCTGGACTCAGTG
pccb-1	17	GTTCTTCAACTTCTTGCTTTCAAGCATGTTCACCTCCTAAGTTTCGAGCTGGACTCAGTG
pccb-1	18	GCGGCTGGGAACGGGTTGCTGAACAGCCTCCTAAGTTTCGAGCTGGACTCAGTG
pccb-1	19	CAGTGTATTCCTCCTCGTGTTGAACGGCGCCTCCTAAGTTTCGAGCTGGACTCAGTG
pccb-1	20	CTCCCATCACAGCAACCTCAGCAGTTCCTCCTAAGTTTCGAGCTGGACTCAGTG
pccb-1	21	GATGATACCTCCGTACTCTTGGGCAGTTCCTCCTAAGTTTCGAGCTGGACTCAGTG
pccb-1	22	CAATTCCGACAGTGCGTCCGTTCATTCTGCCTCCTAAGTTTCGAGCTGGACTCAGTG
pccb-1	23	TGGAACAGCTCTGTCCCATGGATCCTCCTCCTAAGTTTCGAGCTGGACTCAGTG
pccb-1	24	CTCCTGGGTGACCTCCTCGTTGGTAACCTCCTAAGTTTCGAGCTGGACTCAGTG
pccb-1	25	TACCCAGCAAGCGACTCAACTCCTTCCCTCCTAAGTTTCGAGCTGGACTCAGTG
pccb-1	26	GGATACGGGCACCTCCGGAGTCATTGCCTCCTAAGTTTCGAGCTGGACTCAGTG
pccb-1	27	ATTTCTCCACGTCCAGTGACAACCGAATCCCTCCTAAGTTTCGAGCTGGACTCAGTG
pccb-1	28	TGTTAGCTTTCCGCGAGCATGTTGAGCGCCTCCTAAGTTTCGAGCTGGACTCAGTG
pccb-1	29	GACGCGCTTCTTTCCACCTCCGAGAACCTCCTAAGTTTCGAGCTGGACTCAGTG
pccb-1	30	GCTTTCTCTCTGGTCTCATCGATCTTATCCTCCTAAGTTTCGAGCTGGACTCAGTG
pccb-1	31	CTCGCACACCTTCTTTCTGGTCTCTGCCTCCTAAGTTTCGAGCTGGACTCAGTG
pccb-1	32	GGAATGATAATGTCGTCGACGAATCCTCTGACCTCCTAAGTTTCGAGCTGGACTCAGTG
pccb-1	33	TGGCAAGAAACCGGGAACGTCAACCAAAGTGACCTCCTAAGTTTCGAGCTGGACTCAGTG
pccb-1	34	ATTGGGATGTTGAAAGCATCGCAGAATCGGACCCTCCTAAGTTTCGAGCTGGACTCAGTG
pccb-1	35	AACGAGCTCCTTTCACGGAAGAGTTGATATCACCTCCTAAGTTTCGAGCTGGACTCAGTG
pccb-1	36	CATAATCTCGAAGAAATCTCCCTCGTCGACCCTCCTAAGTTTCGAGCTGGACTCAGTG
pccb-1	37	CAGTGCTTTCCAATGGAACAACAGTATCCAAACCTCCTAAGTTTCGAGCTGGACTCAGTG
pccb-1	38	TGAGCGCATCAACATCGTTGTCGAAAGCACCCTCCTAAGTTTCGAGCTGGACTCAGTG
pccb-1	39	GGAGGTATCACGAACCATGAAAGTGAAGTCGGCCTCCTAAGTTTCGAGCTGGACTCAGTG
pccb-1	40	CCCATAATCATAGAGATTTGAGGAACGACACCCCTCCTAAGTTTCGAGCTGGACTCAGTG
pccb-1	41	CCTCTCTCATGATCTTGACGATCTTTTTGGCCTCCTAAGTTTCGAGCTGGACTCAGTG
pccb-1	42	TATCATTACGGAAAAGAATGGAGACTGCACCCCCTCCTAAGTTTCGAGCTGGACTCAGTG
pccb-1	43	GGCAAAAGCGTAGAGAAGTTTGGCTCCGTGACCTCCTAAGTTTCGAGCTGGACTCAGTG
pccb-1	44	AGTGGAAGATAGTTGAAAAGCTCTCTGAGGCTCCTCCTAAGTTTCGAGCTGGACTCAGTG
pccb-1	45	TGAATGGATGACAGAGATCCTCCGAAAACAGTCCTCCTAAGTTTCGAGCTGGACTCAGTG
pccb-1	46	GTCTTGGGAGAAAACAAAGACGGTACGTCCGTCCTCCTAAGTTTCGAGCTGGACTCAGTG
pccb-1	47	TTCTATCCAAAAGAAGATCAATGCGTTCGCGACCTCCTAAGTTTCGAGCTGGACTCAGTG

Table S7. Sequence of probes against *pccb-1*. Primary probes carried the FLAPx extension shown in blue.

Fluorophores	Complementary FLAPx, 5’ -> 3’
Cy3	/5Cy3/CACTGAGTCCAGCTCGAAACTTAGGAGG/3Cy3Sp/
Cy5	/5Cy5/CACTGAGTCCAGCTCGAAACTTAGGAGG/3Cy5Sp/

Table S8. Sequence of complementary FLAPx probes. The probes are modified with two Cy3 or Cy5 moieties at 5’ and 3’. Modification symbols are shown.

SUPPLEMENTARY DATA

Data S1. RNA relative enrichment within oocyte P-bodies, related to Figures 1 and 2. (separate file)
RNA relative enrichments within oocytes P-bodies.

Data S2. RNA-Seq abundances, related to Figures 1 and 2. (separate file)
RNA-Seq abundances of sorted P-bodies, whole animal pre-sorted extracts, and dissected oocytes.

Data S3. Estimated condensed and dissolved mRNA copy numbers in oocytes, related to Figure 1. (separate file)
Transcriptome-wide extrapolation of the mRNA copy numbers condensed in cytosolic P-bodies and dispersed in the cytosolic phase.

Data S4. GO analysis of P-body enriched and depleted mRNAs, related to Figure 2. (separate file)
Full list of GO terms found for P-body enriched and depleted mRNAs.

REFERENCES

1. Adekunle, D.A., and Hubstenberger, A. (2020). The multiscale and multiphase organization of the transcriptome. Emerg Top Life Sci. 10.1042/ETLS20190187.
2. Berry, S., and Pelkmans, L. (2022). Mechanisms of cellular mRNA transcript homeostasis. Trends in Cell Biology *32*, 655–668. 10.1016/j.tcb.2022.05.003.
3. Hubstenberger, A., Courel, M., Bénard, M., Souquere, S., Ernoult-Lange, M., Chouaib, R., Yi, Z., Morlot, J.-B., Munier, A., Fradet, M., et al. (2017). P-Body Purification Reveals the Condensation of Repressed mRNA Regulons. Mol. Cell *68*, 144-157.e5. 10.1016/j.molcel.2017.09.003.
4. Roden, C.A., and Gladfelter, A.S. (2022). Design considerations for analyzing protein translation regulation by condensates. RNA *28*, 88–96. 10.1261/rna.079002.121.
5. Khong, A., and Parker, R. (2020). The landscape of eukaryotic mRNPs. RNA *26*, 229–239. 10.1261/rna.073601.119.
6. Hubstenberger, A., Cameron, C., Shtofman, R., Gutman, S., and Evans, T.C. (2012). A network of PUF proteins and Ras signaling promote mRNA repression and oogenesis in C.

elegans. Developmental Biology *366*, 218–231. 10.1016/j.ydbio.2012.03.019.
7. Lublin, A.L., and Evans, T.C. (2007). The RNA-binding proteins PUF-5, PUF-6, and PUF-7 reveal multiple systems for maternal mRNA regulation during C. elegans oogenesis. Developmental Biology *303*, 635–649. 10.1016/j.ydbio.2006.12.004.
8. Spike, C.A., Coetzee, D., Nishi, Y., Guven-Ozkan, T., Oldenbroek, M., Yamamoto, I., Lin, R., and Greenstein, D. (2014). Translational Control of the Oogenic Program by Components of OMA Ribonucleoprotein Particles in *Caenorhabditis elegans*. Genetics *198*, 1513–1533. 10.1534/genetics.114.168823.
9. Brangwynne, C.P., Eckmann, C.R., Courson, D.S., Rybarska, A., Hoege, C., Gharakhani, J., Jülicher, F., and Hyman, A.A. (2009). Germline P granules are liquid droplets that localize by controlled dissolution/condensation. Science *324*, 1729–1732. 10.1126/science.1172046.
10. Hubstenberger, A., Noble, S.L., Cameron, C., and Evans, T.C. (2013). Translation repressors, an RNA helicase, and developmental cues control RNP phase transitions during early development. Dev. Cell *27*, 161–173. 10.1016/j.devcel.2013.09.024.
11. Li, P., Banjade, S., Cheng, H.-C., Kim, S., Chen, B., Guo, L., Llaguno, M., Hollingsworth, J.V., King, D.S., Banani, S.F., et al. (2012). Phase transitions in the assembly of multivalent signalling proteins. Nature *483*, 336–340. 10.1038/nature10879.
12. Khong, A., Matheny, T., Jain, S., Mitchell, S.F., Wheeler, J.R., and Parker, R. (2017). The Stress Granule Transcriptome Reveals Principles of mRNA Accumulation in Stress Granules. Molecular Cell *68*, 808-820.e5. 10.1016/j.molcel.2017.10.015.
13. Lee, C.-Y.S., Putnam, A., Lu, T., He, S., Ouyang, J.P.T., and Seydoux, G. (2020). Recruitment of mRNAs to P granules by condensation with intrinsically-disordered proteins. eLife *9*. 10.7554/eLife.52896.
14. Namkoong, S., Ho, A., Woo, Y.M., Kwak, H., and Lee, J.H. (2018). Systematic Characterization of Stress-Induced RNA Granulation. Mol. Cell *70*, 175-187.e8. 10.1016/j.molcel.2018.02.025.
15. Hondele, M., Sachdev, R., Heinrich, S., Wang, J., Vallotton, P., Fontoura, B.M.A., and Weis, K. (2019). DEAD-box ATPases are global regulators of phase-separated organelles. Nature *573*, 144–148. 10.1038/s41586-019-1502-y.
16. Kim, T.H., Tsang, B., Vernon, R.M., Sonenberg, N., Kay, L.E., and Forman-Kay, J.D. (2019). Phospho-dependent phase separation of FMRP and CAPRIN1 recapitulates regulation of translation and deadenylation. Science *365*, 825–829. 10.1126/science.aax4240.
17. Sheu-Gruttadauria, J., and MacRae, I.J. (2018). Phase Transitions in the Assembly and Function of Human miRISC. Cell *173*, 946-957.e16. 10.1016/j.cell.2018.02.051.
18. Corbet, G.A., and Parker, R. (2019). RNP Granule Formation: Lessons from P-Bodies and Stress Granules. Cold Spring Harb Symp Quant Biol *84*, 203–215. 10.1101/sqb.2019.84.040329.
19. Ivanov, P., Kedersha, N., and Anderson, P. (2019). Stress Granules and Processing Bodies in Translational Control. Cold Spring Harb Perspect Biol *11*. 10.1101/cshperspect.a032813.
20. Jud, M.C., Czerwinski, M.J., Wood, M.P., Young, R.A., Gallo, C.M., Bickel, J.S., Petty, E.L., Mason, J.M., Little, B.A., Padilla, P.A., et al. (2008). Large P body-like RNPs form in C. elegans oocytes in response to arrested ovulation, heat shock, osmotic stress, and anoxia and are regulated by the major sperm protein pathway. Dev. Biol. *318*, 38–51. 10.1016/j.ydbio.2008.02.059.
21. Lyon, A.S., Peeples, W.B., and Rosen, M.K. (2021). A framework for understanding the functions of biomolecular condensates across scales. Nat Rev Mol Cell Biol *22*, 215–235. 10.1038/s41580-020-00303-z.

22. McSwiggen, D.T., Mir, M., Darzacq, X., and Tjian, R. (2019). Evaluating phase separation in live cells: diagnosis, caveats, and functional consequences. Genes Dev. *33*, 1619–1634. 10.1101/gad.331520.119.
23. Mittag, T., and Pappu, R.V. (2022). A conceptual framework for understanding phase separation and addressing open questions and challenges. Molecular Cell *82*, 2201–2214. 10.1016/j.molcel.2022.05.018.
24. Klosin, A., Oltsch, F., Harmon, T., Honigmann, A., Jülicher, F., Hyman, A.A., and Zechner, C. (2020). Phase separation provides a mechanism to reduce noise in cells. Science *367*, 464–468. 10.1126/science.aav6691.
25. Riback, J.A., Zhu, L., Ferrolino, M.C., Tolbert, M., Mitrea, D.M., Sanders, D.W., Wei, M.-T., Kriwacki, R.W., and Brangwynne, C.P. (2020). Composition-dependent thermodynamics of intracellular phase separation. Nature *581*, 209–214. 10.1038/s41586-020-2256-2.
26. Tauber, D., Tauber, G., Khong, A., Treeck, B.V., Pelletier, J., and Parker, R. (2020). Modulation of RNA Condensation by the DEAD-Box Protein eIF4A. Cell *180*, 411-426.e16. 10.1016/j.cell.2019.12.031.
27. Alberti, S., and Hyman, A.A. (2021). Biomolecular condensates at the nexus of cellular stress, protein aggregation disease and ageing. Nat Rev Mol Cell Biol *22*, 196–213. 10.1038/s41580-020-00326-6.
28. Shin, Y., and Brangwynne, C.P. (2017). Liquid phase condensation in cell physiology and disease. Science *357*, eaaf4382. 10.1126/science.aaf4382.
29. Cirillo, L., Cieren, A., Barbieri, S., Khong, A., Schwager, F., Parker, R., and Gotta, M. (2020). UBAP2L Forms Distinct Cores that Act in Nucleating Stress Granules Upstream of G3BP1. Current Biology *30*, 698-707.e6. 10.1016/j.cub.2019.12.020.
30. Folkmann, A.W., Putnam, A., Lee, C.F., and Seydoux, G. (2021). Regulation of biomolecular condensates by interfacial protein clusters. Science *373*, 1218–1224. 10.1126/science.abg7071.
31. Elaswad, M.T., Watkins, B.M., Sharp, K.G., Munderloh, C., and Schisa, J.A. (2022). Large RNP granules in Caenorhabditis elegans oocytes have distinct phases of RNA-binding proteins. G3 (Bethesda) *12*, jkac173. 10.1093/g3journal/jkac173.
32. Langdon, E.M., Qiu, Y., Ghanbari Niaki, A., McLaughlin, G.A., Weidmann, C.A., Gerbich, T.M., Smith, J.A., Crutchley, J.M., Termini, C.M., Weeks, K.M., et al. (2018). mRNA structure determines specificity of a polyQ-driven phase separation. Science *360*, 922–927. 10.1126/science.aar7432.
33. Niepielko, M.G., Eagle, W.V.I., and Gavis, E.R. (2018). Stochastic Seeding Coupled with mRNA Self-Recruitment Generates Heterogeneous Drosophila Germ Granules. Curr. Biol. *28*, 1872-1881.e3. 10.1016/j.cub.2018.04.037.
34. Trcek, T., Grosch, M., York, A., Shroff, H., Lionnet, T., and Lehmann, R. (2015). Drosophila germ granules are structured and contain homotypic mRNA clusters. Nature Communications *6*, 7962. 10.1038/ncomms8962.
35. Trcek, T., Douglas, T.E., Grosch, M., Yin, Y., Eagle, W.V.I., Gavis, E.R., Shroff, H., Rothenberg, E., and Lehmann, R. (2020). Sequence-Independent Self-Assembly of Germ Granule mRNAs into Homotypic Clusters. Molecular Cell *78*, 941-950.e12. 10.1016/j.molcel.2020.05.008.
36. Franzmann, T.M., Jahnel, M., Pozniakovsky, A., Mahamid, J., Holehouse, A.S., Nüske, E., Richter, D., Baumeister, W., Grill, S.W., Pappu, R.V., et al. (2018). Phase separation of a yeast prion protein promotes cellular fitness. Science *359*. 10.1126/science.aao5654.
37. Iserman, C., Altamirano, C.D., Jegers, C., Friedrich, U., Zarin, T., Fritsch, A.W., Mittasch, M., Domingues, A., Hersemann, L., Jahnel, M., et al. (2020). Condensation of Ded1p

Promotes a Translational Switch from Housekeeping to Stress Protein Production. Cell *0*. 10.1016/j.cell.2020.04.009.
38. Riback, J.A., Katanski, C.D., Kear-Scott, J.L., Pilipenko, E.V., Rojek, A.E., Sosnick, T.R., and Drummond, D.A. (2017). Stress-Triggered Phase Separation Is an Adaptive, Evolutionarily Tuned Response. Cell *168*, 1028-1040.e19. 10.1016/j.cell.2017.02.027.
39. Hubstenberger, A., Cameron, C., Noble, S.L., Keenan, S., and Evans, T.C. (2015). Modifiers of solid RNP granules control normal RNP dynamics and mRNA activity in early development. J. Cell Biol. *211*, 703–716. 10.1083/jcb.201504044.
40. Boke, E., Ruer, M., Wühr, M., Coughlin, M., Lemaitre, R., Gygi, S.P., Alberti, S., Drechsel, D., Hyman, A.A., and Mitchison, T.J. (2016). Amyloid-like Self-Assembly of a Cellular Compartment. Cell *166*, 637–650. 10.1016/j.cell.2016.06.051.
41. Cheng, S., Altmeppen, G., So, C., Welp, L.M., Penir, S., Ruhwedel, T., Menelaou, K., Harasimov, K., Stützer, A., Blayney, M., et al. (2022). Mammalian oocytes store mRNAs in a mitochondria-associated membraneless compartment. Science *378*, eabq4835. 10.1126/science.abq4835.
42. McCarter, J., Bartlett, B., Dang, T., and Schedl, T. (1999). On the Control of Oocyte Meiotic Maturation and Ovulation inCaenorhabditis elegans. Developmental Biology *205*, 111–128. 10.1006/dbio.1998.9109.
43. Boag, P.R., Atalay, A., Robida, S., Reinke, V., and Blackwell, T.K. (2008). Protection of specific maternal messenger RNAs by the P body protein CGH-1 (Dhh1/RCK) during Caenorhabditis elegans oogenesis. J. Cell Biol. *182*, 543–557. 10.1083/jcb.200801183.
44. Jud, M., Razelun, J., Bickel, J., Czerwinski, M., and Schisa, J.A. (2007). Conservation of large foci formation in arrested oocytes of Caenorhabditis nematodes. Dev. Genes Evol. *217*, 221–226. 10.1007/s00427-006-0130-3.
45. Noble, S.L., Allen, B.L., Goh, L.K., Nordick, K., and Evans, T.C. (2008). Maternal mRNAs are regulated by diverse P body-related mRNP granules during early Caenorhabditis elegans development. J. Cell Biol. *182*, 559–572. 10.1083/jcb.200802128.
46. Merritt, C., Rasoloson, D., Ko, D., and Seydoux, G. (2008). 3′ UTRs Are the Primary Regulators of Gene Expression in the C. elegans Germline. Current Biology *18*, 1476–1482. 10.1016/j.cub.2008.08.013.
47. Mueller, F., Senecal, A., Tantale, K., Marie-Nelly, H., Ly, N., Collin, O., Basyuk, E., Bertrand, E., Darzacq, X., and Zimmer, C. (2013). FISH-quant: automatic counting of transcripts in 3D FISH images. Nat. Methods *10*, 277–278. 10.1038/nmeth.2406.
48. Tsanov, N., Samacoits, A., Chouaib, R., Traboulsi, A.-M., Gostan, T., Weber, C., Zimmer, C., Zibara, K., Walter, T., Peter, M., et al. (2016). smiFISH and FISH-quant - a flexible single RNA detection approach with super-resolution capability. Nucleic Acids Res. *44*, e165. 10.1093/nar/gkw784.
49. Stumpf, C.R., Kimble, J., and Wickens, M. (2008). A Caenorhabditis elegans PUF protein family with distinct RNA binding specificity. RNA *14*, 1550–1557. 10.1261/rna.1095908.
50. Tsukamoto, T., Gearhart, M.D., Spike, C.A., Huelgas-Morales, G., Mews, M., Boag, P.R., Beilharz, T.H., and Greenstein, D. (2017). LIN-41 and OMA Ribonucleoprotein Complexes Mediate a Translational Repression-to-Activation Switch Controlling Oocyte Meiotic Maturation and the Oocyte-to-Embryo Transition in *Caenorhabditis elegans*. Genetics *206*, 2007–2039. 10.1534/genetics.117.203174.
51. Banani, S.F., Rice, A.M., Peeples, W.B., Lin, Y., Jain, S., Parker, R., and Rosen, M.K. (2016). Compositional Control of Phase-Separated Cellular Bodies. Cell *166*, 651–663. 10.1016/j.cell.2016.06.010.

52. Adivarahan, S., Livingston, N., Nicholson, B., Rahman, S., Wu, B., Rissland, O.S., and Zenklusen, D. (2018). Spatial Organization of Single mRNPs at Different Stages of the Gene Expression Pathway. Mol. Cell *72*, 727-738.e5. 10.1016/j.molcel.2018.10.010.
53. Kar, M., Dar, F., Welsh, T.J., Vogel, L.T., Kühnemuth, R., Majumdar, A., Krainer, G., Franzmann, T.M., Alberti, S., Seidel, C.A.M., et al. (2022). Phase-separating RNA-binding proteins form heterogeneous distributions of clusters in subsaturated solutions. Proc Natl Acad Sci U S A *119*, e2202222119. 10.1073/pnas.2202222119.
54. Narayanan, A., Meriin, A., Andrews, J.O., Spille, J.-H., Sherman, M.Y., and Cisse, I.I. (2019). A first order phase transition mechanism underlies protein aggregation in mammalian cells. eLife *8*, e39695. 10.7554/eLife.39695.
55. Danielle A. Adekunle, and Eric T. Wang, (last) (2020). Transcriptome-wide organization of subcellular microenvironments revealed by ATLAS-Seq. Nucleic Acids Res. 10.1093/nar/gkaa334.
56. Lécuyer, E., Yoshida, H., Parthasarathy, N., Alm, C., Babak, T., Cerovina, T., Hughes, T.R., Tomancak, P., and Krause, H.M. (2007). Global Analysis of mRNA Localization Reveals a Prominent Role in Organizing Cellular Architecture and Function. Cell *131*, 174–187. 10.1016/j.cell.2007.08.003.
57. Mueller, F., Senecal, A., Tantale, K., Marie-Nelly, H., Ly, N., Collin, O., Basyuk, E., Bertrand, E., Darzacq, X., and Zimmer, C. (2013). FISH-quant: Automatic counting of transcripts in 3D FISH images. Nature Methods *10*, 277–278. 10.1038/nmeth.2406.
58. Hu, B., Yang, Y.-C.T., Huang, Y., Zhu, Y., and Lu, Z.J. (2017). POSTAR: a platform for exploring post-transcriptional regulation coordinated by RNA-binding proteins. Nucleic Acids Res *45*, D104–D114. 10.1093/nar/gkw888.
59. Squirrell, J.M., Eggers, Z., Luedke, N., Saari, B., Grimson, A., Lyons, G., Anderson, P., and White, J.G. (2006). CAR-1, a Protein That Localizes with the mRNA Decapping Component DCAP-1, Is Required for Cytokinesis and ER Organization in Caenorhabditis elegans Embryos. Molecular biology of the cell *17*, 336–344. 10.1091/mbc.E05.
60. Kamath, R.S., and Ahringer, J. (2003). Genome-wide RNAi screening in Caenorhabditis elegans. Methods *30*, 313–321. 10.1016/S1046-2023(03)00050-1.
61. Timmons, L., Court, D.L., and Fire, A. (2001). Ingestion of bacterially expressed dsRNAs can produce specific and potent genetic interference in Caenorhabditis elegans. Gene *263*, 103–112.
62. Timmons, L., and Fire, A. (1998). Specific interference by ingested dsRNA. Nature *395*, 854–854. 10.1038/27579.
63. Hubstenberger, A., Cameron, C., Shtofman, R., Gutman, S., and Evans, T.C. (2012). A network of PUF proteins and Ras signaling promote mRNA repression and oogenesis in C. elegans. Developmental Biology *366*, 218–231. 10.1016/j.ydbio.2012.03.019.
64. Schindelin, J., Arganda-Carreras, I., Frise, E., Kaynig, V., Longair, M., Pietzsch, T., Preibisch, S., Rueden, C., Saalfeld, S., Schmid, B., et al. (2012). Fiji: an open-source platform for biological-image analysis. Nat Methods *9*, 676–682. 10.1038/nmeth.2019.
65. Andrews, S. (2010). FastQC: A Quality Control Tool for High Throughput Sequence Data.
66. Goecks, J., Nekrutenko, A., Taylor, J., Afgan, E., Ananda, G., Baker, D., Blankenberg, D., Chakrabarty, R., Coraor, N., Goecks, J., et al. (2010). Galaxy: a comprehensive approach for supporting accessible, reproducible, and transparent computational research in the life sciences. Genome Biology *11*. 10.1186/gb-2010-11-8-r86.
67. Kim, D., Paggi, J.M., Park, C., Bennett, C., and Salzberg, S.L. (2019). Graph-based genome alignment and genotyping with HISAT2 and HISAT-genotype. Nature Biotechnology

37, 907–915. 10.1038/s41587-019-0201-4.
68. Pertea, M., Pertea, G.M., Antonescu, C.M., Chang, T.C., Mendell, J.T., and Salzberg, S.L. (2015). StringTie enables improved reconstruction of a transcriptome from RNA-seq reads. Nature Biotechnology *33*, 290–295. 10.1038/nbt.3122.
69. Anders, S., Pyl, P.T., and Huber, W. (2015). HTSeq-A Python framework to work with high-throughput sequencing data. Bioinformatics *31*, 166–169. 10.1093/bioinformatics/btu638.
70. Li, H., Handsaker, B., Wysoker, A., Fennell, T., Ruan, J., Homer, N., Marth, G., Abecasis, G., Durbin, R., and 1000 Genome Project Data Processing Subgroup (2009). The Sequence Alignment/Map format and SAMtools. Bioinformatics *25*, 2078–2079. 10.1093/bioinformatics/btp352.
71. Robinson, J.T., Thorvaldsdóttir, H., Winckler, W., Guttman, M., Lander, E.S., Getz, G., and Mesirov, J.P. (2011). Integrative genomics viewer. Nat Biotechnol *29*, 24–26. 10.1038/nbt.1754.
72. Thorvaldsdóttir, H., Robinson, J.T., and Mesirov, J.P. (2013). Integrative Genomics Viewer (IGV): high-performance genomics data visualization and exploration. Briefings in Bioinformatics *14*, 178–192. 10.1093/bib/bbs017.
73. Huber, W., Carey, V.J., Gentleman, R., Anders, S., Carlson, M., Carvalho, B.S., Bravo, H.C., Davis, S., Gatto, L., Girke, T., et al. (2015). Orchestrating high-throughput genomic analysis with Bioconductor. Nat Methods *12*, 115–121. 10.1038/nmeth.3252.
74. Love, M.I., Huber, W., and Anders, S. (2014). Moderated estimation of fold change and dispersion for RNA-seq data with DESeq2. Genome Biology *15*, 1–21. 10.1186/s13059-014-0550-8.
75. Lawrence, M., Huber, W., Pagès, H., Aboyoun, P., Carlson, M., Gentleman, R., Morgan, M.T., and Carey, V.J. (2013). Software for Computing and Annotating Genomic Ranges. PLOS Computational Biology *9*, e1003118. 10.1371/journal.pcbi.1003118.
76. Lawrence, M., Gentleman, R., and Carey, V. (2009). rtracklayer: an R package for interfacing with genome browsers. Bioinformatics *25*, 1841–1842. 10.1093/bioinformatics/btp328.
77. Brenner, S. (1974). The genetics of Caenorhabditis elegans. Genetics *77*, 71–94.
78. Barbee, S.A., Lublin, A.L., and Evans, T.C. (2002). A novel function for the Sm proteins in germ granule localization during C. elegans Embryogenesis. Current Biology *12*, 1502–1506. 10.1016/S0960-9822(02)01111-9.
79. Tsanov, N., Samacoits, A., Chouaib, R., Traboulsi, A.-M., Gostan, T., Weber, C., Zimmer, C., Zibara, K., Walter, T., Peter, M., et al. (2016). smiFISH and FISH-quant - a flexible single RNA detection approach with super-resolution capability. Nucleic Acids Research *44*, e165. 10.1093/nar/gkw784.

Figure 1

Click here to access/download;Figure;Fig1_600ppi.tif

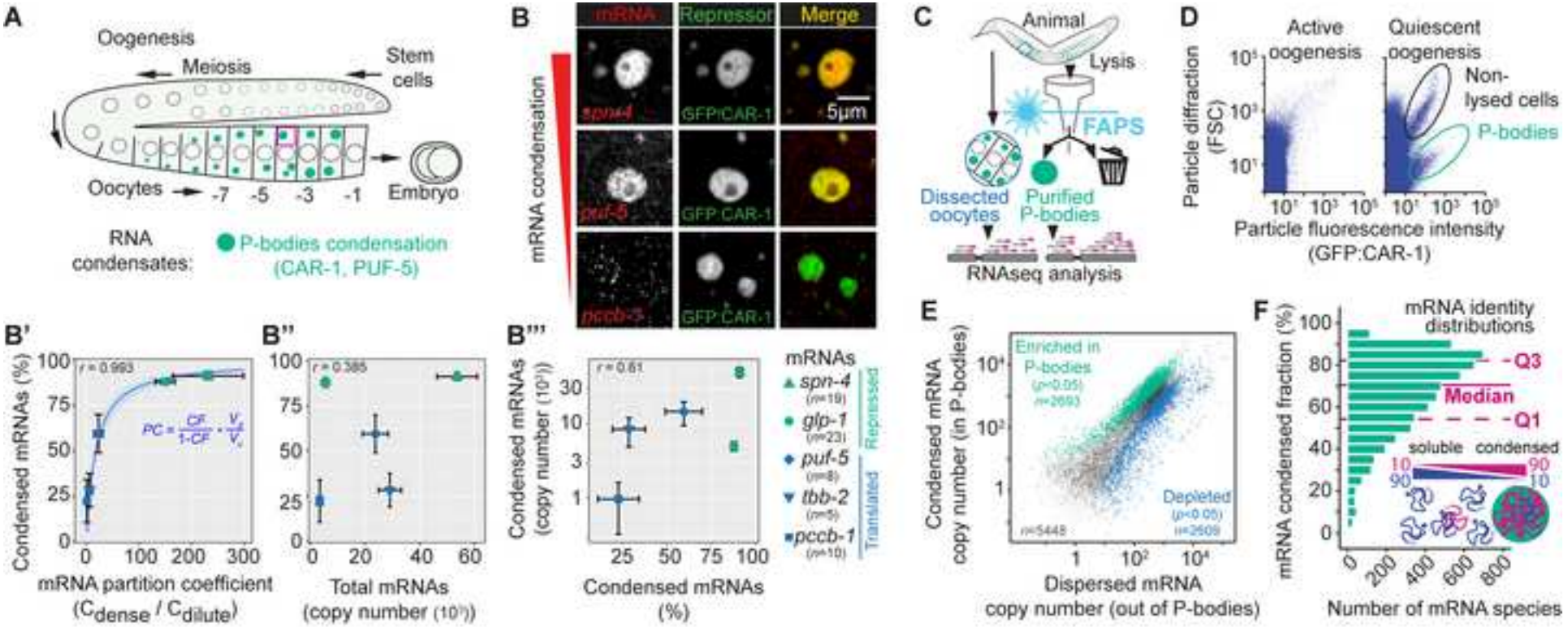

Figure 2

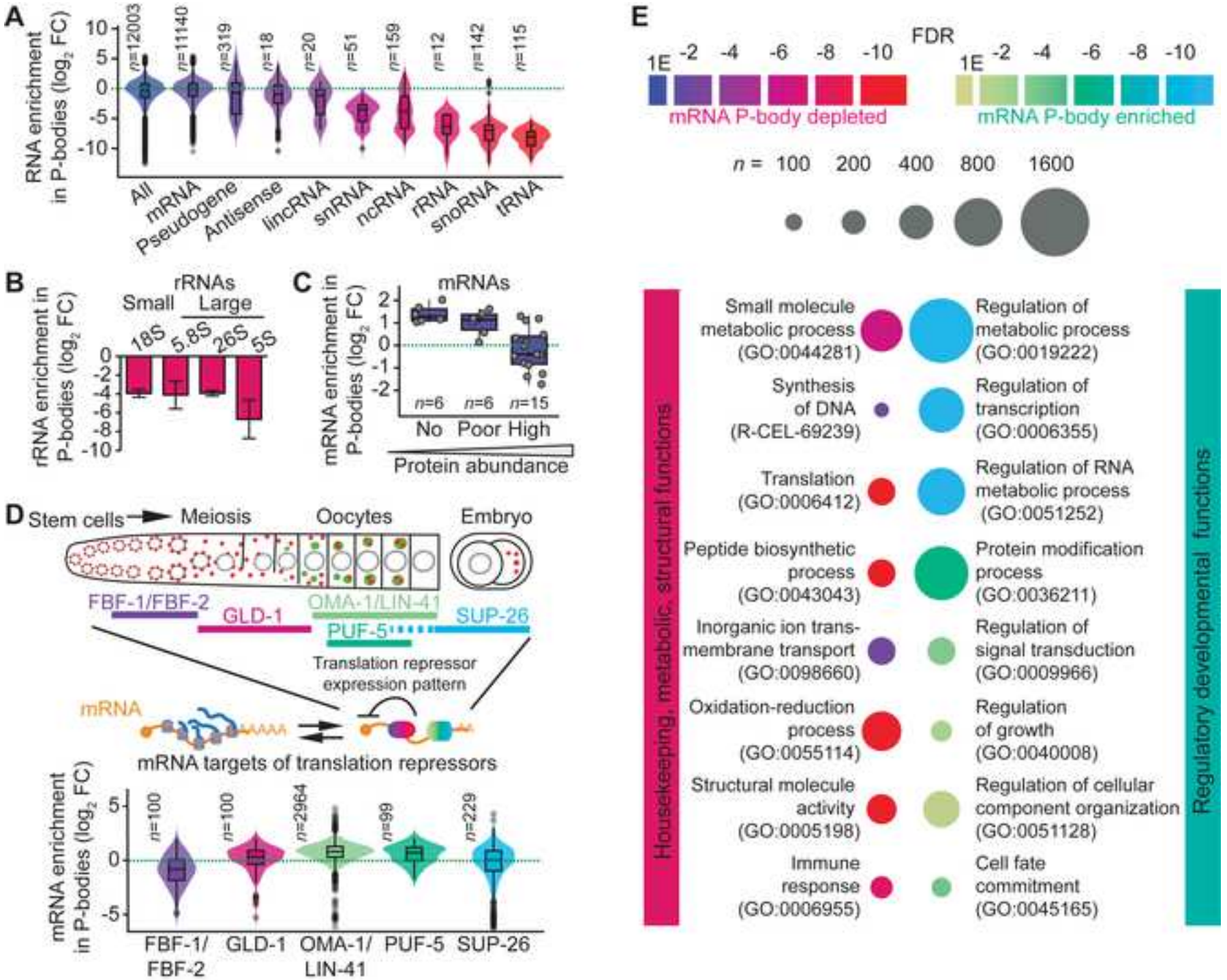

Figure 3

Click here to access/download;Figure;Fig3_600ppi.tif

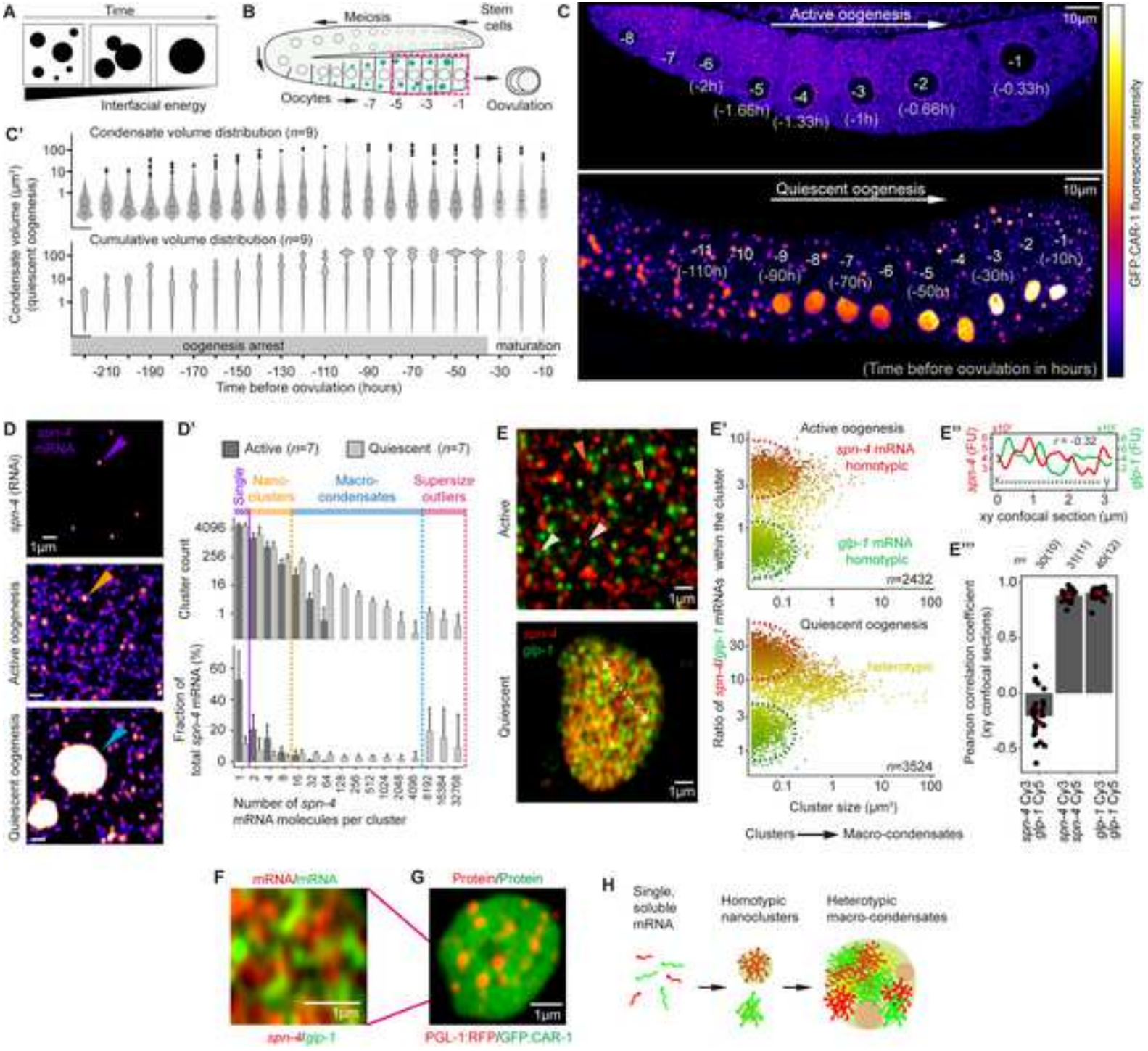

Figure 4

Click here to access/download;Figure;Fig4_600ppi.tif

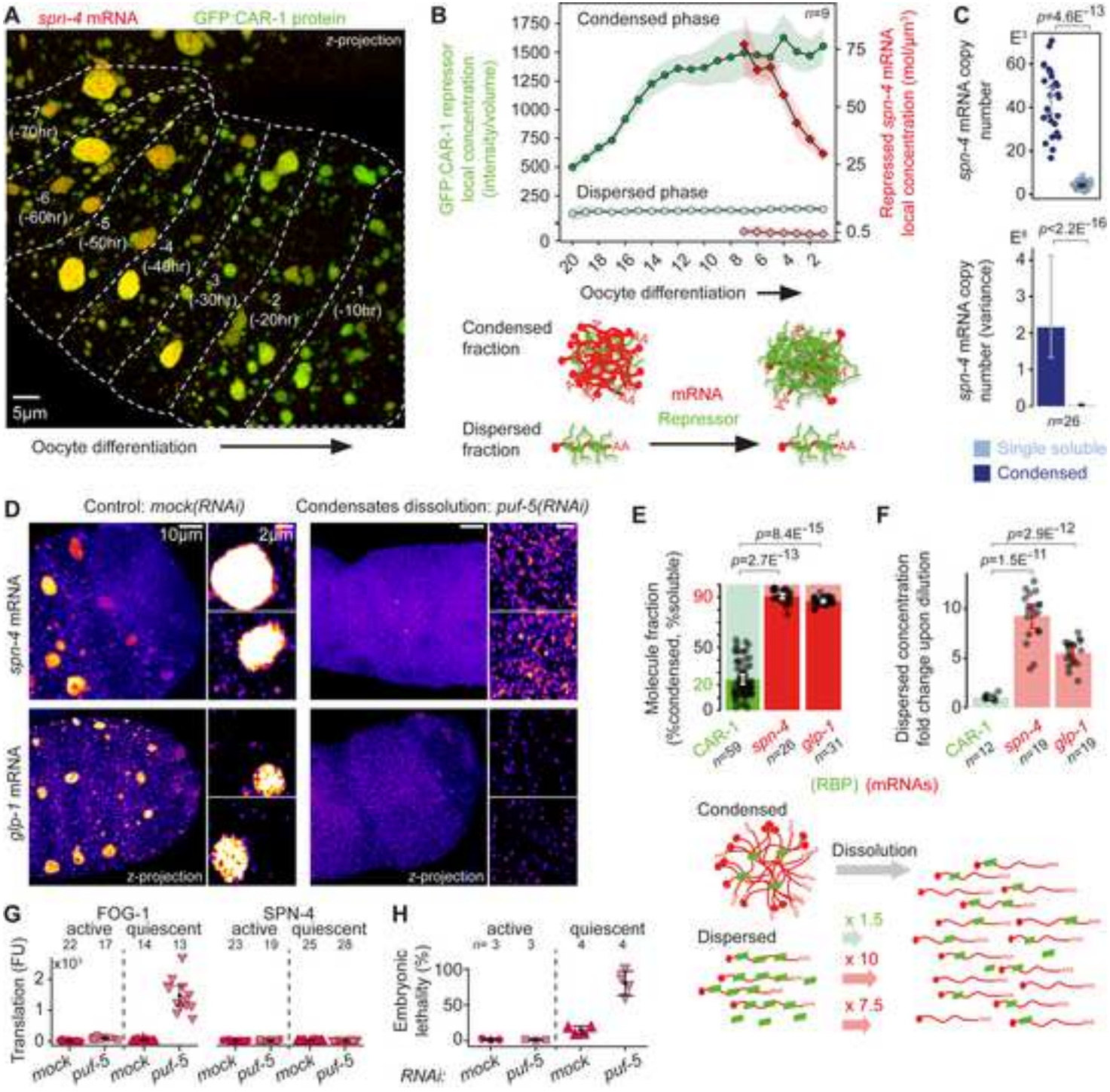

Figure 5

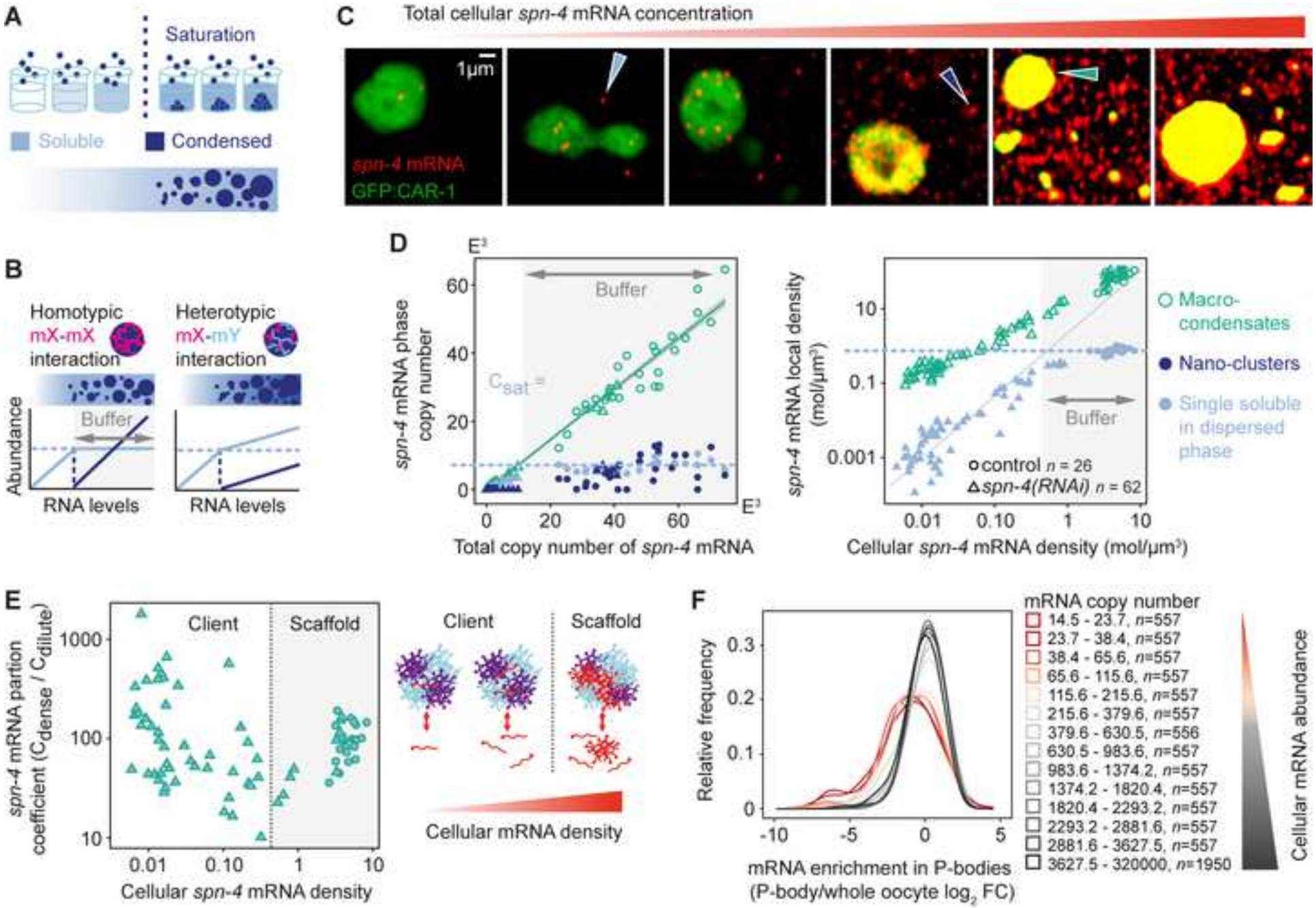

Figure 6

Click here to access/download;Figure;Fig6_600ppi.tif

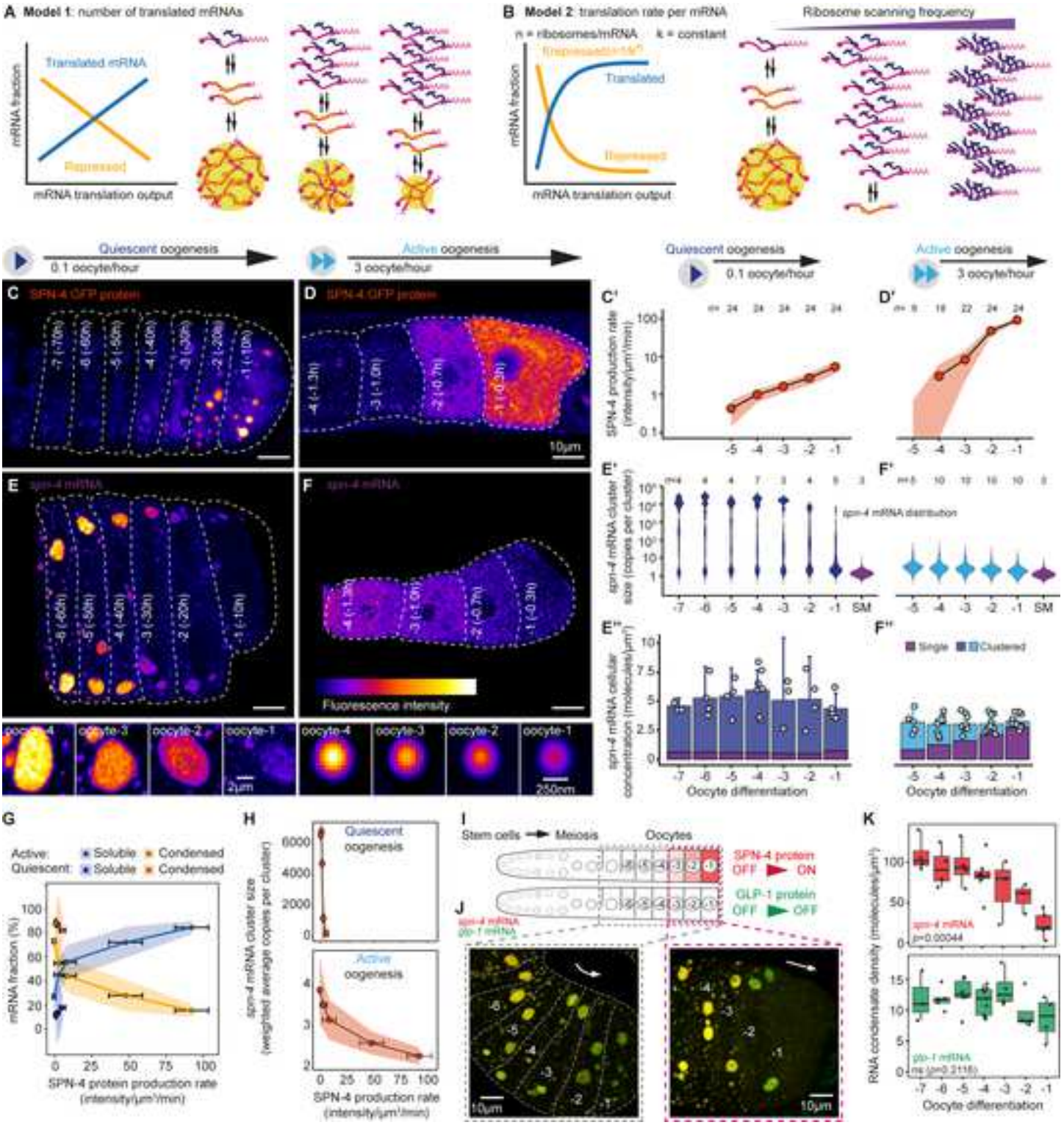

Figure 7

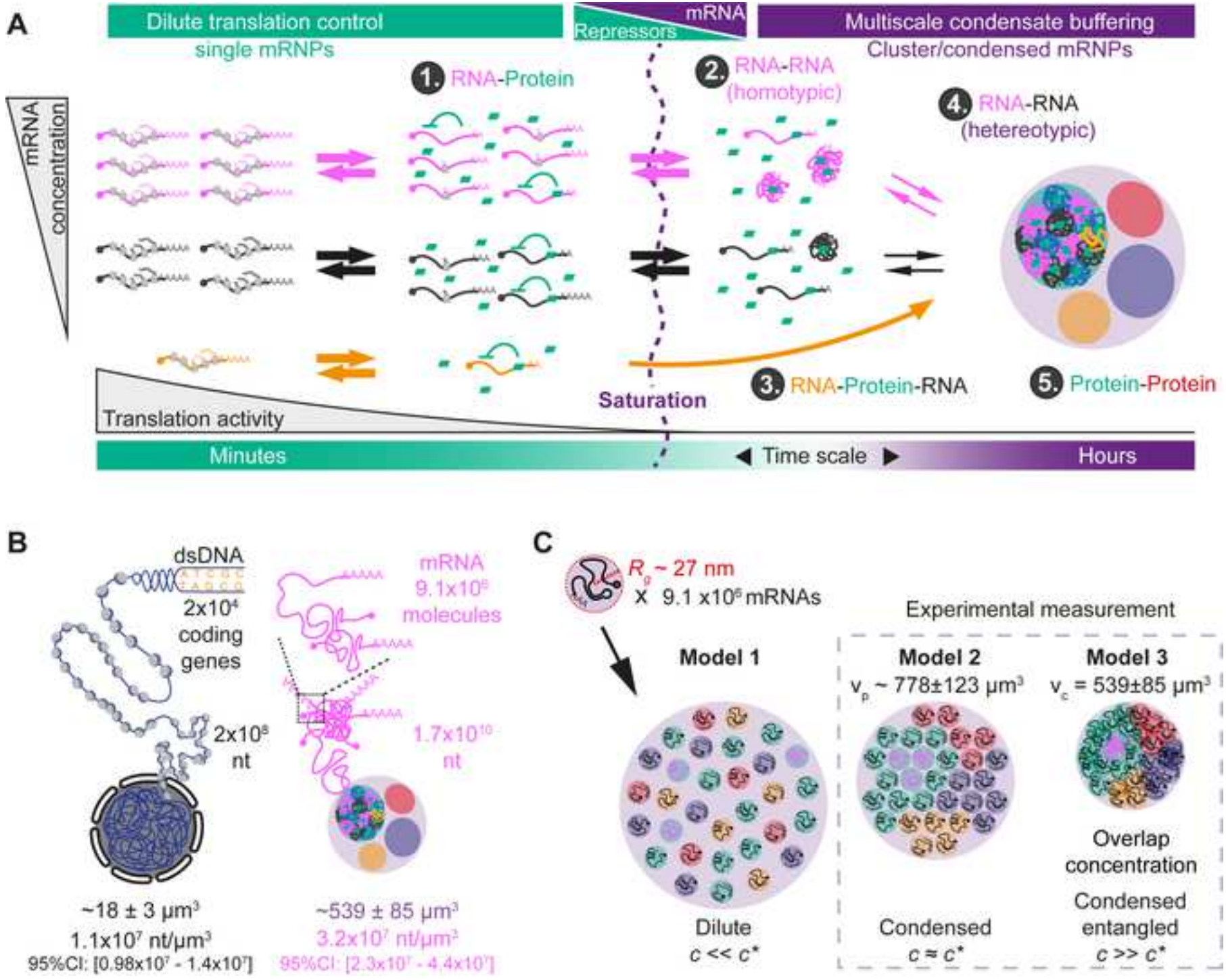

Supplemental Figure S1

Click here to access/download;Supplemental Figure;S1_600ppi.tif

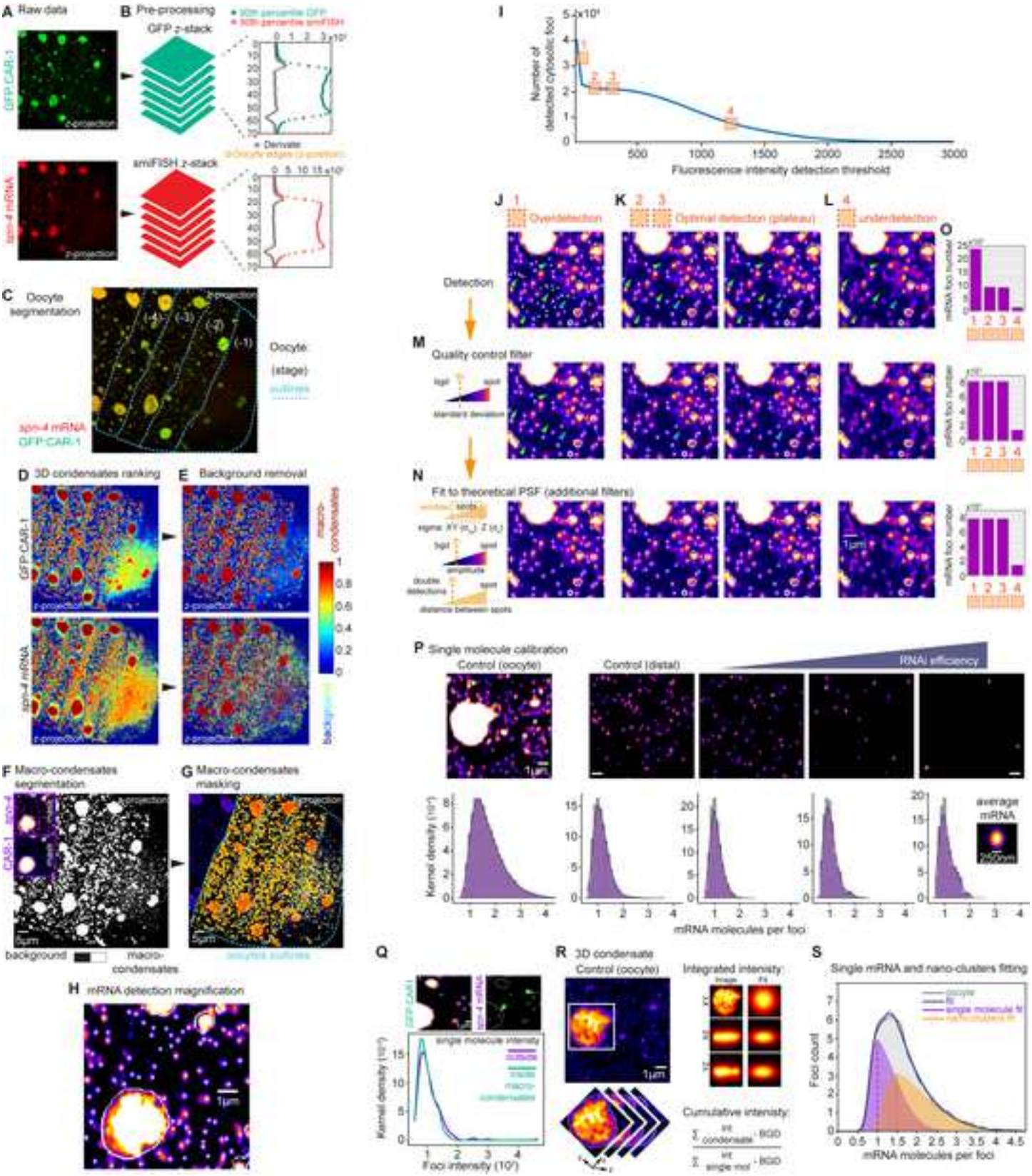

Supplemental Figure S2

Click here to access/download;Supplemental Figure;S2_600ppi.tif

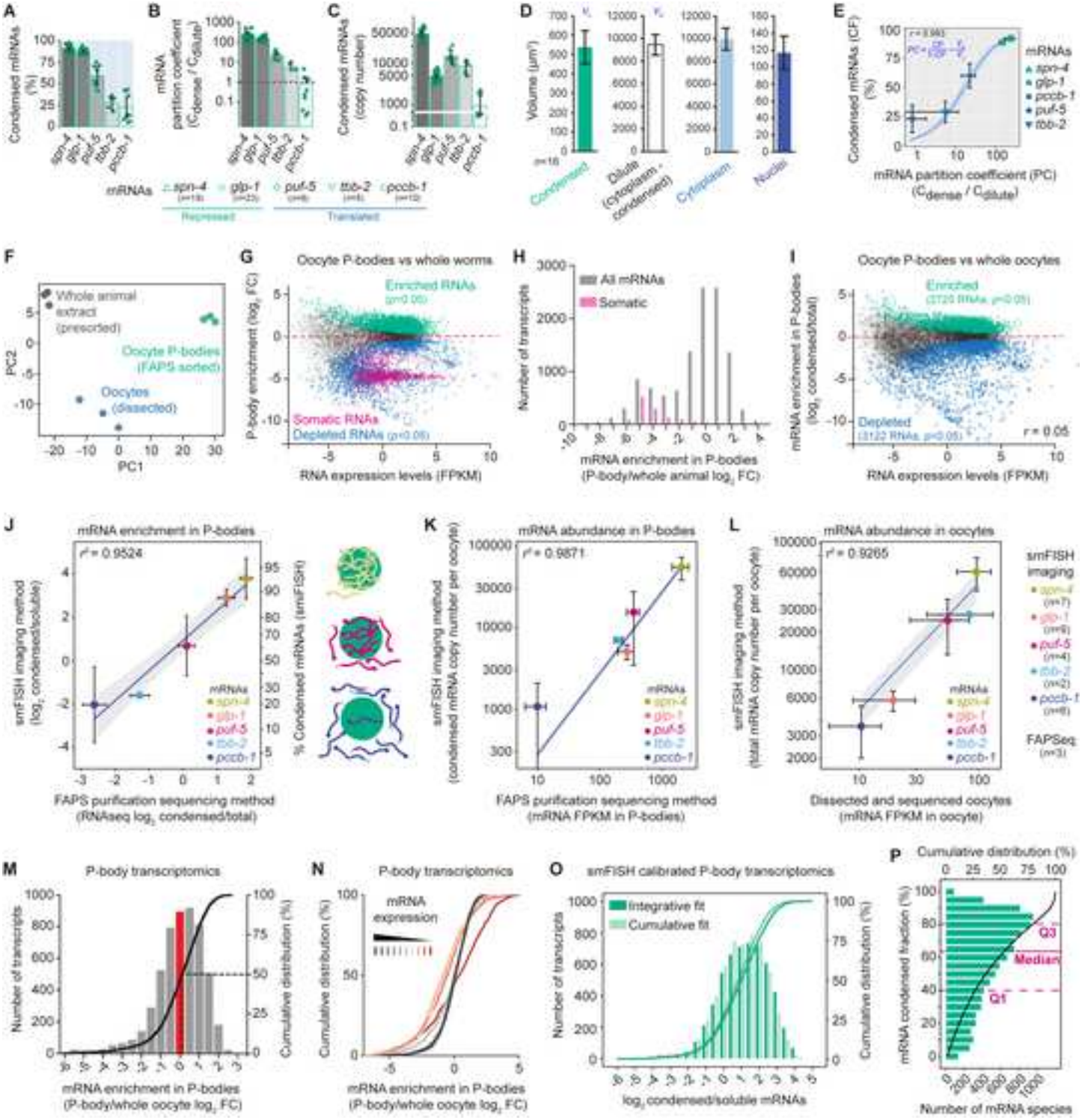

Supplemental Figure S3

Click here to access/download;Supplemental Figure;S3_600ppi.tif

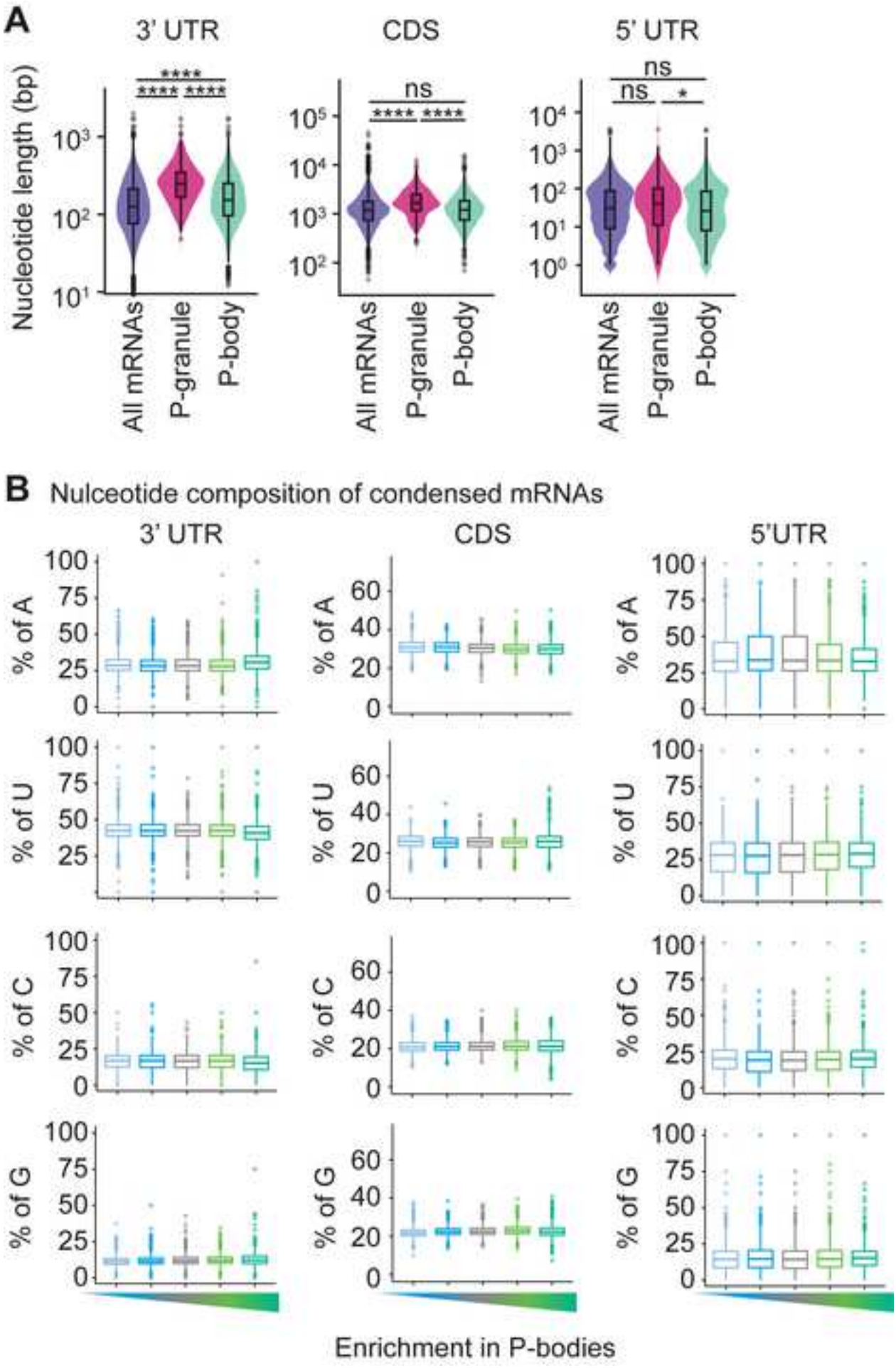

Supplemental Figure S4

Click here to access/download;Supplemental Figure;S4_600ppi.tif

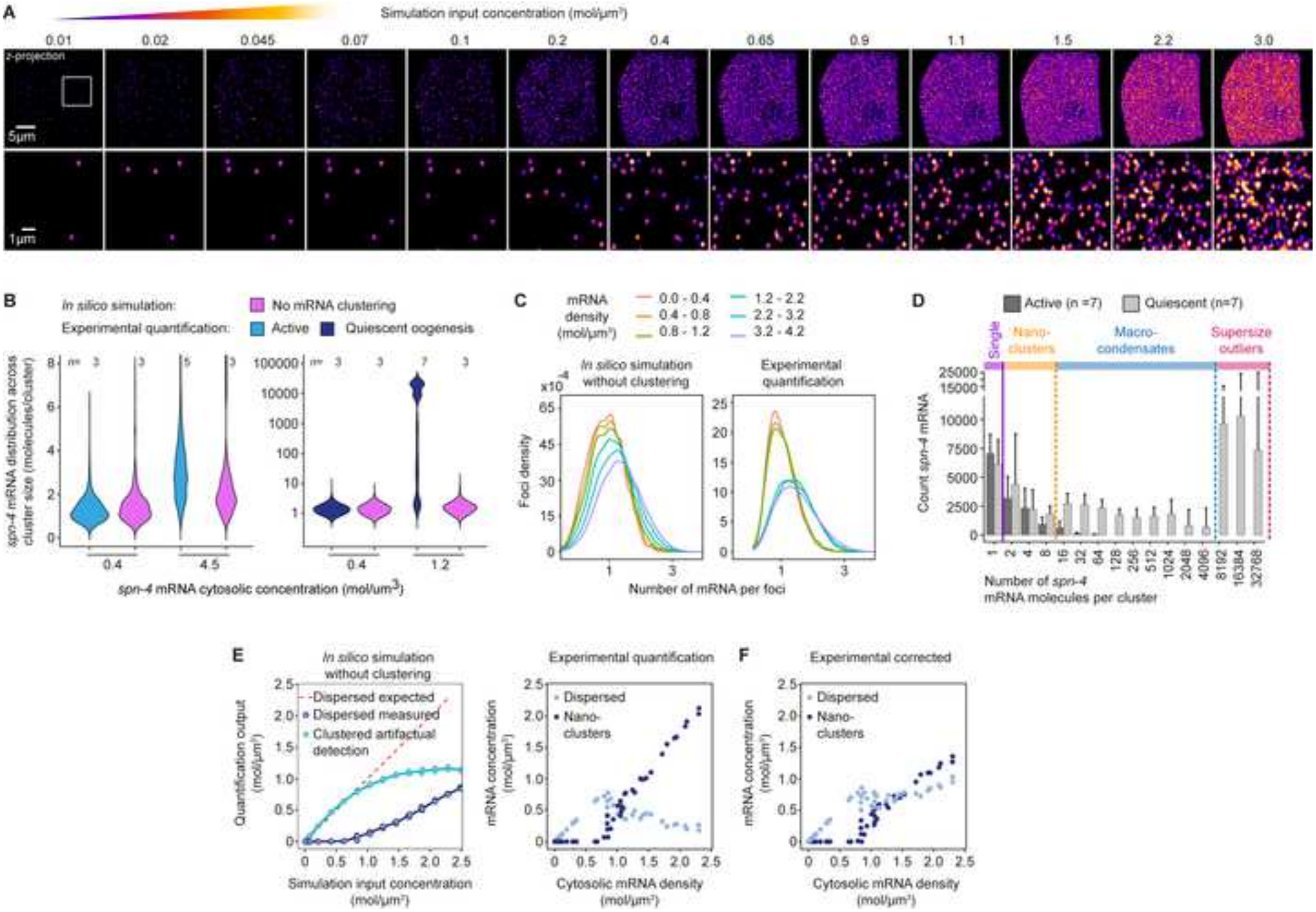

Supplemental Figure S5

Click here to access/download;Supplemental Figure;S5_600ppi.tif

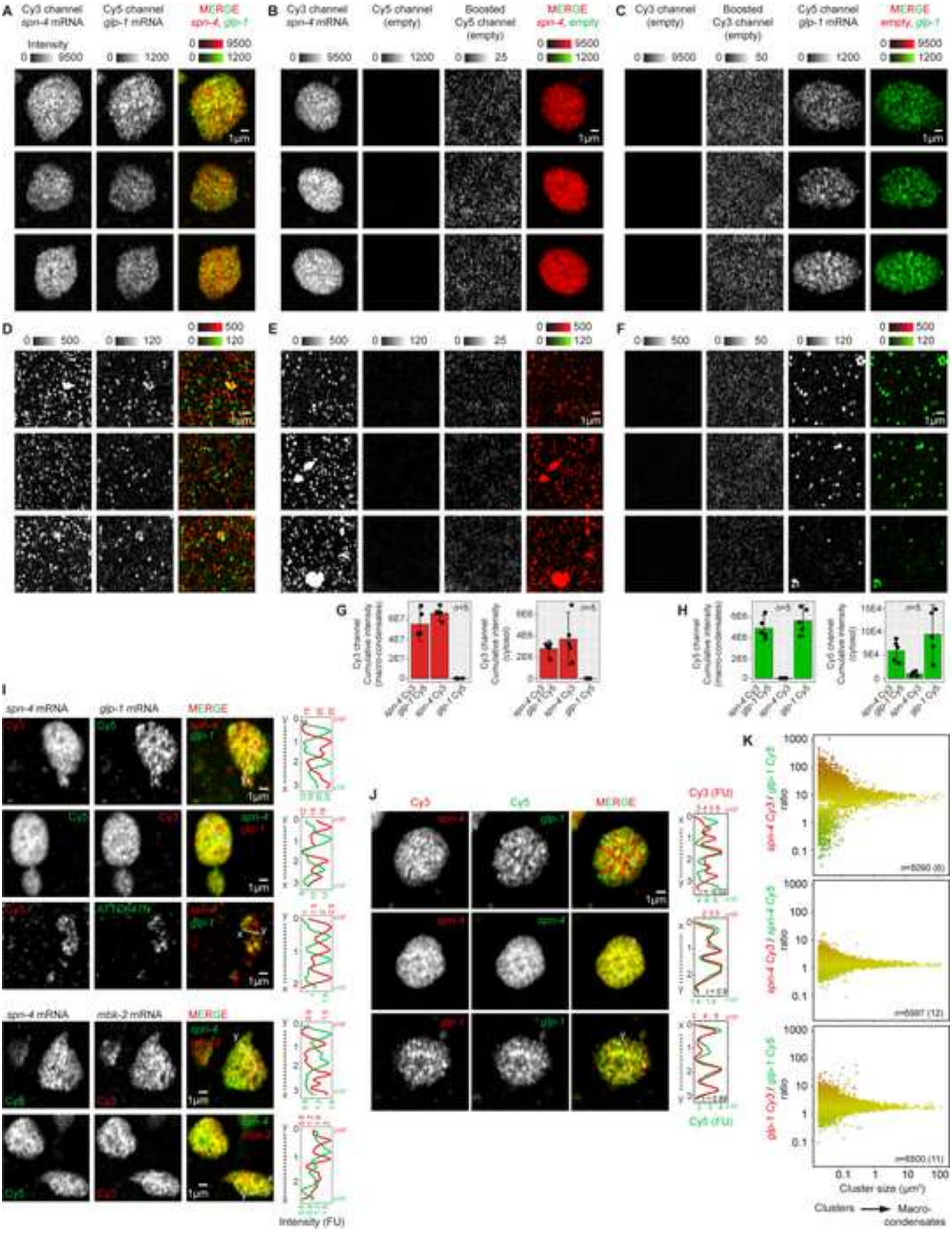

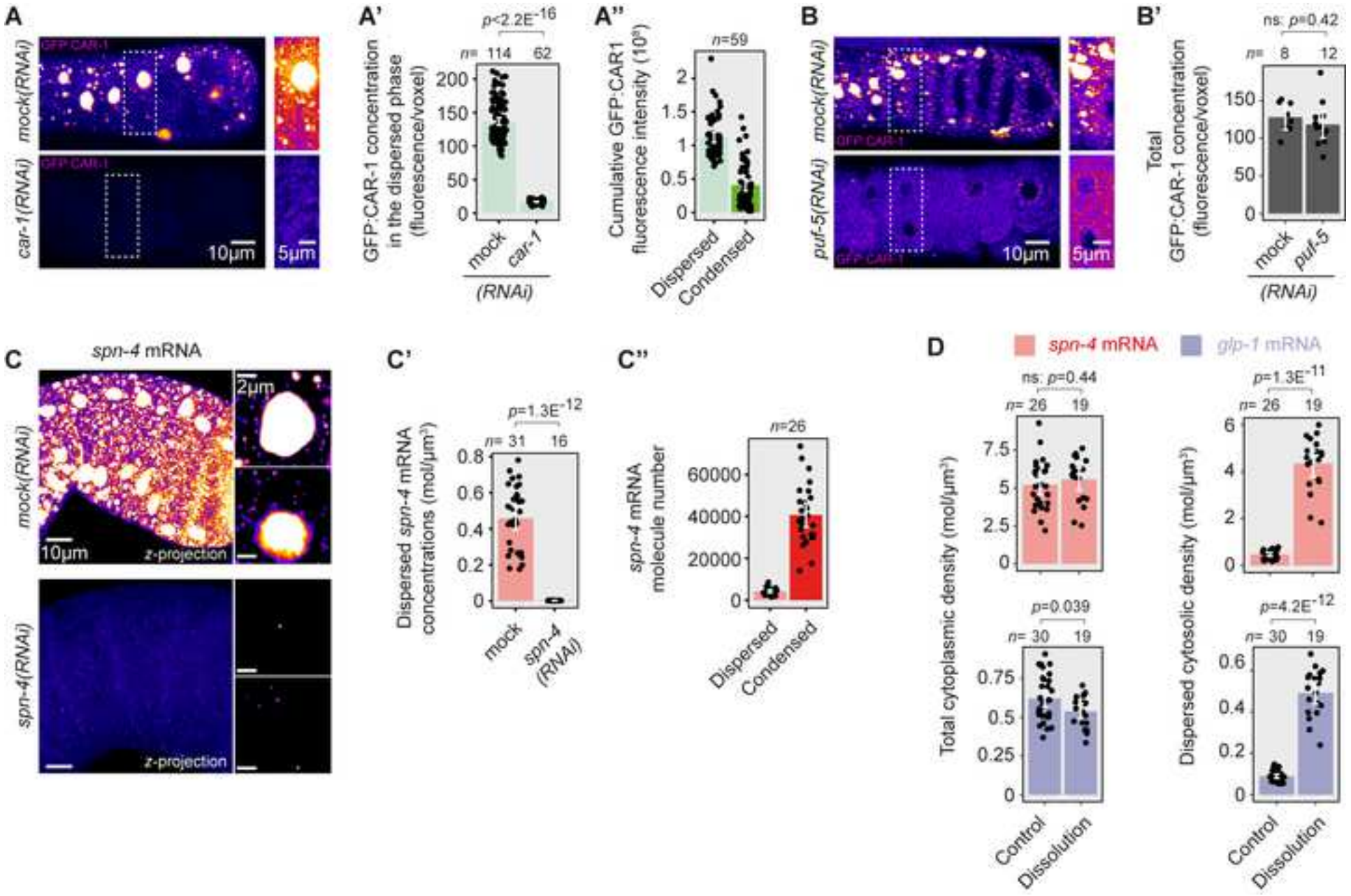

Supplemental Figure S7

Click here to access/download;Supplemental Figure;S7_600ppi.tif

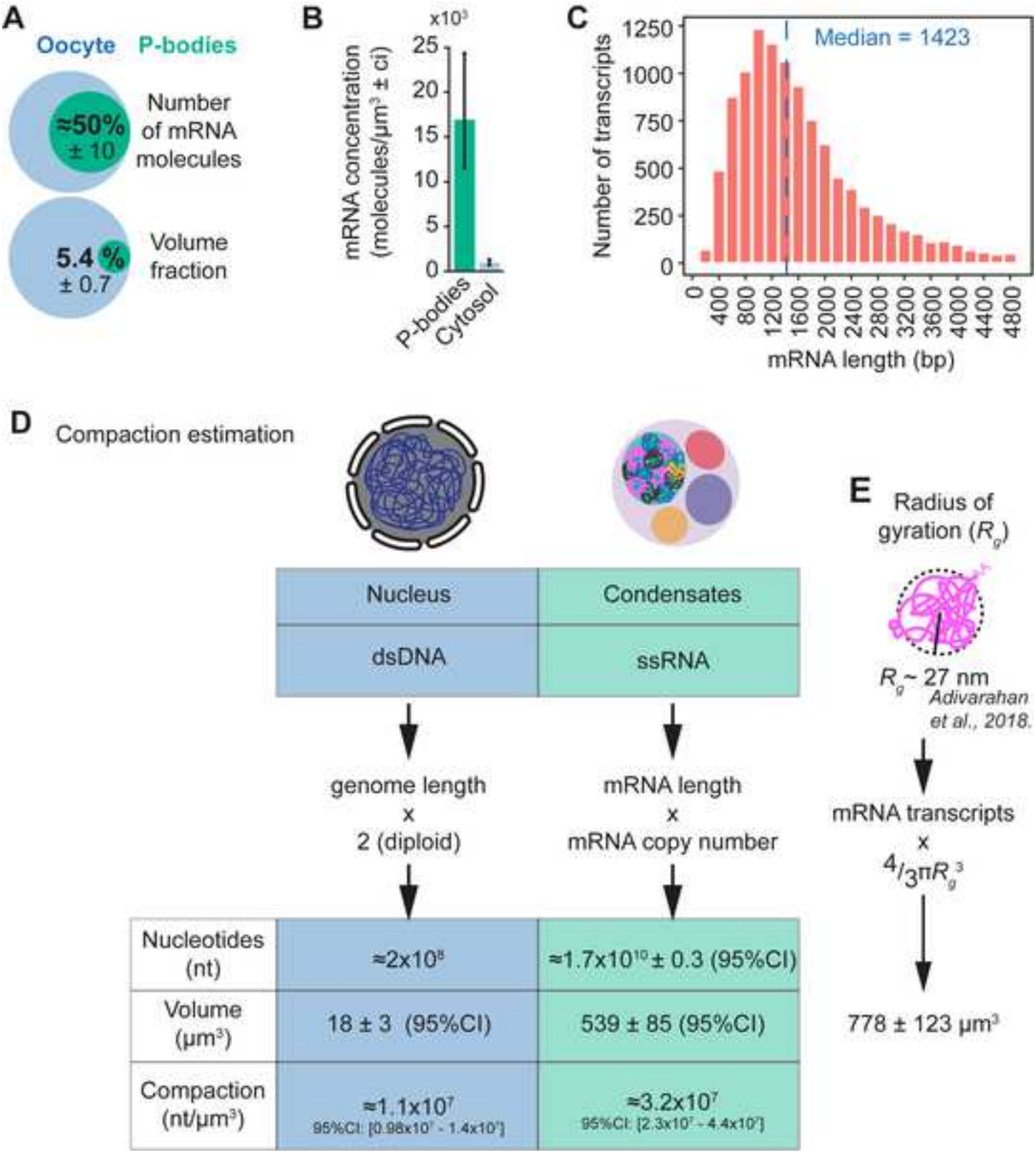

Data S1 - RNA relative enrichment within oocyte P-bodies.

Data S2 - RNA-Seq abundances within oocyte P-bodies

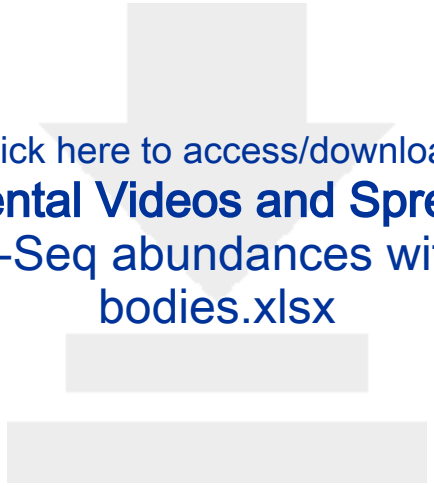

Click here to access/download

Supplemental Videos and Spreadsheets

Data S2 RNA-Seq abundances within oocyte P-bodies.xlsx

Data S3 - Condensed an dissolved mRNA copy numbers in oocytes

Click here to access/download

Supplemental Videos and Spreadsheets

Data S3 Condensed an dissolved mRNA copy numbers in oocytes.xlsx

Data S4 - GO Analysis of P-body enriched and depleted mRNAs